Quantifying Mercury Surface Fluxes by Combining Atmospheric Observations and Models

by

Shaojie Song

B.S., Tsinghua University (2008)
M.S., Tsinghua University (2011)

Submitted to the Department of Earth, Atmospheric and Planetary Sciences
in partial fulfillment of the requirements for the degree of

Doctor of Philosophy in Atmospheric Chemistry

at the

MASSACHUSETTS INSTITUTE OF TECHNOLOGY

September 2016

Author……
Department of Earth, Atmospheric and Planetary Sciences
September 12, 2016

Certified by……
Noelle Eckley Selin
Associate Professor in the Institute of Data, Systems and Society, and Department of Earth, Atmospheric and Planetary Sciences
Thesis Supervisor

Accepted by……
Robert D. van der Hilst
Schlumberger Professor of Earth and Planetary Sciences
Head, Department of Earth, Atmospheric and Planetary Sciences

Quantifying Mercury Surface Fluxes by Combining Atmospheric Observations and Models

by

Shaojie Song

Submitted to the Department of Earth, Atmospheric and Planetary Sciences
on September 12, 2016, in partial fulfillment of
the requirements for the degree of
Doctor of Philosophy in Atmospheric Chemistry

ABSTRACT

Mercury (Hg) is a critical environmental concern. Although an important component of its biogeochemical cycle, large uncertainties still exist in the estimates of surface fluxes of mercury. Three projects presented in this thesis improve our understanding of mercury surface fluxes at different spatial scales by combining atmospheric observations and models. First, a global scale inverse model study uses observations at multiple ground-based stations and simulations from a three-dimensional chemical transport model (GEOS-Chem) to obtain a total mercury emission of about 5.8 Gg yr^{-1}, in which the ocean contributes about a half. The global terrestrial ecosystem is found to be neither a net source nor a net sink of Hg^0 (gaseous elemental mercury). The optimized Asian anthropogenic emissions (0.7-1.8 Gg yr^{-1}) are very likely higher than bottom-up estimates, implying missing sources, higher activity levels, and/or lower control efficiencies in these inventories. Optimizing two physicochemical ocean parameters improves the model's ability in reproducing the seasonal pattern of observed Hg^0. The inversion also suggests that the legacy mercury releases tend to reside in the terrestrial system rather than in the ocean. Second, the comparison of nested grid GEOS-Chem model simulations with aircraft observations support results from the global inversion, and further suggests that the Northwest Atlantic Ocean is a net source of Hg^0, with high evasion fluxes in summer (related to the high precipitation rates and deposition fluxes of oxidized mercury), whereas the terrestrial ecosystem in the eastern United States is likely a net sink of Hg^0 during summer. Third, a one-dimensional chemical transport model is built and used to simulate the mercury diurnal variabilities observed at Dome Concordia on the Antarctic plateau. The model simulation best reproducing the Hg^0 observations shows that in summer mercury is rapidly cycled between the shallow atmospheric boundary layer and the surface snowpack. A two-step bromine initiated scheme oxidizes Hg^0. Oxidized mercury is deposited, photoreduced in the surface snow, and reemitted as Hg^0 back into the atmosphere.

Thesis Supervisor: Noelle Eckley Selin
Title: Associate Professor in the Institute of Data, Systems and Society, and Department of Earth, Atmospheric and Planetary Sciences

Acknowledgments

I must first thank my academic advisor, Professor Noelle Selin, for her supervision and support throughout my graduate career. She has guided me patiently and always gave me timely feedback on my research.

I am grateful to my thesis examination committee members, Professors Susan Solomon, Ronald Prinn, and Daniel Jaffe, for their insightful advice and help that greatly improved the quality of this work.

I would also like to thank the fellow students and researchers in the Selin Group, the Joint Program on the Science and Policy of Global Change, the PAOC, and the MIT Atmospheric Chemistry.

None of this work would have been possible without the collaborators who provided the valuable measurement data and advised me on how to use them — Hélène Angot and Aurélien Dommergue (LGGE), Lynne Gratz and Jesse Ambrose (UW), Franz Slemr (MPI), David Gay and Mark Olson (NADP), Katrine Pfaffhuber (NILU), Kohji Marumoto (NIMD), Shichang Kang and Qianggong Zhang (CAS), and many others. I was also fortunate to work with various members within the GEOS-Chem model community and the international mercury modeling community. Many of them have helped me a lot on the way to become a modeler.

This work was funded by the NSF Atmospheric Chemistry Program (#1053648, #1217010), a MIT-France Seed Fund Program, and the PAOC Houghton Fund.

Final thanks go to my beloved family members who have always been there for me over many years. I dedicate this thesis to my daughter, Maggie.

Contents

List of Figures 9

List of Tables 13

Chapter 1 Introduction 15

1.1 Global Biogeochemical Cycle of Mercury 15
1.2 Current Understanding of Mercury Surface Fluxes 16
1.3 Chapter Descriptions 20

Chapter 2 A Global Scale Inverse Modeling of Atmospheric Mercury and Implications for Its Biogeochemical Cycling 23

2.1 Methodology 23
2.1.1 Ground-based Observations of Atmospheric Hg^0 23
2.1.2 GEOS-Chem Global Mercury Model 29
2.1.3 Emission Inversion: Reference Emission Fluxes 30
2.1.4 Bayesian Inversion Method 35
2.1.5 Parameter Inversion: *A Priori* 37
2.1.6 Error Representation 39
2.2 Emission Inversion: Results 43
2.2.1 Model-Observation Comparison 43
2.2.2 Emission Inversion: Optimized Emission Fluxes 47
2.3 Parameter Inversion: Results 52
2.3.1 *A Posteriori* Parameters 52
2.3.2 Global Ocean Hg Budget 55
2.4 Implications for the Hg Biogeochemical Cycle 57
2.5 Summary and Conclusion 60

Chapter 3 Constraining the Atmosphere–Surface Exchange of Hg^0 over Eastern North America 63

3.1 Methodology 63
3.1.1 Observations 63
3.1.2 GEOS-Chem Global and Nested Grid Simulations 66
3.2 Results 70
3.2.1 Observed Hg^0 in NOMADSS 70

3.2.2 Comparison between Model and Observations 72
3.3 Discussion 77
3.3.1 Enhanced Terrestrial Flux of Hg^0 in Spring 77
3.3.2 Implications for Regional Terrestrial and Oceanic Hg^0 Fluxes 78
3.3.3 Origin of High Hg^0 Flux from the Northwest Atlantic 83
3.4 Conclusions 85
Chapter 4 A Model Calculation of the Diurnal Cycles of Mercury at Dome Concordia on the Antarctic Plateau 87
4.1 Methodology 87
4.1.1 Vertical Transport 88
4.1.2 Atmospheric Mercury Chemistry 91
4.1.3 Mercury in the Free Troposphere 93
4.1.4 Mercury in Surface Snow and its Air–Snow Exchange 96
4.2 Results and Discussion 97
4.2.1 Summer 98
4.2.2 Winter 104
4.2.3 Sensitivity Analysis 106
4.2.4 Comparison with Summit, Greenland 108
4.3 Conclusion 109
Chapter 5 Conclusion 111
Bibliography 115

List of Figures

Figure 1.1. A schematic diagram of the global cycle and the atmosphere-surface exchange of mercury. 16

Figure 1.2. Anthropogenic mercury emissions into the atmosphere from several bottom-up inventories. 17

Figure 1.3. Global net emission fluxes of Hg^0 estimated by the bottom-up approach and assumed in several chemical and transport models..... 18

Figure 2.1. Locations of 27 ground-based observational sites of atmospheric mercury..... 27

Figure 2.2. Hourly (grey) and monthly (red) concentrations of atmospheric mercury measured at ground-based sites. 27

Figure 2.3. Diurnal variations of the average GEM and GOM concentrations measured at two mountain sites, Mauna Loa (MLO) and Mt. Lulin (LUL). 28

Figure 2.4. Decline of Hg^0 concentration calculated from 19 ship cruise measurements in 1990-2009. 29

Figure 2.5. Observed and modeled monthly Hg^0 concentrations over the North Atlantic Ocean..... 29

Figure 2.6. Subsurface water concentrations of inorganic mercury used in our GEOS-Chem modeling..... 33

Figure 2.7. Comparison of the Hg^0 diffusion coefficients (DHg) in seawater..... 33

Figure 2.8. Sensitivities of monthly Hg^0 concentrations at three ground-based observational sites to changes in different sources: (left) the SH ocean emission in March and (right) anthropogenic emission in Asia. 37

Figure 2.9. Responses of Hg^0 concentrations to changes of the partition coefficient (log K_D) (panel a) and dark oxidation rate constant (-log K_{OX2}) (panel b). 39

Figure 2.10. Monthly Hg^0 concentrations for all ground-based observational sites. 45

Figure 2.11. Averaged monthly observations and model simulations of Hg^0 concentrations for the ground-based observational sites in the four regions. 46

Figure 2.12. Scatter plot comparing model outputs (reference simulation, emission inversion, and parameter inversion) to observations of mercury wet deposition fluxes from the NADP/MDN monitoring network during 2009-2011. 47

Figure 2.13. Monthly emissions for the three seasonal sources (NH ocean, SH ocean, and soil) from the reference simulation (blue solid lines), emission inversion (red solid lines), and parameter inversion (green dashed lines). 48

Figure 2.14. Scatter plot of annual Hg^0 dry deposition fluxes modeled by GEOS-Chem (reference simulation) and determined by Zhang et al. (2012a). 50

Figure 2.15. Global ocean mercury budget modeled by GEOS-Chem. 56

Figure 2.16. Average correlations (R^2) between the optimized parameters derived from the special case of parameter inversion 57

Figure 2.17. Simulated ocean and terrestrial reservoirs of mercury using the 7-box model. .. 58

Figure 3.1. Aircraft-, ground-, and ship-based observations used in this study. 65

Figure 3.2. Seasonal variations of terrestrial fluxes of Hg^0 from three model simulations. 69

Figure 3.3. Vertical profile of potential temperature observed during all the NOMADSS research flights. 71

Figure 3.4. Averaged monthly observations and model simulations of Hg^0 concentrations for the NADP AMNet ground-based sites. 73

Figure 3.5. The wet deposition data measured by the NADP MDN and its comparison with different model simulations in 2013 summer. 75

Figure 3.6. Spatial distributions of modeled atmospheric Hg^0 fluxes in eastern North America in summer. 76

Figure 3.7. Different atmosphere-terrestrial mercury exchange processes involved in a forest ecosystem. 81

Figure 3.8. Examples of temporal changes in river water discharge from South Carolina into the Northwest Atlantic during recent years and measurements of precipitation rate and wet deposition flux of mercury in South Carolina during 2013 summer. 82

Figure 3.9. Seasonal variability and spatial distribution of modeled net oceanic Hg^0 flux from the North Atlantic. Results of the model simulation HOXSO are shown. 84

Figure 3.10. Spatial distributions of modeled vertical exchange fluxes in the North Atlantic in summer. 85

Figure 4.1. A schematic diagram of the 1-D chemical and transport model for mercury. 88

Figure 4.2. One-week backward trajectories arriving at Dome C in 2013 summer and winter. 89

Figure 4.3. Vertical structures of the lower atmosphere in summer (a) and winter (b) represented by the average diurnal cycles of the mixing rates between adjacent vertical levels. 90

Figure 4.4. Comparison of Hg^0 concentration at AMS and CPT between observations and models (GEOS-Chem, GMHG, and GLEMOS) in 2013 summer and winter. 95

Figure 4.5. Vertical profiles of the simulated speciated mercury concentrations in the lower atmosphere in 2013 summer and winter. 96

Figure 4.6. Diurnal variations of O_3, OH, and Br in near surface air in summer and winter. . 99

Figure 4.7. Concentrations of NO_2, NO, and HO_2 in near surface air in summer and winter. 99

Figure 4.8. Diurnal cycles of speciated mercury concentrations in summer at Dome C. 101

Figure 4.9. Vertical distributions of the simulated speciated mercury concentrations in the ABL. 102

Figure 4.10. Modeled mercury fluxes in different scenarios. 103

Figure 4.11. Observed and modeled average mercury concentrations in Jan and Feb. 104

Figure 4.12. Diurnal cycles of mercury concentrations in winter at Dome C. 105

Figure 4.13. Profiles of the vertical turbulent diffusion coefficients during winter. 106

Figure 4.14. Diurnal cycles of simulated mercury concentrations in summer using different Hg^{II} deposition velocities V_d (m s^{-1}). 107

Figure 4.15. Diurnal profiles of simulated mercury concentrations in summer using different lifetime of mercury photoreduction in surface snowpack. 108

List of Tables

Table 2.1. Information for ground-based observational sites of atmospheric mercury. 26

Table 2.2. Summary of over-water Hg^0 observational data in the North Atlantic Ocean..... 28

Table 2.3. Global mercury emissions into the atmosphere. 31

Table 2.4. Uncertainty information for each ground-based observational site. 42

Table 2.5. Comparison of Asian Hg^0 emissions from recent studies. 52

Table 2.6. Evolution of the estimates of the four parameters in the parameter inversion. 53

Table 2.7. Recent surface ocean mercury measurements and corresponding simulated concentrations. 54

Table 2.8. Present-day reservoirs and fluxes used to calculate first-order rate coefficients in the 7-box model of Hg global cycle. 59

Table 3.1. Global budgets of mercury from three GEOS-Chem model simulations. 68

Table 3.2. Observed and modeled Hg^0 concentrations during NOMADSS. 72

Table 3.3. Observed and modeled air and aqueous Hg for three summertime Northwest Atlantic ship cruises. 75

Table 3.4. A summary of measured net emission fluxes of Hg^0 for different land uses and seasons. 78

Table 4.1. Gas phase mercury reactions used in our model. 94

Table 4.2. Model scenarios with varying physical and chemical parameters in summer. 101

Chapter 1 Introduction

1.1 Global Biogeochemical Cycle of Mercury

Mercury (Hg) is a ubiquitous trace metal that cycles among the atmosphere, ocean, land, and biosphere (Selin, 2009). It is regarded as a critical environmental concern mainly due to the adverse effects of methylmercury on human health (Mergler et al., 2007). Methylmercury is a potent neurotoxin produced in aqueous environments from inorganic mercury by anaerobic bacteria and bioaccumulates in the food web. It is essential to understand the global mercury biogeochemical cycle (see Figure 1.1) in order to evaluate its effects on human society and to design effective regulation strategies (Giang and Selin, 2016).

Unlike most other metals, mercury in the lower atmosphere exists primarily in its elemental form Hg^0 (gaseous elemental mercury, GEM), which is semi-volatile and poorly soluble (Lin and Pehkonen, 1999). The major loss pathway of Hg^0 in the atmosphere is via oxidation to Hg^{II} (oxidized mercury), a much more soluble form which partitions between gas and particle phases and is subject to rapid dry and wet deposition processes (Lindberg et al., 2007). Hg^{II} may also be photoreduced to Hg^0 in cloud droplets, but either the oxidation or reduction mechanisms of atmospheric mercury are still not well understood (Ariya et al., 2015). It has been shown that mercury has a relatively long residence time (about 6 months to 2 years) in the atmosphere and thus can be transported in long distances (Selin et al., 2007).

After being deposited on terrestrial and water surfaces, part of the Hg^{II} can be converted to methylmercury (in aqueous environments), and part of the Hg^{II} can be reduced photochemically and/or biochemically to Hg^0 and then readily reemitted back to the atmosphere (Selin et al., 2008). Thus Hg^0 exchange at the Earth's surfaces is bi-directional which means both emission and deposition may occur (Figure 1.1). The remobilization of deposited mercury also suggests that the atmosphere continues to be affected by historical releases. Human activities have strongly changed the cycling of mercury at local, regional, and global scales (Amos et al., 2013; Driscoll et al., 2013). Mercury emissions from surfaces can be natural (e.g., volcano eruptions and geogenic activities), anthropogenic, and/or due to the legacy of historical releases (also known as reemissions). Although they are important components of the biogeochemical cycle

of mercury, as described below, both anthropogenic emission fluxes and exchange fluxes of Hg^0 at terrestrial and ocean surfaces are poorly constrained. The research projects presented in this thesis go beyond previous studies and quantify the surface fluxes of mercury at different spatial scales by combining atmospheric observations and models.

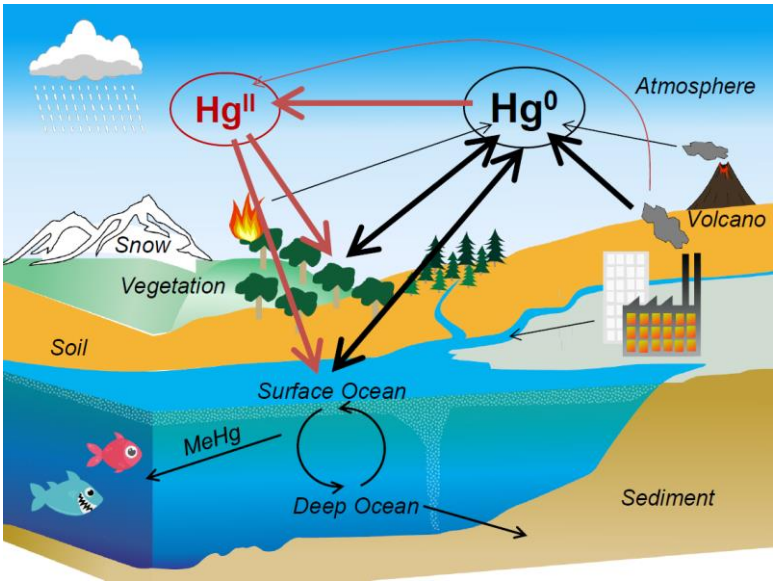

Figure 1.1. A schematic diagram of the global cycle and the atmosphere-surface exchange of mercury. MeHg is the short name of methylmercury.

1.2 Current Understanding of Mercury Surface Fluxes

Current estimates of mercury surface fluxes to the atmosphere are mainly built on a bottom-up approach. Anthropogenic mercury emission inventories determined by such an approach are commonly based on emission factors, activity levels, and abatement efficiency (Pacyna et al., 2010). For example, in order to estimate mercury emissions from the sector of coal-fired power plants, the information including the amount of coal burned during a given time period (activity levels), the mercury content in coal (emission factors), and the efficiency of the in-combustion and end-of-the-pipe control devices should be gathered. On a global scale, artisanal and small scale gold mining, coal burning, metal smelting, and cement production are the most important

mercury emitting sectors (AMAP/UNEP, 2013). As shown in Figure 1.2, different bottom-up anthropogenic mercury emission inventories consistently suggest that in recent years Asia is the largest emitter contributing about a half to the global total, whereas the contributions from the developed regions such as European Union and North America are relatively small. Figure 1.2 also indicates that large uncertainties exist in these bottom-up inventories. For example, anthropogenic mercury emission from Asia ranges from ~ 0.5 to > 2.0 Gg yr^{-1} (a factor of 4) by AMAP/UNEP (2013).

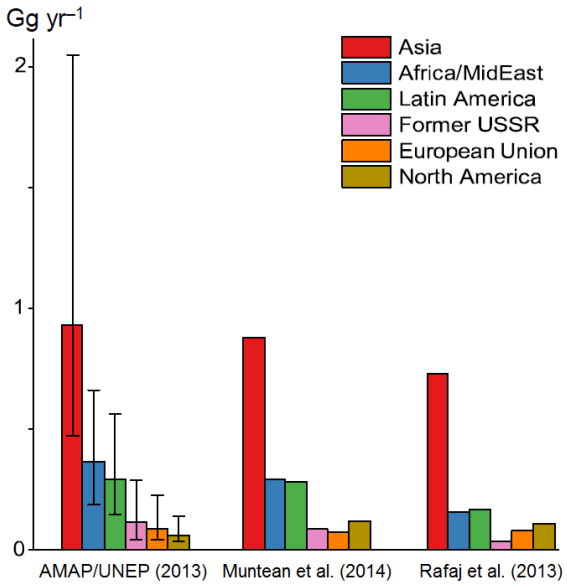

Figure 1.2. Anthropogenic mercury emissions into the atmosphere from several bottom-up inventories. AMAP/UNEP (2013) and Rafaj et al. (2013) are based on activity data in the year of 2010, whereas Muntean et al. (2014) is based on data in the year of 2008.

As described earlier, the exchange of Hg^0 at terrestrial and ocean surfaces is bi-directional: both evasion (upward) and dry deposition (downward) may occur at the interface. A positive (negative) net flux indicates that Hg^0 evasion exceeds (is lower than) its dry deposition (Gustin et al., 2008; Xu et al., 1999). The bottom-up approach estimates global and regional exchange fluxes of Hg^0 at ocean and terrestrial surfaces by extrapolating limited measurements and/or use simplified process models (Mason, 2009; Kuss et al., 2011).

More than 100 field flux measurement studies have been conducted since 1970s to measure Hg^0 exchange fluxes at various terrestrial surface types (e.g., soil, forest, grassland, and snow) and to determine environmental factors influencing these fluxes (Agnan et al., 2016). Dynamic flux chambers (DFCs) and micrometeorological techniques (MMs) are the two mostly widely approaches accounting for > 90% of all observations, however, systematic biases may exist in their measured fluxes (Zhu et al., 2016). In addition, these measurements have been unevenly distributed in time and among regions and landscapes. Through extrapolating these local-scale (<0.1 to 10^3 m^2) flux measurements to a global scale, it remains unclear whether the global terrestrial ecosystem acts as a net source or a net sink of atmospheric Hg^0. As shown in Figure 1.3, an earlier study (Pirrone et al., 2010; Mason, 2009) showed that the global Hg^0 net emission flux at terrestrial surfaces was positive (1.8 Gg yr^{-1} with a uncertainty range of 1.0–3.4 Gg yr^{-1}). A more recent study by Agnan et al. (2016) estimated a global net Hg^0 flux of 0.4 Gg yr^{-1} with a large uncertainty range of -2.9 to 4.5 Gg yr^{-1} (50% confidence interval). Agnan et al. (2016) has also suggested that the largest uncertainty in estimating global terrestrial Hg^0 fluxes arises from the forest ecosystem, which has a median flux of -59 Mg yr^{-1} (a small net sink) and a very large 50% confidence interval (-2.6 to 3.3 Gg yr^{-1}).

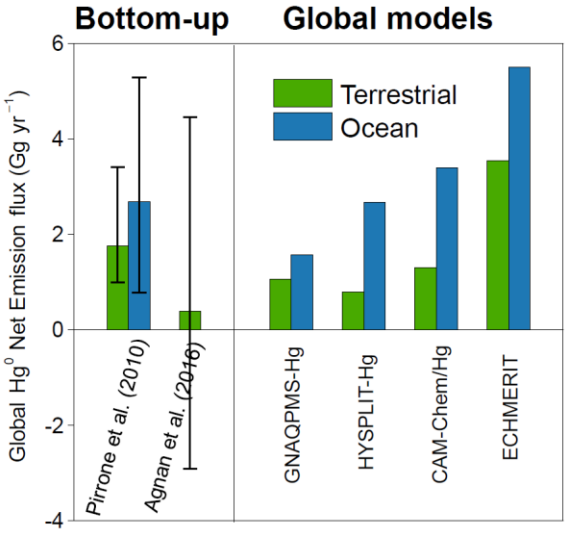

Figure 1.3. Global net emission fluxes of Hg^0 estimated by the bottom-up approach and assumed in several chemical and transport models. The references for the global models are GNAQPMS-Hg (Chen et al., 2015), HYSPLIT-Hg (Cohen et al., 2016), CAM-Chem/Hg (Lei et al., 2013), and ECHMERIT (Jung et al., 2009; De Simone et al., 2014).

Most atmospheric mercury chemical and transport models treat Hg^0 emission from, and dry deposition to, the terrestrial ecosystem separately. Dry deposition flux is typically simulated using a resistance-in-series scheme (Wesely, 1989). Due to lack of a clear understanding of all the controlling factors, some models calculate soil emission fluxes using empirical equations involving several important factors such as solar radiation, temperature, and the substrate Hg concentrations (Selin et al., 2008; Holmes et al., 2010; Lei et al., 2013; Lin et al., 2010; Shetty et al., 2008). Terrestrial emissions in some other models are mapped according to biogenic CO emission and/or historical Hg deposition and are scaled by global Hg budgets (Chen et al., 2015; Dastoor et al., 2015; Jung et al., 2009). As shown in Figure 1.3, most models assume that the global terrestrial ecosystem is a net source of Hg^0 and the net emission flux ranges from 0.8 to 3.6 Gg yr^{-1} (Chen et al., 2015; Lei et al., 2013; De Simone et al., 2014; Cohen et al., 2016).

The global ocean is believed to be a net Hg^0 source, but its magnitude is uncertain (Figure 1.3). Air–ocean Hg^0 exchange can be estimated using flux chamber techniques or by measuring the gradient between air Hg^0 and oceanic Hg^0 (also known as dissolved gaseous mercury, DGM) levels (Gårdfeldt et al., 2003). Most ocean surfaces have been observed to be supersaturated in DGM partly due to the very low solubility of Hg^0 in water, generating a positive net flux of Hg^0 to the atmosphere (Soerensen et al., 2014; Kuss et al., 2011; Ci et al., 2011). Global Hg^0 fluxes from oceanic surfaces have been estimated in the range of 1.5–5.5 Gg yr^{-1} by different numerical models (Strode et al., 2007; Soerensen et al., 2010a; De Simone et al., 2014; Lei et al., 2013; Chen et al., 2015; Sunderland and Mason, 2007) and using flux scaling methods (Mason and Sheu, 2002).

The estimates of regional scale mercury fluxes are also very uncertain. For example, the net Hg^0 terrestrial fluxes from the contiguous United States may also be positive or negative based on flux scaling methods (-183 to 269 Mg yr^{-1} (50% confidence interval; Agnan et al., 2016)) and a newly developed model of estimating the air-surface bi-directional exchange of mercury (118–141 Mg yr^{-1} (Wang et al., 2014)). The Antarctic plateau is the most remote and least explored region of mercury dynamics. Although it is far from most anthropogenic emission sources, this region receives significant inputs of mercury because it is subject to long-range atmospheric transport and is readily cycled at surfaces (Dommergue et al., 2010; Selin, 2009). The Antarctic plateau is a vast (~ 7 million km^2) area of snow-covered ice and is elevated

(~ 3000 m above sea level) and mostly flat. Thus it is an ideal region to study the atmosphere-snow mercury exchange which is currently virtually unknown (Dommergue et al., 2012).

Overall, we describe in this section that both anthropogenic emission fluxes and exchange fluxes of Hg^0 at terrestrial and ocean surfaces are still poorly constrained.

1.3 Chapter Descriptions

The goal of this work is to better quantify the surface fluxes of mercury at different spatial scales. To accomplish this goal, we combine atmospheric observations and models. Three projects are contained in the Chapters 2–4 of this thesis. Chapters 2 and 3 have been published as journal papers (Song et al., 2015; 2016) and Chapter 4 is currently in preparation for journal publication. Chapter 5 summarizes the conclusions of this thesis.

The inverse approach is a powerful tool to quantitatively combine observations and models, and has been widely used to derive sources and sinks of greenhouse gases and ozone-depleting substances (Gurney et al., 2002; Xiao et al., 2010). Inverse studies have only addressed mercury at regional scales (de Foy et al., 2012; Roustan and Bocquet, 2006). In **Chapter 2**, we present the first ever global-scale inverse modeling study combining a global three-dimensional model and atmospheric Hg^0 concentrations observed at multiple ground-based sites in order to better constrain Hg^0 emission fluxes from terrestrial and oceanic surfaces. The reference (*a priori*) emission fluxes agree well with bottom-up estimates. A Bayesian inversion method is used to obtain the optimized (*a posteriori*) emissions taking into account uncertainties in both reference emissions and ground-based observations. Key uncertain model parameters are identified and then optimized. The implications of our inversion results for the global biogeochemical mercury cycle are also discussed. In this study, we also find that the uncertain atmospheric mercury chemical mechanisms and the potential large systematic uncertainty of the Hg^0 measurements at different ground-based sites may limit the assessment of terrestrial and oceanic fluxes (Ebinghaus et al., 1999; Slemr et al., 2015).

Such uncertainty is minimized, however, when a consistent instrument is used to measure Hg^0 in different locations. Thus in **Chapter 3**, we use aircraft measurements and compare them with the Hg^0 data from mercury chemical transport modeling in terms of their constraints on

the large scale terrestrial and oceanic fluxes of Hg^0 from eastern North America. Multiple model simulations are performed and our model–observation comparisons suggest that the Northwest Atlantic may be a net source of Hg^0, with high evasion fluxes in summer, while the terrestrial ecosystem in the eastern United States is likely a net sink of Hg^0 during summer. The relationships between the inferred high Hg^0 fluxes from the Northwest Atlantic and high precipitation rates in this region are also investigated.

The Antarctic plateau is an ideal region to study the atmosphere-snow exchange of mercury (Dommergue et al., 2012). Brooks et al. (2008) has suggested that a photochemically driven mercury cycle should occur at the air–snow interface. More recently, Angot et al. (2016) reported the first year-round record of Hg^0 at the French-Italian Concordia Research Station, Dome C (75°06' S, 123°21' E). Hg^0 in near surface air at Dome C showed a distinct diurnal cycle during summer, with a maximum around noon and a minimum around midnight. **Chapter 4** builds a one-dimensional chemical and transport model and uses it to quantitatively explore and identify the most important processes contributing to the Hg variability. Model simulations reveal that the fast oxidation of Hg^0 by a two-step bromine-initiated scheme and the reemission of deposited mercury from the surface snow are necessary to reproduce the observed distinct diurnal cycles of Hg^0 concentration in summer.

Chapter 2 A Global Scale Inverse Modeling of Atmospheric Mercury and Implications for Its Biogeochemical Cycling

In this chapter, we apply a top-down approach on a global scale to quantitatively estimate present-day mercury emission fluxes (emission inversion) as well as key parameters in the GEOS-Chem chemical transport model (parameter inversion). We combine atmospheric Hg^0 ground-based observations and global model simulations. Reference (*a priori*) emissions are from GEOS-Chem parameterizations and agree well with bottom-up estimates. We adopt a Bayesian inversion method to obtain the optimized (*a posteriori*) emissions, with a monthly time step, taking into account uncertainties associated with both reference emissions and ground-based observations. The optimized emissions from ocean and terrestrial surfaces and from anthropogenic sources are shown. We use the results of the emission inversion to identify key uncertain model parameters, and optimize them in the parameter inversion. Finally, we discuss the implications of our inversion for the global biogeochemical mercury cycle.

2.1 Methodology

2.1.1 Ground-based Observations of Atmospheric Hg^0

In this inverse modeling study, we only use GEM and TGM observations to constrain Hg surface fluxes because we are not able to quantify the uncertainty existing in the present GOM and PBM measurements (Jaffe et al., 2014; McClure et al., 2014). We identify high-frequency observations of GEM and TGM concentration for our inversions using two criteria. First, we choose sites in rural and remote areas that are not strongly affected by local emission. Second, we require that observations at different sites are minimally correlated (Brunner et al., 2012). Our mercury data sets at rural/remote sites are drawn from the NADP Atmospheric Mercury Network (AMNet) (Gay et al., 2013), the Canadian Measurement Networks (including the Canadian Air and Precipitation Monitoring Network (CAPMoN) and other sites sponsored by Environment Canada) (Cole et al., 2014), and the European Monitoring and Evaluation

Programme (EMEP) (Tørseth et al., 2012). We use data from 2009-2011, when all these networks were active. In order to expand the spatial coverage of Hg observations, we also collect data from individual sites for recent years (2007-2013). Some sites are included in the Global Mercury Observation System (GMOS) (Pirrone et al., 2013). All sites use Tekran analyzers, operated in sampling intervals of 5-30 min. We calculate the Pearson's correlation coefficients between each two pair of sites using hourly data, and exclude several sites due to their strong correlations with each other. Thus atmospheric mercury data at the sites used in our inversion are all uncorrelated or only weakly correlated ($-0.3 < r < 0.4$, $n = 10^3$–10^4).

Table 2.1 shows the names, locations, and affiliated networks of the 27 ground-based sites used in our inversion. Site locations are also plotted in Figure 2.1. For most of these sites GEM data are used, and for a few sites where GEM data are not available we use TGM data. The difference between measured GEM and TGM concentrations in remote near-surface air is usually < 1% (Lan et al., 2012; Weigelt et al., 2013; Steffen et al., 2014), and thus we do not distinguish between measured GEM and TGM concentrations and use Hg^0 to represent them throughout the chapter. Original observational data are converted into hourly averages and then into monthly averages (Figure 2.2). We require more than 30 min of data to derive an hourly average and more than 10 day of data to derive a monthly average. Where full data are available, median values are used to suppress the influence of high Hg^0 due to local or regional pollution events (Jaffe et al., 2005; Weigelt et al., 2013) or occasional low Hg^0 due to non-polar depletion events (Brunke et al., 2010). For a few individual sites (Table 2.1), the original data are not available, and monthly arithmetic means are used. Finally, multiple-year averages are calculated. Atmospheric Hg^0 concentrations are given in ng m^{-3} at standard temperature and pressure.

Four polar sites are included (ALT, ZEP, and ADY in Arctic and TRS in Antarctica) in our inversion. Episodically low Hg^0 is observed at these sites in polar spring (Cole et al., 2013; Pfaffhuber et al., 2012). These so-called Atmospheric Mercury Depletion Events (AMDEs) result from rapid Hg^0 oxidation and deposition driven by halogens (Steffen et al., 2008). Volatilization of the deposited Hg and the large quantities of imported mercury from circumpolar rivers to the Arctic Ocean are hypothesized to contribute to the observed summer Hg^0 peak in the Arctic region (Dastoor and Durnford, 2013; Fisher et al., 2012). The lack of

understanding of above physical and chemical processes limits the capability of the GEOS-Chem model to reproduce the observed reactivity of Hg^0 in the polar spring and summer. For these reasons we remove Hg^0 data at polar sites for this period (i.e. Mar.-Sep. in Arctic and Oct.-Mar. in Antarctica). In Chapter 4, we present a detailed analysis of mercury variabilities over the Antarctic plateau.

We also include three mountain-top sites (LUL, MBO, and MLO). These sites are affected by upslope surface air during the day and downslope air from the free troposphere at night (Fu et al., 2010; Sheu et al., 2010). The downslope air usually contains higher levels of GOM than the upslope air does due to oxidation of Hg^0 to GOM in the free troposphere (Timonen et al., 2013). Therefore, Hg^0 at mountain-top sites may peak in the afternoon whereas GOM may peak between midnight and early morning (see Figure 2.3 for two mountain-top sites, i.e., Mauna Loa (MLO) and Mt. Lulin (LUL)), generally showing an opposite diurnal pattern to most low-elevation sites (Lan et al., 2012). The minimum hourly Hg^0 at night is calculated to be ~ 90% of the all-day average. Thus, to represent Hg^0 modeled by GEOS-Chem at a vertical layer in the free troposphere (this layer is obtained by matching observed air pressure), the observed mountain-top Hg^0 data are multiplied by 0.9.

We do not include over-water atmospheric Hg^0 observations (i.e. from ship cruises) in the inversion because they are very limited and usually cover large areas, making their observational errors difficult to estimate. Instead, we use over-water observations as an independent check of our inversion results constrained by ground-based observations only. The North Atlantic Ocean is the most densely sampled ocean basin. Soerensen et al. (2012) assembled Hg^0 measurements from 18 ship cruises in this region during 1990-2009 and found a statistically significant decrease of -0.046 ± 0.010 ng m^{-3} yr^{-1}. However, previous GEOS-Chem simulations of Hg^0 concentration did not take this multi-decadal trend into account in evaluating its seasonal variability (Soerensen et al., 2010a). Here we add a new ship cruise and adjust observed Hg^0 concentrations (Hg^0_{obs}) from all 19 ship cruises to Hg^0 levels consistent with year 2009 based on a fitted decline trend (Table 2.2 and Figure 2.4). Seasonal variation is estimated by dividing the normalized Hg^0 (Hg^0_{nor}) by month of measurement. As shown in Figure 2.5, Hg^0_{nor} are smaller and show less seasonal variability compared to Hg^0_{obs}.

Table 2.1. Information for ground-based observational sites of atmospheric mercury.

ID[a,b]	Location	Time period	Lat	Lon	Alt[c]	Network[d]
ALT	Alert, NU, Canada	2009	83	-62	210	1
ZEP	Zeppelin, Ny-Ålesund, Norway	2009-2011	79	12	474	2
ADY	Andøya, Norway	2010-2011	69	16	380	2
BKN	Birkenes, Norway	2010-2011	58	8	219	2
MHD	Mace Head, Ireland	2009-2011	53	-10	15	2
WLD	Waldhof, Germany	2009-2011	53	11	74	2
BRL	Bratt's Lake, SK, Canada	2009-2010	50	-105	587	1
SAT	Saturna, BC, Canada	2009-2010	49	-123	178	1
KEJ	Kejimkujik, NS, Canada	2009-2011	44	-65	158	3
EGB	Egbert, ON, Canada	2009-2010	44	-80	251	1
MBO	Mt. Bachelor, OR, USA	2009-2010	44	-122	2763	4
HTW	Huntington Wildlife Forest, NY, USA	2009-2011	44	-74	502	3
CBS	Mt. Changbai, JL, China	2008-2010	42	128	741	4
ATS	Athens Super Site, OH, USA	2009-2011	39	-82	274	3
SCZ	Santa Cruz, CA, USA	2010-2011	37	-122	150	3
WLG	Waliguan, QH, China	2007-2008	36	101	3816	4
YKV	Yorkville, GA, USA	2009-2011	34	-85	394	3
NMC	Nam Co Lake, XZ, China	2011-2013	31	91	4730	4
GRB	Grand Bay NERR, MS, USA	2009-2011	30	-88	1	3
SGR	Shangri-La, YN, China	2009-2010	28	100	3580	4
OKN	Okinawa, Japan	2009-2011	27	128	60	4
LUL	Mt. Front Lulin, Taiwan	2009-2011	24	121	2862	4
MLO	Mauna Loa, HI, USA	2011	20	-156	3384	3
NWN	Nieuw Nickerie, Suriname	2007-2008	6	-57	5	4
CPT	Cape Point, South Africa	2009-2011	-34	18	230	4
AMS	Amsterdam Island, Indian Ocean	2012-2013	-38	78	55	4
TRS	Troll Research Station, Antarctica	2009-2011	-72	3	1275	4

[a] Observational sites without original high-frequency observational data are: MBO, CBS, WLG, NMC, SGR, LUL, and NWN.

[b] Observational sites where we use TGM data are: ALT, BRL, SAT, EGB, CBS, WLG, NMC, SGR, and NWN. For all other sites, we use GEM data.

[c] Unit for altitude is meters.

[d] Network affiliations: (1) Canadian networks, (2) EMEP, (3) AMNet, and (4) Individual observational sites. More information about these individual sites can be found in Swartzendruber et al. (2006) for MBO, Fu et al. (2012b) for CBS, Fu et al. (2012a) for WLG, Zhang et al. (2015) for SGR, MOEJ (2013) for OKN, Sheu et al. (2010) for LUL, Müller et al. (2012) for NWN, Slemr et al. (2011) for CPT, Angot et al. (2014) for AMS, and Slemr et al. (2015) for the Southern Hemispheric sites.

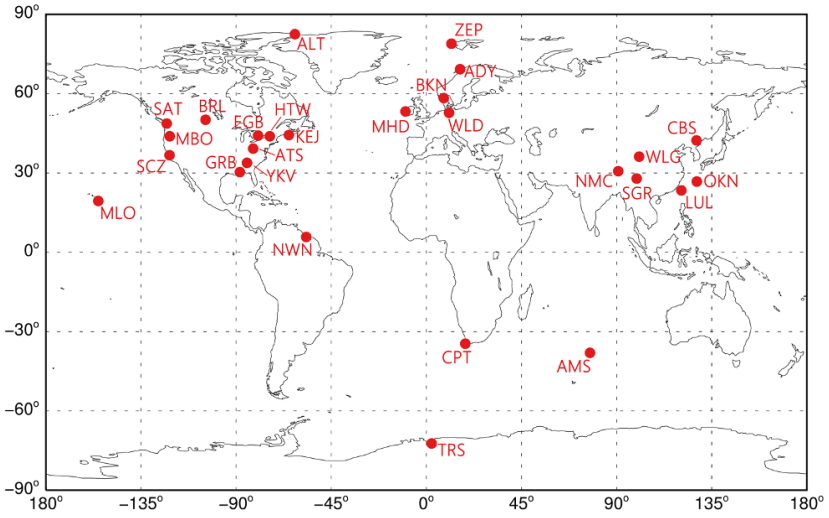

Figure 2.1. Locations of 27 ground-based observational sites of atmospheric mercury.

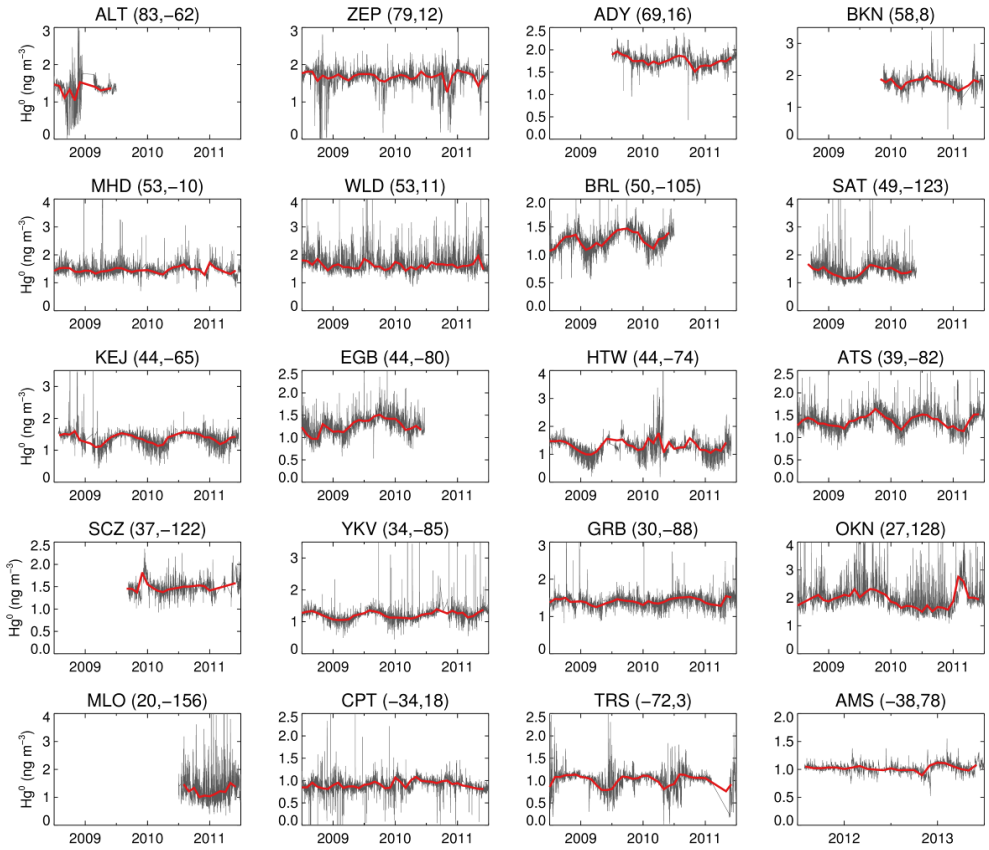

Figure 2.2. Hourly (grey) and monthly (red) concentrations of atmospheric mercury measured at ground-based sites. Note different scales on vertical axis.

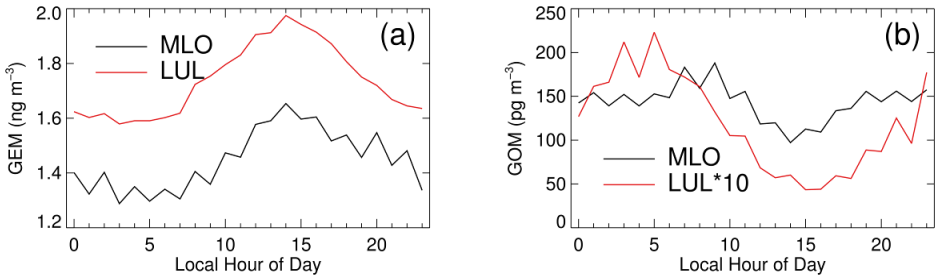

Figure 2.3. Diurnal variations of the average GEM and GOM concentrations measured at two mountain sites, Mauna Loa (MLO) and Mt. Lulin (LUL). Data for LUL are from Sheu et al. (2010). We estimate, for both sites, that the minimum hourly Hg^0 concentration at night is ~ 90% of the all-day average.

Table 2.2. Summary of over-water Hg^0 observational data in the North Atlantic Ocean. Unit is ng m^{-3}.

Year	Month	Latitude	Method	Hg^0_{obs}	Hg^0_{nor}	Ref.*
1990	Oct-Nov	7-54N	Manual	2.25	1.38	(1)
1993	Aug	50-68N	Manual	2.10	1.36	(2)
1994	Oct-Nov	6-54N	Manual	1.79	1.10	(1)
1996	Oct-Nov	8-67N	Tekran	2.12	1.52	(1)
1999	Sep	31-32N	Manual	2.03	1.57	(3)
1999	Dec	31-32N	Manual	2.06	1.60	(3)
1999	Dec	10-54N	Tekran	2.05	1.59	(1)
2000	Mar	31-32N	Manual	1.90	1.49	(3)
2003	Aug-Sep	10-37N	Tekran	1.63	1.35	(4)
2004	Jun-Aug	54-67N	Tekran	1.54	1.31	(5)
2005	Jul	60-62N	Tekran	1.78	1.60	(6)
2006	Aug	58-67N	Tekran	1.32	1.18	(7)
2007	Apr	43-59N	Tekran	2.26	2.17	(7)
2008	Nov	25-50N	Tekran	1.14	1.09	(8)
2008	Aug	35-45N	Tekran	1.40	1.35	(9)
2008	Sep	32-34N	Tekran	1.46	1.41	(9)
2009	Apr-May	25-50N	Tekran	1.15	1.15	(8)
2009	Jun	31-32N	Tekran	1.43	1.43	(9)
2009	Oct	35-45N	Tekran	1.40	1.40	(9)

*References: (1) Temme et al. (2003b); (2) Mason et al. (1998); (3) Mason et al. (2001); (4) Laurier and Mason (2007); (5) Aspmo et al. (2006); (6) Sommar et al. (2010); (7) Soerensen et al. (2010a); (8) Kuss et al. (2011); (9) Soerensen et al. (2013).

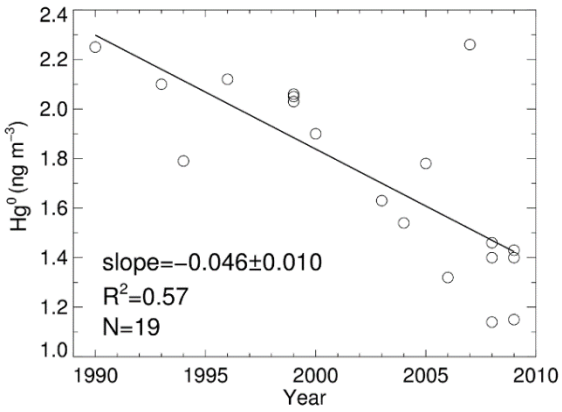

Figure 2.4. Decline of Hg^0 concentration calculated from 19 ship cruise measurements in 1990-2009.

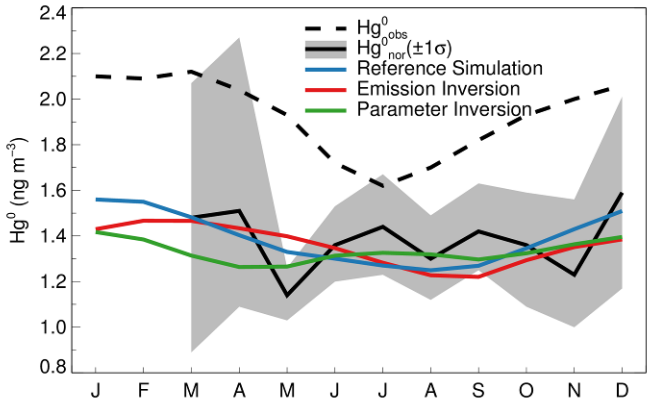

Figure 2.5. Observed and modeled monthly Hg^0 concentrations over the North Atlantic Ocean. The observational data and related references are given in the Supplement. Hg^0_{obs} are the concentrations observed from 19 ship cruises during 1990-2009, whereas Hg^0_{nor} are the concentrations normalized to levels consistent with year 2009. The gray shaded region shows one-sigma error of Hg^0_{nor}, which is composed of observational error, mismatch error, and regression error.

2.1.2 GEOS-Chem Global Mercury Model

GEOS-Chem (v9-02; *www.geos-chem.org*) is a CTM driven by assimilated meteorological fields from the NASA Goddard Earth Observing System (GEOS) (Bey et al., 2001). In this inverse modeling study, the original GEOS-5 has a resolution of 1/2°×2/3° and is degraded to 2°×2.5° for input into our global model simulations. For consistency with most ground-based

atmospheric mercury observations used in our inversion, we use meteorological years of 2009-2011 for analysis, after a spin-up period of 4 years.

The GEOS-Chem global mercury simulation was described and evaluated in Selin et al. (2007) and Strode et al. (2007), with updates by Selin et al. (2008), Holmes et al. (2010), Soerensen et al. (2010b), and Amos et al. (2012). It couples a three-dimensional atmosphere, a two-dimensional mixed layer slab ocean, and a two-dimensional terrestrial reservoir. Three mercury tracers (representing GEM, GOM, and PBM) are simulated in the atmosphere in GEOS-Chem. Models have assumed that Hg^0 is oxidized by OH, ozone, and/or halogens (De Simone et al., 2014; Durnford et al., 2010; Grant et al., 2014; Lei et al., 2013; Travnikov and Ilyin, 2009). Some studies suggested that gas-phase reaction with Br was the most important Hg^0 oxidation process globally (Hynes et al., 2009; Seigneur and Lohman, 2008; Gratz et al., 2015), and here we use Br as the only oxidant of Hg^0 (Holmes et al., 2010; Goodsite et al., 2012). Tropospheric Br fields are archived from a full chemistry GEOS-Chem simulation (Parrella et al., 2012). Models also hypothesize gas- and/or aqueous-phase reductions of oxidized Hg and scale their kinetics to match atmospheric observations (Pongprueksa et al., 2011; Holmes et al., 2010; Selin et al., 2007). However, an accurate determination of potential pathways is lacking (Subir et al., 2011, 2012), and their atmospheric relevance is unknown (Gårdfeldt and Jonsson, 2003). Thus we do not include atmospheric reduction of oxidized Hg in our global model simulations.

2.1.3 Emission Inversion: Reference Emission Fluxes

For our reference emissions, we use parameterizations in GEOS-Chem with improvements from recent literature. As shown in Table 2.3, global mercury emission is estimated as 6.0 Gg yr^{-1}, with an uncertainty range of 0.4-12.2 Gg yr^{-1}. Mercury released via natural processes is assumed to be entirely Hg^0 (Stein et al., 1996), while a small fraction of anthropogenic mercury is in oxidized forms. Anthropogenic emission is unidirectional, but air-surface exchange is bi-directional (emission and deposition) (Gustin et al., 2008; Xu et al., 1999). A positive net emission from a surface means it is a net source of Hg^0, whereas a negative value means it is a net sink. We describe below our reference emissions for individual sources.

Anthropogenic Sources. We use the anthropogenic emission inventory based on activity data for year 2010, developed by AMAP/UNEP (2013), as the reference emissions from anthropogenic sources in our inverse modeling. As shown in Table 2.3, the total global anthropogenic emission is 1960 Mg yr^{-1}, with an uncertainty range of 1010-4070 Mg yr^{-1}. We do not optimize oxidized mercury emissions (accounting for about 19% of the total anthropogenic sources) in part because this form has a short atmospheric lifetime (days to weeks) and may not significantly contribute to observed TGM concentrations and in part because we do not use oxidized mercury measurements in our inversion. The geospatial distribution for emissions from contaminated sites (Kocman et al., 2013) is not available for this inventory, and we distribute this small source (80 Mg yr^{-1}) based on the locations of mercury mines (Selin et al., 2007). We do not consider in-plume reduction of oxidized Hg emitted from coal-fired power plants (Zhang et al., 2012b). About 50% of global emissions are from Asia (defined as 65°E-146°E, 9°S-60°N), and a small fraction are from Europe and North America (together < 10%). For other regions like Africa and South America, there is no effective observational site to constrain emissions (Figure 2.1). Accordingly, only anthropogenic emissions from Asia are optimized in the inversion, but we still include other regions' anthropogenic emissions in the GEOS-Chem model simulations.

Table 2.3. Global mercury emissions into the atmosphere. Unit is Mg yr^{-1}.[a]

Source	Included in inversion?[b]	Reference emission	Optimized emission
Anthropogenic[c]		**1960 (420-3510)**	**2250 (1150-3360)**
Asia	Y	770 ± 390	1060 ± 110
Other regions	N	760	760
Contaminated sites	N	80 (70-100)	80 (70-100)
Oxidized Hg	N	350	350
Net ocean		**2990 (470-5510)**	**3160 (1160-5160)**
Net NH ocean	Y	1230 ± 630	1670 ± 530
Net SH ocean	Y	1760 ± 880	1490 ± 680
Net terrestrial[d]		**1070 (-510-3130)**	**340 (-590-1750)**
Soil	Y	1680 ± 840	860 ± 440
Prompt reemission	N	520	500
Hg^0 dry deposition	N	-1430	-1320
Geogenic	N	90 (60-600)	90 (60-600)
Biomass burning	N	210	210
TOTAL[e]		**6020 (380-12150)**	**5750 (1720-10270)**

[a] Flux values in parentheses indicate estimated uncertainty ranges. For sources included in the inversion, "average ± standard deviation" is shown. The uncertainty ranges of contaminated sites and geogenic emissions are from AMAP/UNEP (2013) and Mason (2009), respectively. If the uncertainty range of a source is not available, we assume that its standard deviation is a half of its best estimate.

[b] Only selected mercury emission sources are included in the inversion, see details in Section 2.1.3.

[c] Oxidized Hg emissions from anthropogenic sources are not included in the inversion. "Asia" and "Other regions" (except Asia) refer to emissions of Hg^0.

[d] As air-terrestrial interactions are bi-directional, we assume that uncertainties of prompt reemission and Hg^0 deposition have been covered by that of soil emission.

[e] Total mercury emissions are the sum of anthropogenic, net ocean, and net terrestrial emissions.

Ocean Evasion. The mixed layer (ML) slab ocean model in GEOS-Chem is described in Soerensen et al. (2010b). Net Hg^0 emission from ocean surfaces is determined by the supersaturation of Hg_{aq}^0 in the ML relative to the atmosphere and the air-sea exchange rate. Hg_{aq}^0 in the ML is mainly produced by the net photolytic and biotic reduction of Hg_{aq}^{2+}. Atmospheric deposition accounts for most Hg_{aq}^{2+} inputs into the ML, but subsurface waters also contribute a considerable fraction. The ML interacts with subsurface waters through entrainment/detrainment of the ML and wind-driven Ekman pumping. We improve several parameterizations in the current GEOS-Chem ocean model (Soerensen et al., 2010b) based on recent findings. (1) Basin-specific subsurface water mercury concentrations are updated according to new measurements (Figure 2.6). (2) Soerensen et al. (2010b) used the Wilke-Chang method for estimating the Hg_{aq}^0 diffusion coefficient (D_{Hg}) (Wilke and Chang, 1955), but this estimate was believed to be too high (Loux, 2004). We adopt a revised D_{Hg} derived by molecular dynamics (MD) simulation (Kuss et al., 2009). As shown in Figure 2.7, compared to the Wilke-Chang method, MD simulation obtains a D_{Hg} that agrees much better with recent laboratory results (Kuss, 2014). (3) Particulate mercury (Hg_{aq}^P) sinking from the ML is estimated by linking the organic carbon export (biological pump) and Hg_{aq}^P:C ratios. Soerensen et al. (2010b) used the model of Antia et al. (2001) for estimating carbon export fluxes, giving a global total of 23 Gt C yr^{-1}. However, this estimate is mainly based on the flux measurement data from much deeper depths and may not well represent carbon export from the ML. Different models suggest global carbon export fluxes ranging from 5-20 Gt C yr^{-1} with a best estimate of 11 Gt C yr^{-1} (Henson et al., 2011; Sanders et al., 2014). Thus, we multiply carbon export fluxes in GEOS-Chem by a factor of 0.47 (11 Gt C yr^{-1}/23 Gt C yr^{-1}) to match this best estimate. Net global ocean emission of 2990 Mg yr^{-1} from the improved GEOS-Chem (considered as

reference emission, shown in Table 2.3) compares favourably with best estimates of 2680 Mg yr^{-1} using a bottom-up approach (Mason, 2009; Pirrone et al., 2010). Due to their different seasonal characteristics, we divide the global ocean into the NH (northern hemisphere) and SH (southern hemisphere) oceans, and optimize their emissions separately.

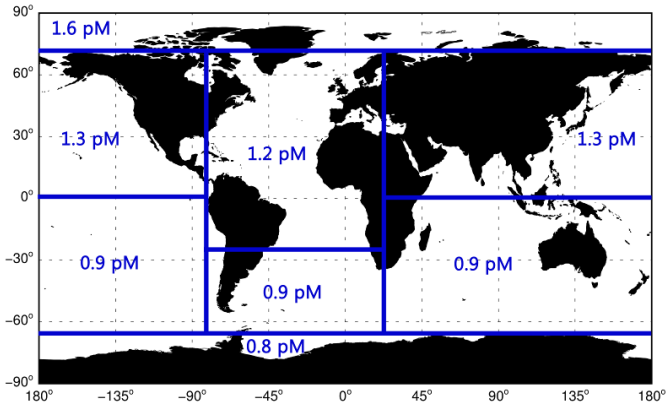

Figure 2.6. Subsurface water concentrations of inorganic mercury used in our GEOS-Chem modeling. These basin-specific data are compiled by Soerensen et al. (2010b) and updated based on new measurements. The Hg concentration in the North Atlantic Ocean (NAO) is reduced from 1.8-2.0 pM to 1.2 pM, according to the vertical profiles measured at the Bermuda Atlantic Time Series (BATS, 31°40'N 64°10'W) in June 2008 (Lamborg et al., 2012). Mercury concentration in the South Atlantic Ocean (SAO) is reduced to 0.9 pM, at the low end of uncertainty range by Sunderland and Mason (2007). The southern boundary of the North Pacific (NP), where mercury concentration is set as 1.3 pM, is extended to the equator since Munson et al. (2015) measured total mercury concentration of 1-1.5 pM in the Tropical Pacific Ocean.

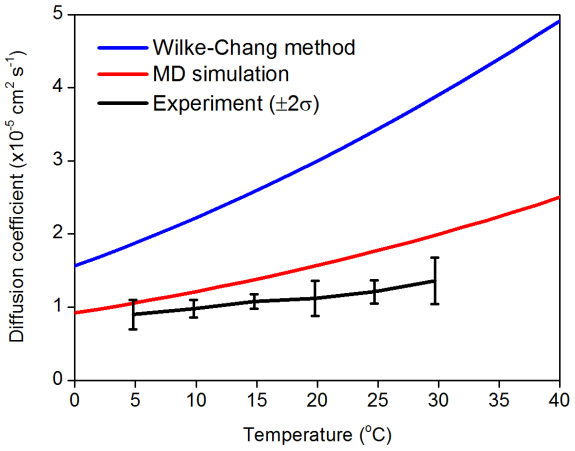

Figure 2.7. Comparison of the Hg^0 diffusion coefficients (DHg) in seawater. They are determined by the Wilke-Chang method (Wilke and Chang, 1955), MD (molecular dynamics) simulation (Kuss et al., 2009), and the laboratory experiment (Kuss, 2014), respectively. The Wilke-Chang method can be found in Soerensen et al. (2010b). The parameterization of the MD simulation is DHg (cm^2 s^{-1}) = $0.02293 \times e^{(17.76\ kJ/mol)/RT}$, with R the gas constant and T the temperature in K.

Terrestrial Ecosystem. GEOS-Chem treats the emission and deposition fluxes of Hg^0 separately. Only dry deposition is considered for Hg^0 due to its low Henry's law constant (Lin and Pehkonen, 1999). As shown in Equation (2.1), the net emission from terrestrial surfaces (E_{net}) represents the sum of these processes: volatilization from soil (E_{soil}), prompt reemission of deposited Hg (E_{pr}), geogenic activity (E_{gg}), biomass burning (E_{bb}), and dry deposition to surfaces (E_{ddHg0}).

$$E_{net} = E_{soil} + E_{pr} + E_{gg} + E_{bb} - E_{ddHg0} \tag{2.1}$$

Soil emission (E_{soil}) is specified as a function of solar radiation and soil Hg concentration.

$$E_{soil}\ (\text{ng m}^{-2}\ \text{h}^{-1}) = \beta\ C_{soil} \exp(1.1\times10^{-3} \times R_g) \tag{2.2}$$

where C_{soil} is soil Hg concentration (ng g^{-1}) and R_g is the solar radiation flux at the ground (W m^{-2}). GEOS-Chem assumes a global average soil concentration of 43 ng g^{-1} for preindustrial conditions and derives its spatial distribution from the local equilibrium between emission and deposition. The scaling factor β (1.2×10^{-2} g m^{-2} h^{-1}) is obtained from the global mass balance of the preindustrial simulation. Selin et al. (2008) assumed that present-day soil mercury reservoir and emission have both increased by 15% compared to preindustrial period, and distributed this global average increase according to the present-day deposition pattern of anthropogenic emission. However, by linking soil mercury with organic carbon pools, Smith-Downey et al. (2010) estimated that present-day Hg storage in organic soils has increased by 20% while soil emission by 190%. Mason and Sheu (2002) suggested doubled soil emissions compared to preindustrial times. Thus, following Smith-Downey et al. (2010), we assume a 190% global increase in the present-day soil emission, and distribute this increase according to the anthropogenic emission deposition pattern. The present-day reference soil emission is calculated to be 1680 Mg yr^{-1}. An additional 520 Mg Hg yr^{-1} is emitted from the soil, vegetation, and snow (E_{pr}) through rapid photoreduction of recently deposited oxidized Hg (Fisher et al., 2012; Holmes et al., 2010). Geogenic emission (E_{gg}) is set as 90 Mg yr^{-1}, consistent with its best bottom-up estimate (Bagnato et al., 2014; Mason, 2009). Biomass burning (E_{bb}) of 210 Mg yr^{-1} is estimated using the Global Fire Emissions Database version 3 of CO (van der Werf et al.,

2010) and a Hg:CO ratio of 100 nmol mol^{-1} (Holmes et al., 2010). This amount falls at the lower end of bottom-up estimates (Friedli et al., 2009). Dry deposition of Hg^0 is estimated using a resistance-in-series scheme (Wesely, 1989) and has a downward flux of 1430 Mg yr^{-1}. Using Equation (2.1), the net emission of Hg^0 from terrestrial ecosystem surfaces is calculated to be 1070 Mg yr^{-1} in GEOS-Chem (Table 2.3), which is found at the lower end of the bottom-up estimates (1140-5280 Mg yr^{-1}) (Mason, 2009; Pirrone et al., 2010), and also lower than 1910 Mg yr^{-1} by Kikuchi et al. (2013) using a different empirical mechanism (Lin et al., 2010).

Sources Included in Emission Inversion. Because of limitations in both observations and the CTM, only anthropogenic emission from Asia, ocean evasion (separated into the NH and SH), and soil emission are optimized in the emission inversion (Table 2.3). The remaining sources are still included in the simulation but not inverted because they are too diffusely distributed, their magnitude is small, and/or observations are not sensitive to them (Chen and Prinn, 2006). The seasonal sources (the NH ocean, SH ocean, and soil) usually have strong spatiotemporal variations and the inversion optimizes their monthly magnitudes and uncertainties. For the aseasonal Asian anthropogenic emission, the inversion optimizes its annual magnitude and uncertainty.

2.1.4 Bayesian Inversion Method

We use a Bayesian method to invert emissions and parameters with a weighted least-squares technique (Ulrych et al., 2001). The unknowns (correction factors for reference emissions and parameters) are contained in a state vector $\boldsymbol{x}$ and their *a priori* errors (uncertainties in reference emissions and parameters) in a matrix **P**. In the emission inversion, as we include one aseasonal source (Asian anthropogenic emission) and three monthly sources (the NH ocean, SH ocean, and soil), the vector $\boldsymbol{x}$ contains 37 elements. **P** is a 37x37 diagonal matrix with each diagonal element equal to the square of one-sigma *a priori* error of the corresponding element in $\boldsymbol{x}$ (see Section 2.1.6).

Our inversion method assumes a linear relationship between the observation vector $\boldsymbol{y}^{\mathbf{obs}}$ and $\boldsymbol{x}$, as shown in the Measurement Equation (2.3):

$$\boldsymbol{y}^{\mathbf{obs}} = \boldsymbol{y}^{\mathbf{ref}} + \mathbf{H}\boldsymbol{x} + \boldsymbol{\varepsilon} \tag{2.3}$$

where $\boldsymbol{y}^{\mathbf{ref}}$ contains monthly Hg^0 concentrations modeled by GEOS-Chem using the reference emissions and parameters. The vectors $\boldsymbol{y}^{\mathbf{obs}}$ and $\boldsymbol{y}^{\mathbf{ref}}$ both have 12 (number of months per year) × 27 (number of observational sites) = 324 elements. $\boldsymbol{\varepsilon}$ represents model and observational errors which will be discussed in detail in Section 2.1.6. The state vector $\boldsymbol{x}$ is related to monthly Hg^0 concentrations by the sensitivity matrix **H**, in which the elements are written as:

$$\mathbf{h}_{\mathbf{ij}} = (\boldsymbol{y}_{\mathbf{i}} - \boldsymbol{y}_{\mathbf{i}}^{\mathbf{ref}})/(\boldsymbol{x}_{\mathbf{j}} - \boldsymbol{x}_{\mathbf{j}}^{\mathbf{ref}}) \approx \partial \boldsymbol{y}_{\mathbf{i}}/\partial \boldsymbol{x}_{\mathbf{j}} \tag{2.4}$$

where **i** and **j** are indices for the observational and state vectors, respectively. **H** describes how monthly Hg^0 concentrations at different observational sites respond to changes in the state vector $\boldsymbol{x}$ (for examples see Figure 2.8). The GEOS-Chem CTM acts as a mathematical operator relating the emissions/parameters to monthly Hg^0 concentrations. For the emission inversion, sensitivities for the seasonal and aseasonal sources are generated by two different types of simulations. The aseasonal Asian anthropogenic emission is perturbed above the reference level by 50%, and we run the GEOS-Chem CTM until steady state is reached. For the seasonal sources (e.g. the NH ocean emission from March), a one-month pulse of Hg^0 is emitted, and we track modeled Hg^0 concentrations by GEOS-Chem for the next three years. After this, we assume that the perturbed concentrations at all observational sites will exponentially decrease (Saikawa et al., 2012). The objective function **J** with respect to $\boldsymbol{x}$ is calculated in Equation (2.5):

$$\mathbf{J}(\boldsymbol{x}) = \boldsymbol{x}^{\mathrm{T}}\mathbf{P}^{-1}\boldsymbol{x} + (\mathbf{H}\boldsymbol{x} - \boldsymbol{y}^{\mathbf{obs}} + \boldsymbol{y}^{\mathbf{ref}})^{\mathrm{T}}\mathbf{R}^{-1}(\mathbf{H}\boldsymbol{x} - \boldsymbol{y}^{\mathbf{obs}} + \boldsymbol{y}^{\mathbf{ref}}) \tag{2.5}$$

where **R**, a diagonal 324×324 matrix, represents errors related to observations and the CTM and will be described in detail in Section 2.1.6. By minimizing **J**, we obtain the expression for the optimal estimate of the state $\boldsymbol{x}$ (Equation (2.6)):

$$\boldsymbol{x} = (\mathbf{H}^{\mathrm{T}}\mathbf{R}^{-1}\mathbf{H} + \mathbf{P}^{-1})^{-1}\mathbf{H}^{\mathrm{T}}\mathbf{R}^{-1}(\boldsymbol{y}^{\mathbf{obs}} - \boldsymbol{y}^{\mathbf{ref}}) \tag{2.6}$$

$$\mathbf{Q} = (\mathbf{H}^{T}\mathbf{R}^{-1}\mathbf{H} + \mathbf{P}^{-1})^{-1} \quad (2.7)$$

where the matrix **Q** contains the *a posteriori* errors of $\boldsymbol{x}$. The size of **Q** is the same as the matrix **P**. Each diagonal element in **Q** is the square of one-sigma *a posteriori* error of the corresponding element in $\boldsymbol{x}$. A detailed mathematical derivation of the above equations can be found in Wunsch (2006). As shown in Equations (2.6) and (2.7), several vectors and matrices need to be calculated during the optimization procedure, including the observational vector $\boldsymbol{y}^{\mathbf{obs}}$ and its error matrix **R**, the error matrix **P** of the *a priori* state, the sensitivity matrix **H**, and the vector $\boldsymbol{y}^{\mathbf{ref}}$ which is obtained from the reference simulation of the GEOS-Chem CTM.

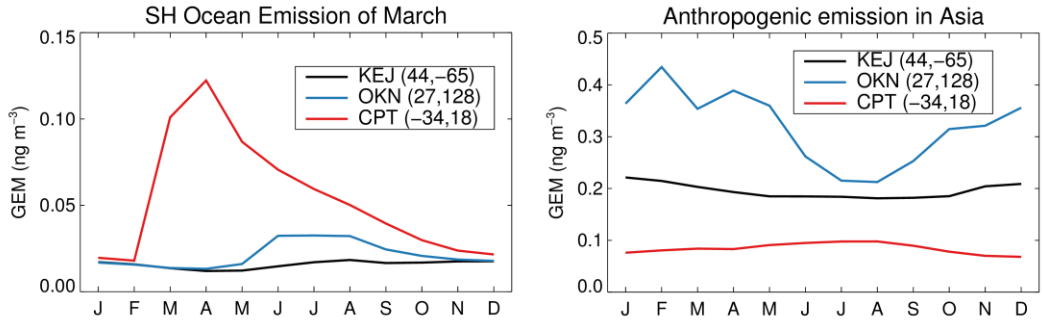

Figure 2.8. Sensitivities of monthly Hg^0 concentrations at three ground-based observational sites to changes in different sources: (left) the SH ocean emission in March and (right) anthropogenic emission in Asia. The sensitivities of the simulated GEM concentrations at different surface stations are calculated by perturbing the SH ocean emission of March and the anthropogenic emission in Asia by 100%. The SH ocean emission in March has larger sensitivities in the SH site CPT than the two NH sites (KEJ and OKN). The sensitivities at CPT exhibit an exponential decay starting from March-April. The anthropogenic emission in Asia has the largest sensitivities in OKN, which is located in the Asia-Pacific region. The smallest sensitivities are found for the SH site CPT because the Asian emissions are predominantly from the NH.

2.1.5 Parameter Inversion: *A Priori*

Based on the results of ocean evasion in our emission inversion and the sensitivity tests of model parameters, we identify two ocean parameters in GEOS-Chem for improvement: the rate constant of dark oxidation of Hg_{aq}^0 (denoted as K_{OX2}, following notations in Soerensen et al. (2010b)) and the partition coefficient between Hg_{aq}^{2+} and Hg_{aq}^{P} (denoted as K_D). For simplicity they are expressed in decimal logarithms (-log K_{OX2} and log K_D).

Below we summarize the results from previous laboratory studies for -log K_{OX2}. Amyot et al. (1997) first showed that seawater Hg_{aq}^0 could undergo rapid oxidation in dark conditions. They collected seawater samples from the Gulf of Mexico, spiked them with known amounts of Hg_{aq}^0, and measured time series of Hg_{aq}^0 and total aqueous Hg. A first-order rate constant of (2.5–3.3) × 10^{-5} s^{-1} (i.e., -log K_{OX2} = 4.5–4.6) for dark oxidation was obtained. This rate was considered to be unreliable because other Hg_{aq}^0 loss pathways also existed, including volatilization from solution and adsorption on container wall. Using a similar method, Lalonde et al. (2001) indicated that the first-order reaction rate of dark oxidation in the Baie Saint-Paul river water was 1.7 × 10^{-5} s^{-1} (-log K_{OX2} = 4.8). Lalonde et al. (2004) measured no significant loss of Hg_{aq}^0 under a dark environment. However, they observed dark oxidation of Hg_{aq}^0 with a rate of 8.3 × 10^{-6} s^{-1} (-log K_{OX2} = 5.1) if the natural water had been irradiated by ultraviolet light for 2 hours before being kept in the dark. Qureshi et al. (2010) proposed two possible redox pathways for surface ocean Hg. Both pathways included relatively high reaction rates of dark oxidation, i.e., (0.9–2.2) × 10^{-4} s^{-1} (-log K_{OX2} = 3.7–4.0) and (1.1–2.6) ×10^{-4} s^{-1} (-log K_{OX2} = 3.6–4.0). They noted that the two dark oxidation rate constants were likely to be upper limits. In short, we find from these studies that the rate constants of dark oxidation (K_{OX2}) may range from 10^{-6} to 10^{-4} s^{-1} (i.e., -log K_{OX2} = 4.0–6.0). In comparison, a -log K_{OX2} (s^{-1}) of 7.0 is specified in GEOS-Chem (Soerensen et al., 2010b). Thus we suggest that this value is too low and that a more appropriate range of -log K_{OX2} is 4.0–6.0. The chemical mechanisms for dark oxidation of Hg_{aq}^0 remain unclear. OH generated from photochemically produced H_2O_2 via the Fenton reaction may oxidize Hg_{aq}^0 in dark conditions (Zepp et al., 1992; Zhang and Lindberg, 2001). Light irradiation before a dark period is needed, and dark oxidation kinetics depend on intensity and duration of light (Batrakova et al., 2014; Qureshi et al., 2010). Future work could include a more mechanistic representation of this process as laboratory studies become available.

K_D (=C_s/C_dC_{SPM}) describes the affinity of aqueous Hg^{2+} for suspended particulate matter (SPM), where C_s, C_d, and C_{SPM} are the concentrations of Hg_{aq}^P, Hg_{aq}^{2+}, and SPM, respectively. GEOS-Chem uses a log K_D (L kg^{-1}) of 5.5 based on measurements in North Pacific and North Atlantic Ocean (Mason and Fitzgerald, 1993; Mason et al., 1998).

In the parameter inversion, we attempt to constrain these two ocean model parameters using the Bayesian approach described in Section 2.1.4. For consistency with sources in the

emission inversion, two other parameters are included, i.e. emission ratios for soil (ER_{Soil}) and Asian anthropogenic sources (ER_{Asia}). It is noted that the emission inversion and parameter inversion are carried out separately. Because the responses of Hg^0 concentrations to changes in ocean parameters are nonlinear, as shown in Figure 2.9, we use a two-step iterative inversion method (Prinn et al., 2011). At each iteration step, the sensitivity matrix **H** is estimated by linearizing the nonlinear function around the current parameter estimate. In the parameter inversion, the state vector ***x*** contains four elements (corresponding to the four parameters), and **P** and **Q** are 4 × 4 matrices.

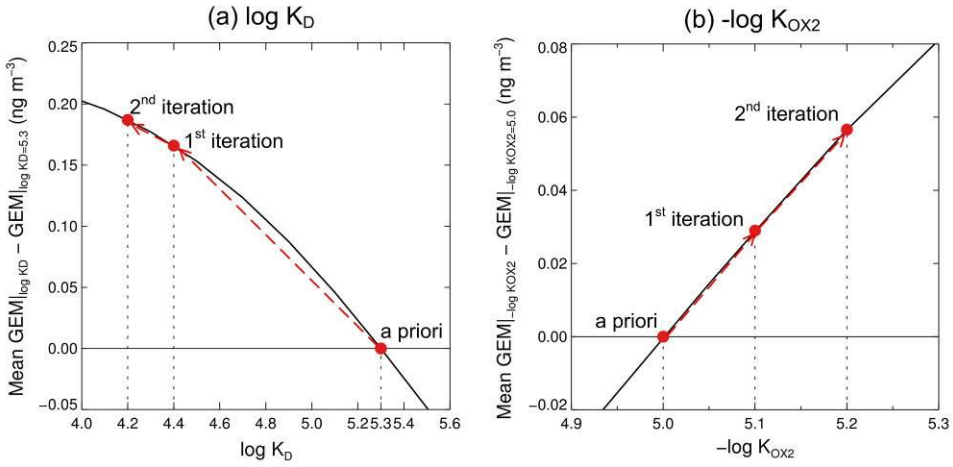

Figure 2.9. Responses of Hg^0 concentrations to changes of the partition coefficient (log K_D) (panel a) and dark oxidation rate constant (-log K_{OX2}) (panel b). We also show in the figure the evolution of the two parameters from the *a priori* to *a posteriori* estimate. See the assumptions of uncertainties associated with the parameters in Table 2.6.

2.1.6 Error Representation

Successful estimation of ***x*** (Equation (2.6)) and its uncertainty **Q** (Equation (2.7)) depends on reasonable representations of all relevant errors, including the *a priori* errors associated with reference emissions/parameters (contained in **P**) and errors related to Hg^0 observations and the CTM (contained in **R**). **R** should consist of three parts: observational errors, model-observation mismatch errors, and model errors.

Errors in Reference Emission and Parameters. We set the one-sigma errors in reference emissions as 50% in order to match uncertainties in their estimates using bottom-up approaches (see Table 2.3). For example, the reference emissions and one-sigma errors for the NH and SH

oceans are 1230 ± 630 and 1760 ± 880 Mg yr^{-1}, respectively. The uncertainty range of reference emission from the global ocean is estimated as 470-5510 Mg yr^{-1}, comparing very well with 780-5280 Mg yr^{-1} from bottom-up estimates (Mason, 2009; Pirrone et al., 2010). For the parameter inversion, the *a priori* estimates of two ocean model parameters are taken from literature reviews (Batrakova et al., 2014): -log K_{OX2} (5.0 ± 1.0) and log K_D (5.3 ± 0.4). The *a priori* uncertainties of ER_{Soil} and ER_{Asia} are chosen as 50%, the same as in the emission inversion.

Observational Errors. Observational errors for ground-based sites determine their relative importance in deriving the optimized state. As shown in Equation (2.8), the total observational errors (σ_{TOT}) contain instrumental precision (σ_{IP}), intercomparison (σ_{IC}), and sampling frequency errors (σ_{SF}) (Chen and Prinn, 2006; Rigby et al., 2012). Table 2.4 shows observational errors at each site, averaged over 2009-2011.

$$\sigma_{TOT} = \sqrt{\sigma_{IP}^2 + \sigma_{IC}^2 + \sigma_{SF}^2} \tag{2.8}$$

The instrumental precision (σ_{IP}) of high-frequency Hg^0 measurements using the Tekran instrument is usually reported by the mercury measurement studies to be ~ 2% (Poissant et al., 2005; Fu et al., 2010). Here, in our inverse modeling, an intercomparison error (σ_{IC}) is used to represent the comparability of Hg^0 concentrations measured by different research groups using the Tekran instrument. In principle, it includes several inaccuracies during the measurement process (e.g. the instrument's flow control and the permeation source rate for the automated calibration) and also arises from the different data management and quality control protocols taken by different research groups (Steffen et al., 2012). Its value has been assessed in several field intercomparisons (Aspmo et al., 2005; Ebinghaus et al., 1999; Munthe et al., 2001; Schroeder et al., 1995; Temme et al., 2006). Hg^0 concentrations measured by different laboratories have a relative standard deviation of reproducibility of 1-9%, and we choose a uniform intercomparison error (σ_{IC}) of 10%. Sampling frequency error (σ_{SF}) reflects the ability of each site to capture the overall variability of Hg^0 concentration in one month, and is calculated as the monthly standard deviation divided by the square root of the number of valid hourly data points in this month (Rigby et al., 2012). As shown in Table 2.4, the total

observational errors are dominated by intercomparison errors. The other two types of errors have much smaller contributions. Thus the total observational errors of Hg^0 concentration for ground-based sites are only a little larger than 10%. It is important to note that the total observational errors that we calculate here not only refer to random uncertainties but primarily to systematic uncertainties, i.e. biases (Slemr et al., 2015). However, due to the lack of the bias information (from available field intercomparisons) for the specific instrument used at each site, we are not able to compensate the biases in Hg^0 observation. Therefore, research aimed at quantifying and reducing the biases should be given high priority by the mercury measurement community.

Model-Observation Mismatch Errors. The mismatch error (σ_{MM}) exists because an observation is made at a single point in space but its corresponding grid box in model represents a large volume of air. We estimate σ_{MM} as the standard deviation of monthly Hg^0 concentrations in the eight surrounding grid boxes (at the same vertical layer) from the reference simulation, following the method in Chen and Prinn (2006). As shown in Table 2.4, σ_{MM} are larger over strongly emitting continental areas (e.g. SGR and WLG) and smaller over remote marine areas (e.g. CPT and AMS).

Model Errors. All existing CTMs, including GEOS-Chem are imperfect, due to both errors in meteorological data driving the CTMs and errors induced by their parameterizations of physical and chemical processes. The former type of model errors is termed "forcing errors" and the latter "process errors" (Locatelli et al., 2013). Physical processes consist of horizontal and vertical resolution, advection and convection, turbulence, planetary boundary layer mixing, etc. The CTM for Hg is subject to large process errors due to highly uncertain atmospheric chemistry. Recent studies have showed that Br concentration may be significantly underestimated in GEOS-Chem (Gratz et al., 2015; Parrella et al., 2012; Shah et al., 2016) and that current Br-initiated oxidation mechanisms are incomplete in describing all possible radical reactions (Dibble et al., 2012; Wang et al., 2014a). In order to provide a preliminary assessment of the effect of Br oxidation chemistry on our inversion, we perform an additional parameter inversion including six new elements in the state vector $\boldsymbol{x}$, and each of them represents Br columns in a 30° latitudinal band (see results in Section 2.3). Quantifying model errors requires incorporating many CTMs which are driven by different meteorology and which contain

different parameterizations (Prinn, 2000). Several multi-CTM intercomparison studies have been performed for CO_2 and CH_4 (Baker et al., 2006; Gurney et al., 2002; Locatelli et al., 2013), suggesting that model errors can impact their inverted emissions. Few other global CTMs exist for Hg (Bullock et al., 2008, 2009). Due to our inability to quantify model errors using a single CTM, model errors are not incorporated in our inversion, like many other inverse studies (Huang et al., 2008; Rigby et al., 2012; Xiao et al., 2010). As a result, **R** only includes observational errors and model-observation mismatch errors.

Table 2.4. Uncertainty information for each ground-based observational site. Unit for observational errors is pg m^{-3} unless otherwise stated.

ID	Average concentration*	Observational errors			Mismatch error (σ_{MM})	NRMSE		
		σ_{IP}	σ_{IC}	σ_{SF}		Reference simulation	Emission inversion	Parameter inversion
ALT	1.3	28	138	3	36	0.06	0.03	0.02
ZEP	1.7	34	169	6	14	0.13	0.19	0.18
ADY	1.8	36	181	4	13	0.16	0.22	0.23
BKN	1.8	36	178	6	32	0.19	0.22	0.24
MHD	1.5	29	145	5	8	0.08	0.08	0.09
WLD	1.6	33	163	10	114	0.14	0.10	0.12
BRL	1.3	25	127	5	23	0.18	0.11	0.13
SAT	1.4	28	140	8	28	0.16	0.12	0.13
KEJ	1.4	28	138	6	14	0.07	0.05	0.09
EGB	1.3	25	126	5	49	0.21	0.11	0.11
MBO	1.3	26	128	6	10	0.04	0.04	0.06
HTW	1.3	26	131	8	29	0.13	0.06	0.08
CBS	1.6	32	160	14	134	0.17	0.16	0.23
ATS	1.4	28	137	6	39	0.17	0.04	0.07
SCZ	1.5	30	148	5	23	0.07	0.05	0.04
WLG	1.9	38	188	20	223	0.21	0.26	0.24
YKV	1.2	24	122	6	48	0.30	0.15	0.13
NMC	1.2	25	124	6	23	0.07	0.06	0.07
GRB	1.4	28	141	5	41	0.08	0.07	0.08
SGR	2.5	50	250	30	544	0.37	0.40	0.37
OKN	1.9	39	195	13	37	0.24	0.24	0.22
LUL	1.4	29	145	12	52	0.12	0.13	0.13
MLO	1.2	25	123	16	8	0.11	0.13	0.11
NWN	1.3	25	126	22	105	0.22	0.13	0.18
CPT	0.9	18	91	4	13	0.26	0.08	0.16
AMS	1.0	21	103	3	7	0.16	0.08	0.07
TRS	1.0	22	107	3	33	0.15	0.13	0.09
AVG.		29	146	8	63	0.16	0.13	0.14

* The unit of average Hg0 concentration is ng m-3. Equation of NRMSE (quantity without unit) is given in Section 2.2.1.

2.2 Emission Inversion: Results

2.2.1 Model-Observation Comparison

We first test whether the comparison between ground-based Hg^0 observations and model outputs improves when using optimized emissions, compared to reference emissions. Figure 2.10 shows the modeled and observed Hg^0 concentrations at all 27 sites. In order to quantify model performance, we calculate the normalized root mean square error (NRMSE) for each site:

$$\mathrm{NRMSE} = \sqrt{\frac{1}{n}\sum_{i=1}^{n}\left(X_{\mathrm{obs},i} - X_{\mathrm{mod},i}\right)^2} \Bigg/ \frac{1}{n}\sum_{i=1}^{n} X_{\mathrm{obs},i} \tag{2.9}$$

where $X_{\mathrm{obs},i}$ and $X_{\mathrm{mod},i}$ are the observed and modeled Hg^0 concentrations at the ith month (n in total), respectively. As shown in Table 2.4, an average NRMSE of 0.13 is obtained for the emission inversion, smaller than that of 0.16 for the reference simulation, indicating that the emission inversion can better reproduce ground-based observations. While this is a relatively small uncertainty reduction (-0.03), we do not expect better performance for our inversion. This is because the total errors involved (as described above, and in Table 2.4) are ~ 13%, which constrain the optimization. Our inversion brings the average NRMSE within the observation error.

The NRMSEs are not reduced for all 27 sites (see Table 2.4). For three Nordic sites (ZEP, ADY, and BKN) and four Asia-Pacific sites (WLG, SGR, LUL, and MLO), the NRMSEs increase. Hg^0 concentrations are ~ 1.8 ng m^{-3} at the three Nordic sites, higher than the modeled values (Figure 2.10) from both reference simulation and emission inversion, and also higher than those measured at many background sites in Europe (Ebinghaus et al., 2011; Kentisbeer et al., 2014; Weigelt et al., 2013). Part of the differences may be explained by a positive bias in the instrumentation of these Nordic observations when compared to other laboratories (Temme et al., 2006). It is also possible that GEOS-Chem cannot sufficiently capture local meteorology and/or emissions at these sites. For the Asia-Pacific sites, the reference simulation

underestimates Hg^0 at SGR (-32%, calculated as $(\mathbf{y^{ref}}/\mathbf{y^{obs}} - 1) \times 100\%$, hereinafter the same) and WLG (-19%), and predicts comparable values at MLO (+2%) and LUL (+0%). Such discrepancies likely arise from unknown intercomparison errors and influence by local emission and meteorology factors not captured by the CTM (Fu et al., 2012b; Wan et al., 2009). These sites are operated by three different laboratories, but to the best of our knowledge, no field intercomparisons have been conducted among these laboratories.

Figure 2.11 compares the monthly Hg^0 observations with model simulations for sites aggregated into four regions: Asia-Pacific, North America, Europe, and Southern Hemisphere (SH). The emission inversion significantly improves the comparison for the SH sites (CPT, AMS, and TRS). In the reference simulation, Hg^0 concentrations at the SH sites vary seasonally, with a high in austral winter (~ 1.3 ng m^{-3}) and a low in austral summer (~ 0.9 ng m^{-3}). However, observed Hg^0 shows little seasonal variation with monthly concentrations of ~ 1.0 ng m^{-3}. The emission inversion reduces Hg^0 concentration in austral winter and fits the observations much better (the average NRMSE decreases from 0.19 to 0.10). As shown in Figure 2.10, all three SH sites show improvement after optimization.

The emission inversion also improves the comparison for sites in North America (the average NRMSE decreases from 0.13 to 0.08). Hg^0 data at a total of 11 sites are available, including five coastal sites (ALT, SAT, KEJ, SCZ, and GRB), five inland sites (BRL, EGB, HTW, ATS, and YKV), and one mountain-top site (MBO) (see Table 2.1 and Figure 2.1). Hg^0 at the coastal and inland sites are observed to be 1.41 ± 0.04 and 1.29 ± 0.06 ng m^{-3}, respectively. This coastal-inland difference in observation is consistent with results of Cheng et al. (2014), who found that air masses from open ocean at the site KEJ had 0.06 ng m^{-3} higher Hg^0 concentrations than those originating over land. The reference simulation and emission inversion both obtain comparable Hg^0 concentrations at the coastal sites (1.43 ± 0.06 and 1.38 ± 0.07 ng m^{-3}). At the inland sites, the emission inversion predicts Hg^0 concentrations (1.38 ± 0.03 ng m^{-3}) closer to observations than the reference simulation (1.50 ± 0.06 ng m^{-3}).

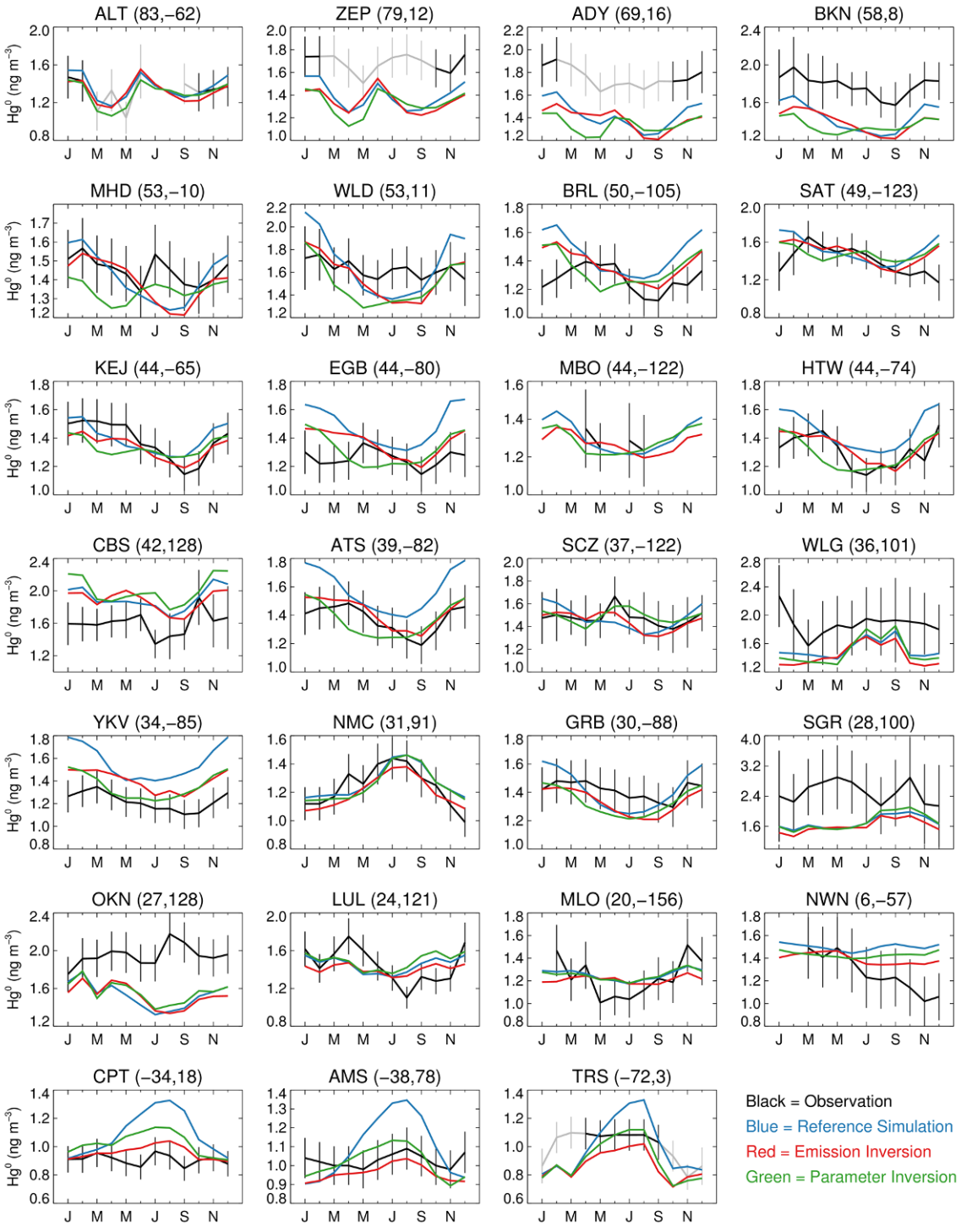

Figure 2.10. Monthly Hg^0 concentrations for all ground-based observational sites. Note different scales on vertical axes. Error bars correspond to the total errors described in Section 2.1.6. The two numbers in parentheses after the name of each site are its latitude and longitude. For polar sites (ALT, ZEP, ADY, and TRS), the gray color shows the observed Hg^0 concentrations that are not used in our inversions due to AMDEs.

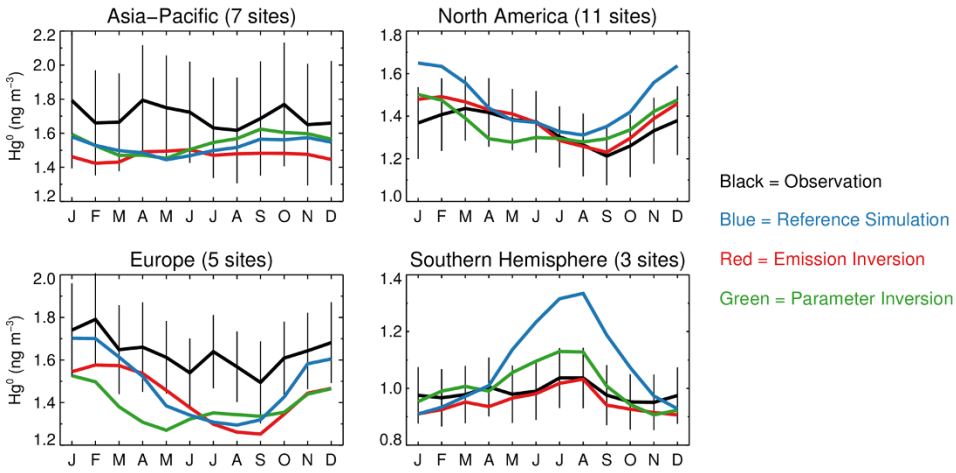

Figure 2.11. Averaged monthly observations and model simulations of Hg^0 concentrations for the ground-based observational sites in the four regions. They are Asia-Pacific: 45°E-140°W 0°-90°N, North America: 140°W-45°W 15°N-90°N, Europe: 15°W-45°E 15°N-90°N, and the Southern Hemisphere. Note different scales on vertical axes. Hg^0 observations are shown with total errors as described in Section 2.1.6.

Over-water Hg^0 observations serve as an independent test of the emission inversion. As shown in Figure 2.5, Hg^0 concentrations over the North Atlantic Ocean from both the reference simulation and the emission inversion fall within one-sigma uncertainty ranges of Hg^0_{nor}. The NRMSEs for the reference simulation and the emission inversion are 0.09 and 0.10, respectively. Thus using Hg^0 emissions constrained by ground-based observations, GEOS-Chem still matches these regional over-water observations.

We additionally test performance of the inversion by comparison with regional wet deposition data. Since most oxidized Hg is formed from the oxidation of Hg^0, changing Hg^0 emissions may have an effect on modeled oxidized Hg and its subsequent deposition. We compare model results to the observed wet deposition fluxes from NADP/MDN (2012), as shown in Figure 2.12. We use the monitoring sites active in 2009-2011 (n = 126). Both the reference simulation and the emission inversion fit observations well ($R \approx 0.7$, $NRMSE \approx 0.3$, see Figure 2.12). Accordingly, the effect of the inversion on the NADP/MDN wet deposition fluxes is insignificant.

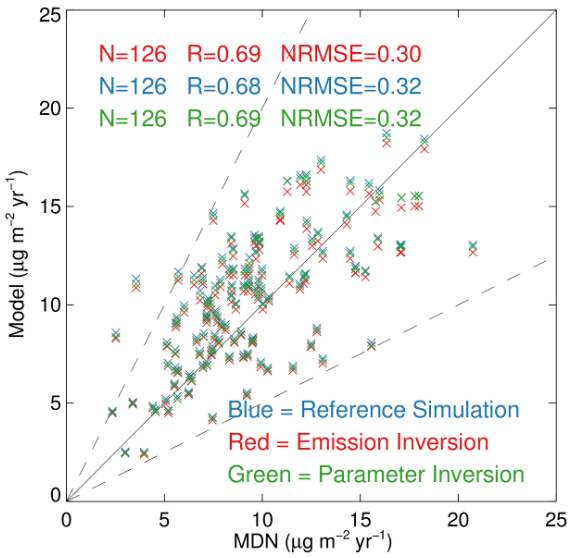

Figure 2.12. Scatter plot comparing model outputs (reference simulation, emission inversion, and parameter inversion) to observations of mercury wet deposition fluxes from the NADP/MDN monitoring network during 2009-2011. The selection criteria of the observational data have been described in Holmes et al. (2010). The solid line indicates the 1:1 ratio and the two dashed lines correspond to the deviation factors of 0.5 and 2.

2.2.2 Emission Inversion: Optimized Emission Fluxes

The annual reference and optimized emissions of mercury are shown in Table 2.3. Equation (2.10) is used to compute the annual uncertainty for seasonal sources (Chen and Prinn, 2006).

$$\bar{\sigma} = \sqrt{n \sum_{i=1}^{n} \sigma_t^{\,2}} \qquad (2.10)$$

where n = 12 months and σ_t is monthly error. The uncertainty of the aseasonal source (annual Asian anthropogenic emission) is obtained directly from Equation (2.7). The global optimized mercury emission is ~ 5.8 Gg yr^{-1}, with an uncertainty range of 1.7-10.3 Gg yr^{-1}. Compared to our reference emission of ~ 6.0 Gg yr^{-1} (uncertainty range: 0.4-12.2 Gg yr^{-1}), the emission inversion results in a slightly smaller value and also reduces its uncertainty range. The optimized value is smaller than previous estimates of 7.5 Gg yr^{-1} by Pirrone et al. (2010) using a bottom-up approach. The emission inversion increases emissions from anthropogenic sources and ocean surfaces, but decreases those from terrestrial surfaces. The ocean accounts for more than half (55%) of the total, while the terrestrial surface contributes only a small fraction (6%).

Ocean Evasion. Net Hg^0 evasion from the global ocean is optimized by the emission inversion as 3160 Mg yr^{-1}, with an uncertainty range of 1160-5160 Mg yr^{-1} (Table 2.3). The NH and SH oceans contribute similar amounts to the total, but on an area basis, evasion from the NH ocean is higher since it is 30% smaller. We are able to reduce ocean evasion uncertainty from 50% to 40% by using top-down constraints. Figure 2.13 shows the monthly reference and optimized emissions of seasonal sources. We find, for both hemispheres, that the emission inversion generally results in increased ocean emissions in summer and decreased emissions in winter, compared to the reference simulation. As a result, we hypothesize that one or more ocean processes that affect the seasonal behavior of aqueous mercury and its evasion are not well-represented in GEOS-Chem. We therefore conduct a series of sensitivity studies of model parameters to test their potential effects on the seasonal pattern of ocean emission. We also compare the parameter values used in GEOS-Chem with their possible ranges in a recent review (Batrakova et al., 2014). The tested model parameters in GEOS-Chem include rates of redox chemical reactions and physical processes in the ML and subsurface mercury concentrations affecting physical exchange between the ML and subsurface waters. Through these sensitivity tests and literature review, we identify two processes as candidates for improvement, the rate constant of dark oxidation of Hg_{aq}^0 (K_{OX2}) and the partition coefficient between Hg_{aq}^{2+} and Hg_{aq}^P (K_D). We optimize these two ocean model parameters in the parameter inversion, as described in Section 2.1.5.

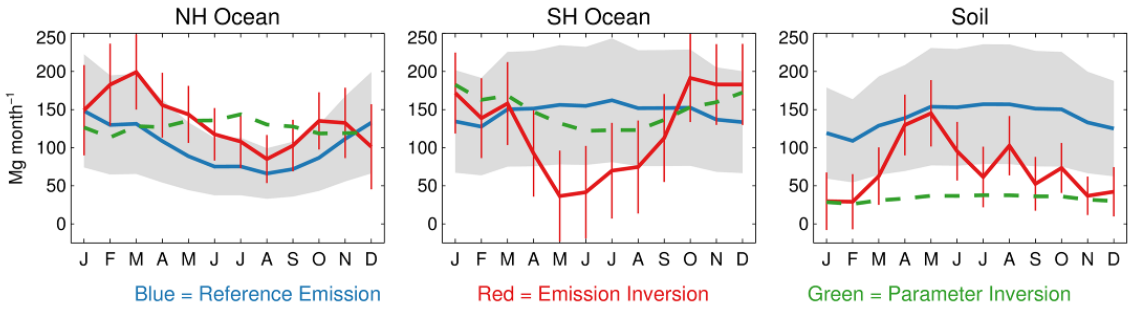

Figure 2.13. Monthly emissions for the three seasonal sources (NH ocean, SH ocean, and soil) from the reference simulation (blue solid lines), emission inversion (red solid lines), and parameter inversion (green dashed lines). The grey shaded regions and red error bars indicate one-sigma uncertainties for the reference emissions and emission inversion, respectively.

Terrestrial Ecosystem. As shown in Table 2.3, the emission inversion reduces soil emissions of Hg^0 by about 50%, from 1680 ± 840 to 860 ± 440 Mg yr^{-1}. Using Equation (2.1), the optimized net emission flux from terrestrial surfaces (E_{net}) is 340 Mg yr^{-1}. If we do not consider geogenic activities (90 Mg yr^{-1}) and biomass burning (210 Mg yr^{-1}), the E_{net2} (calculated as $E_{soil} + E_{pr} - E_{ddHg0}$ and representing net emissions from soils/vegetation) is almost zero after optimization. Thus terrestrial surfaces are neither a net source nor a net sink of Hg^0. This is in contrast to bottom-up estimates that the terrestrial surface is a net source of about 2000 Mg yr^{-1} (Mason, 2009; Pirrone et al., 2010). Vegetation is now believed to serve as a net sink of atmospheric Hg^0 through foliar uptake and sequestration (Stamenkovic and Gustin, 2009; Gustin et al., 2008). Although its size has not been well quantified, we suggest that this sink is important in global mass balance since litterfall transfers about 1200 Mg Hg yr^{-1} to terrestrial surfaces (Wang et al., 2016). Air-soil flux measurements show that Hg^0 emissions from background soils generally dominate over dry deposition (Denkenberger et al., 2012; Edwards and Howard, 2013; Ericksen et al., 2006; Obrist et al., 2014; Park et al., 2013). Our result of a smaller soil Hg source is consistent with a study by Obrist et al. (2014), which suggested that Hg was unlikely to be re-emitted once incorporated into soils and that terrestrial Hg emission was restricted to surface layers (Demers et al., 2013). Our result is also in agreement with estimates of terrestrial fluxes of southern Africa using Hg^0 correlations with ^{222}Rn, a radioactive gas of predominantly terrestrial origin (Slemr et al., 2013). Considering that soil is a smaller source while vegetation a sink of Hg^0, our result that the terrestrial ecosystem is neither a net source nor a net sink of Hg^0 is reasonable, implying that the magnitudes of soil emission and dry deposition of Hg^0 (primarily to vegetation) are similar.

We evaluate dry deposition fluxes modeled by GEOS-Chem against data in Zhang et al. (2012a), which estimated fluxes at sites in North America and obtained reasonable agreements with surrogate surface and litterfall measurements (Graydon et al., 2008; Lyman et al., 2007). As shown in Figure 2.14, there is no obvious bias in the average dry deposition flux at eight background sites, indicating that ~ 1400 Mg yr^{-1} (modeled by GEOS-Chem) may be reasonable estimates for both emission and dry deposition of Hg^0.

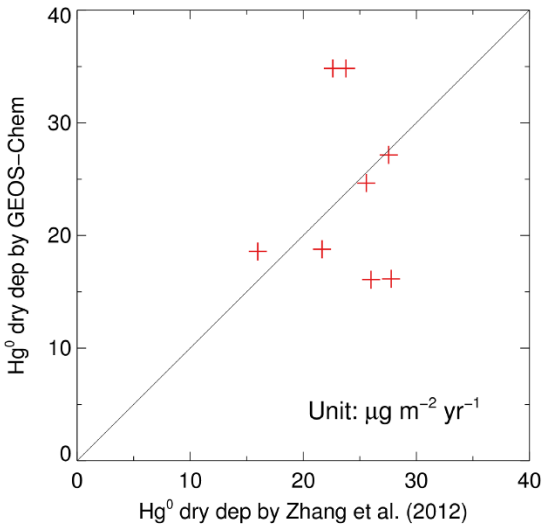

Figure 2.14. Scatter plot of annual Hg^0 dry deposition fluxes modeled by GEOS-Chem (reference simulation) and determined by Zhang et al. (2012a). The solid line indicates 1:1 line. The annual Hg^0 dry deposition fluxes from GEOS-Chem and Zhang et al. (2012a) are both 24 μg m^{-2} yr^{-1}.

Anthropogenic Emission from Asia. Table 2.5 summarizes Asian emissions of Hg^0 (only GEM) estimated by several recent bottom-up emission inventories and modeling studies. These inventories reported Asian anthropogenic emissions ranging from 550-800 Mg yr^{-1}. In our model simulations, the reference emission of 770 Mg yr^{-1} follows AMAP/UNEP (2013). The emission inversion using all 27 sites increases this value to 1060 ± 110 Mg yr^{-1}. Uncertainty in Asian anthropogenic emission should be larger than that obtained using our inversion method, because emission estimates are sensitive to the Asia-Pacific sites used in the inversion. As discussed above, model performance at several Asia-Pacific sites is affected by unknown intercomparison errors and local emission and meteorological factors not captured by GEOS-Chem. To obtain a more accurate estimate of uncertainty, we perform seven emission inversions, each including only one Asia-Pacific site.

As shown in Table 2.5, these inversions result in Asian anthropogenic emissions of Hg^0 ranging from 650-1770 Mg yr^{-1}. Comparing this range to its bottom-up inventory estimates of 550-800 Mg yr^{-1}, we suggest that the Asian anthropogenic emission is very likely to be underestimated in these bottom-up inventories. We estimate total (anthropogenic + natural + legacy) Hg^0 emission in Asia as 1180-2030 Mg yr^{-1}. Our uncertainty ranges cover those in

Strode et al. (2008), which estimated total Asian emission of 1260-1450 Mg yr^{-1} with 890-990 Mg yr^{-1} from anthropogenic sources, by comparing GEOS-Chem to the observed Hg:CO ratio at sites OKN and MBO. Pan et al. (2007) assimilated aircraft observations into a regional CTM and estimated total Hg^0 emission in East Asia as 2270 Mg yr^{-1}, at the upper end of our range. Jaffe et al. (2005) and Fu et al. (2015) obtained total Hg^0 emissions in Asia of 1460 and 1590-1870 Mg yr^{-1}, respectively, compared well with our range, using the Hg^0:CO and/or Hg^0:CO_2 slopes observed at ground-based sites and inventories of CO and CO_2. Shetty et al. (2008) estimated natural terrestrial emission in East Asia was about 710 Mg yr^{-1}, much higher than our 0-230 Mg yr^{-1} in a larger domain. The difference is due to their larger estimation of vegetation evapotranspiration (630 Mg yr^{-1}).

There is some new evidence supporting our conclusion that the Asian anthropogenic emission of mercury is very likely to be underestimated in AMAP/UNEP (2013). First, several potentially important sectors and activities are not included in AMAP/UNEP (2013), which is mainly because of lack of information at a global scale. For example, only in China, the disposal of nonferrous metal (zinc, lead and copper) smelting slags is estimated to emit 47.8 (uncertainty range: 3.4-102.7) Mg yr^{-1} Hg into the atmosphere (Wu et al., 2016), and the reuse of fly ash (a byproduct of coal fired power plants) contributes 32.7 (uncertainty range: 12.5-56.1) Mg yr^{-1} Hg (Hui et al., 2015). Second, new data from National Bureau of Statistics of China (NBSC, 2015) suggested that China's coal consumption used in the calculation of AMAP/UNEP (2013) had been underestimated by ~ 10% in 2010. As the use of coal in power plants and industry is an important factor for Hg emission in China, it implies an underestimation in atmospheric mercury emissions. Third, a recent study (Wang et al., 2015) used satellite measurements to constrain SO_2 emissions from individual power plants and indicated that the real efficiencies of flue gas desulfurization facilities operated in these power plants were considerably lower than reported due to weak supervision measures in China. As Hg-specific control devices have not been installed in China's coal fired power plants, the removal of mercury primarily relies on the co-benefits of air pollution control devices aimed to control other air pollutants (e.g. particulate matter, SO_2, and NO_x). Therefore, an overestimation of air pollution control efficiency also implies that more Hg is released into the atmosphere than previously thought.

Table 2.5. Comparison of Asian Hg^0 emissions from recent studies. Unit is Mg yr^{-1}.[a]

Reference	Base year	Anthropogenic	Net terrestrial[b]	Net ocean[b]	Total
Emission inventories					
Streets et al. (2009)[c]	2006	800			
Streets et al. (2011)[c]	2008	700			
Muntean et al. (2014)	2008	580			
AMAP/UNEP (2013)	2010	770			
Rafaj et al. (2013)[c]	2010	550-750			
Other studies					
Jaffe et al. (2005)	2004				1460
Pan et al. (2007)[d]	1999			420	2270
Shetty et al. (2008)[d]	2001		710	120	
Strode et al. (2008)	2004	890-990			1260-1450
Fu et al. (2015)[e]	2007-2010				1590-1870
This study					
Reference emission	2009-2011	770 ± 390	360	230	1360
Emission inversion	2009-2011	1060 ± 110	130	300	1490
Inversion using different Asian sites	2009-2011	650-1770	0-230	260-300	1180-2030

[a] Here Hg^0 only refers to gaseous elemental mercury.

[b] Net terrestrial and ocean emissions are from the Asian domain.

[c] Estimated values from tables and figures in the references.

[d] An East Asian domain is used in these studies. Their terrestrial and ocean surfaces are smaller than those of the Asia domain.

[e] The Asian domain includes mainland China, South Asia, Indochinese Peninsula, and Central Asia, and does not include ocean surfaces.

2.3 Parameter Inversion: Results

2.3.1 *A Posteriori* Parameters

Results of the parameter inversion are presented in Table 2.6. The *a posteriori* K_{OX2} of 6×10^{-6} s^{-1} is much larger than its current value (1×10^{-7} s^{-1}) in GEOS-Chem, suggesting that Hg_{aq}^0 dark oxidation in the ML is more important than previously thought. The *a posteriori* log K_D of 4.2 is lower than seawater values in the literature (Batrakova et al., 2014; Fitzgerald et al.,

2007) but agrees with the lower end of fresh water measurements (Amos et al., 2014). We attribute this discrepancy to several simplifying assumptions in GEOS-Chem. K_D is linked to the estimates of SPM concentrations in the ML and organic carbon export. As described above, the amount of organic carbon export is very uncertain (5-20 Gt C yr^{-1}). A smaller organic carbon export may correspond to a larger log K_D. The uncertain spatial and seasonal variations of carbon export may also affect the estimate of log K_D. In addition, there are no available global data sets of SPM in the ML. GEOS-Chem derives SPM concentrations from MODIS satellite Chlorophyll a and C:Chla ratios (Soerensen et al., 2010b). Thus, the uncertain SPM fields may also affect log K_D. As for the other two parameters (ER_{Soil} and ER_{Asia}), the parameter inversion decreases soil emission but increases Asian anthropogenic emission, consistent with the emission inversion.

Table 2.6. Evolution of the estimates of the four parameters in the parameter inversion.

Parameter	*A priori*	First iteration	Before second iteration*	*A posteriori*
-log K_{OX2}	5.0 ± 1.0	5.1 ± 0.1	5.1 ± 1.0	5.2 ± 0.1 ($K_{OX2} = 6\times10^{-6}$ s^{-1})
log K_D	5.3 ± 0.4	4.4 ± 0.2	4.4 ± 0.2	4.2 ± 0.2 ($K_D = 1.6\times10^4$ L kg^{-1})
ER_{Soil}	1.0 ± 0.5	0.37 ± 0.08	0.37 ± 0.19	0.24 ± 0.1 (Soil emission decreases by 76%)
ER_{Asia}	1.0 ± 0.5	1.7 ± 0.1	1.7 ± 0.9	1.9 ± 0.1 (Asian anthropogenic emission increases by 90%)

*For the 2nd iteration, we use the best estimates derived from the 1st iteration, but larger parameter uncertainties. The uncertainty of 1.0 for -log K_{OX2} is the same as that for the *a priori* estimate. The uncertainties for ER_{Soil} and ER_{Asia} are chosen as 50% of their best estimates, in consistent with the emission inversion. The uncertainty for log K_D is chosen as 0.2 because it is approaching the lower end (4.2) of the possible values in the literature survey.

Table 2.7. Recent surface ocean mercury measurements and corresponding simulated concentrations.

Location	Date	Latitude, longitude	Measurement	Reference simulation[a]	Parameter inversion[a]	Ref.[b]
			Hg_{aq}^{T} (pM)			
Atlantic Ocean	Nov 2008	15N-50N, 20W-5W	0.8-3.0	*0.64±0.18*	0.89±0.15	(1)
		30S-15S, 0-15E	0.4-2.8	0.48±0.23	0.97±0.22	(1)
	Apr-May 2009	15N-50N, 25W-5W	0.4-2.3	*0.34±0.08*	0.82±0.10	(1)
		50S-15S, 65W-20W	0.5-1.5	0.68±0.21	0.89±0.12	(1)
	Oct-Nov 2005	20S-35N, 25W-10E	0.5-4.5	0.63±0.25	1.2±0.58	(2)
	Jun 2008	32N, 64W	0.6-1.0	0.65±0.32	*1.2±0.6*	(3)
	Sep 2008-2009	25N-35N, 65W-60W	0.6-0.9	*0.95±0.05*	*1.2±0.1*	(4)
	Aug 2010	30N-32N, 65W-60W	1.2-1.6	*0.91±0.04*	1.2±0.1	(4)
Pacific Ocean	Mar 2006	20N-50N, 152W	0.5-1.9	0.96±0.10	1.2±0.2	(5)
	May 2009	30N, 140W	0.2-0.4	*0.8±0.4*	*1.1±0.6*	(6)
	Oct 2011	15S-17N, 175W-155W	< 0.5	*0.83±0.27*	*1.1±0.5*	(7)
Southern Ocean	Mar-Apr 2008	66S-44S, 140E-147E	0.6-2.8	0.85±0.29	1.1±0.3	(8)
			Hg_{aq}^{0} (fM)			
Atlantic Ocean	Nov 2008	15N-50N, 20W-5W	30-140	52±14	51±7	(1)
		30S-15S, 0-15E	15-30	*38±16*	*68±16*	(1)
	Apr-May 2009	15N-50N, 25W-5W	15-40	27±6	*55±6*	(1)
		50S-15S, 65W-20W	10-70	54±16	59±12	(1)
	Jul 2005	60N, 40W-5E	30-90	*22±10*	83±12	(9)
	Sep 2008-2009	25N-35N, 65W-60W	80-170	80±4	87±5	(4)
	Jun 2009	32N, 64W	105-135	*55±27*	*90±45*	(4)
	Aug 2010	30N-32N, 65W-60W	130-260	*77±4*	*94±2*	(4)
Pacific Ocean	Oct 2011	15S-17N, 175W-155W	< 100	71±24	81±36	(7)
Southern Ocean	Mar-Apr 2008	66S-44S, 140E-147E	< 280	72±24	58±19	(8)
			Hg_{aq}^{P} (fM)			
Pacific Ocean	Oct 2011	15S-17N, 175W-155W	20-50	*70±33*	*5±3*	(7)

1 pM = 10^{-9} mol m^{-3}; 1 fM = 10^{-12} mol m^{-3}.

[a] Numbers in italics represent the modeled concentrations are out of the corresponding measurement ranges.

[b] References: (1) Kuss et al. (2011); (2) Pohl et al. (2011); (3) Lamborg et al. (2012); (4) Soerensen et al. (2013); (5) Sunderland et al. (2009); (6) Hammerschmidt and Bowman (2012); (7) Munson et al. (2015); (8) Cossa et al. (2011); (9) Andersson et al. (2011).

Similar to our model-observation comparison for the emission inversion, we run GEOS-Chem using optimized parameters and calculate the NRMSEs for all ground-based sites (Table 2.4). A smaller average NRMSE of 0.14 for the parameter inversion than that of 0.16 for the reference simulation shows improvement in model performance. GEOS-Chem simulations using optimized parameters also match regional over-water Hg^0 (NRMSE = 0.10) and wet deposition measurements (Figure 2.12). In addition, we evaluate the optimized model against recent surface ocean measurements of total aqueous mercury (Hg_{aq}^T), Hg_{aq}^0, and Hg_{aq}^P (Table 2.7). For Hg_{aq}^T, 50% and 75% (6 and 8 out of 12) modeled data from the reference and optimized simulations, respectively, are within measurement ranges. For Hg_{aq}^0, 60% (6 out of 10) modeled data from both simulations are within measurement ranges. For Hg_{aq}^P, the reference simulation predicts a higher while the parameter inversion predicts a lower value than the only measurement data. These results suggest that the parameter inversion is comparable or potentially better than the reference simulation with regard to modeling surface ocean mercury.

2.3.2 Global Ocean Hg Budget

Optimizing the two ocean model parameters, -log K_{OX2} and log K_D, changes the global ocean Hg budget in GEOS-Chem, as shown in Figure 2.15. Sources of Hg_{aq} in the ML include deposition of oxidized Hg and physical transport from subsurface waters. They are balanced by Hg^0 evasion and Hg_{aq}^P sinking. In the reference simulation, although deposition (20.2 Mmol yr^{-1}) accounts for most ML Hg_{aq} inputs, the two physical transport processes, entrainment/detrainment of the ML and Ekman pumping, together supply a considerable amount (F_{INT}: 6.1 Mmol yr^{-1}) from subsurface waters. This upward flux is a result of the gradient in Hg_{aq}^T between the ML (0.8 pM) and subsurface waters (1.1 pM). Hg^0 evasion and Hg_{aq}^P sinking remove 14.9 and 11.4 Mmol yr^{-1} from the ML, respectively. The combined effect of the larger K_{OX2} and smaller K_D in the parameter inversion is, in the ML, that Hg_{aq}^{2+} increases from 0.69 to 0.95 pM, Hg_{aq}^P decreases from 0.05 to 0.004 pM, and Hg_{aq}^0 remains to be 0.06 pM. Hg_{aq}^P sinking becomes a smaller sink (1.7 Mmol yr^{-1}) due to the lower K_D. Physical transport contributes a downward flux (-1.5 Mmol yr^{-1}) since the gradient of Hg_{aq}^T between the ML (1.0 pM) and subsurface waters (1.1 pM) is diminished.

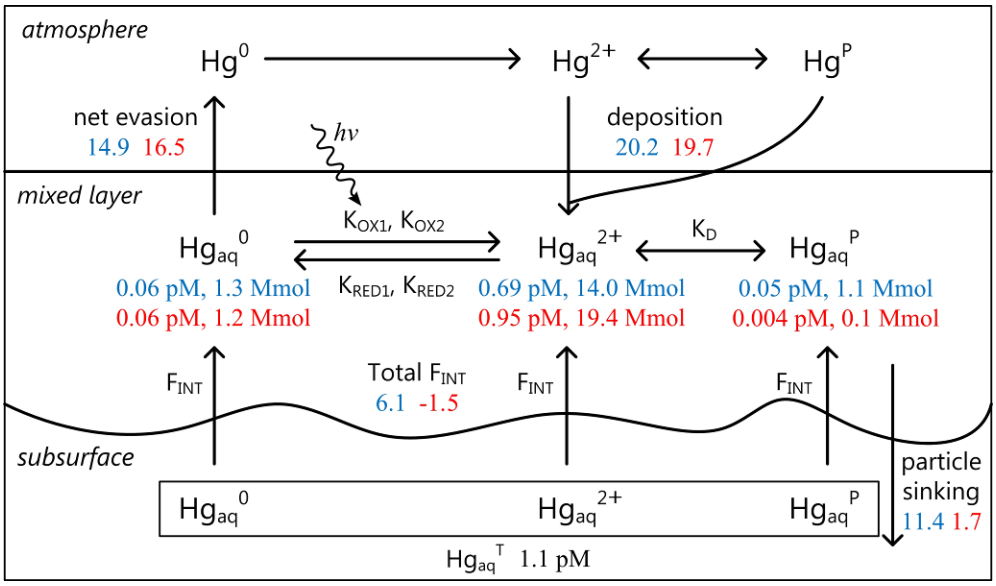

Figure 2.15. Global ocean mercury budget modeled by GEOS-Chem. Blue color indicates the reference simulation and red color the parameter inversion. Fluxes are in Mmol yr^{-1}. Notations in this figure follow Soerensen et al. (2010b). F_{INT} denotes net fluxes from subsurface waters through entrainment/detrainment of the mixed layer and Ekman pumping.

Physical transport and Hg_{aq}^{P} sinking affect seasonal variations of simulated Hg^0 evasion from the ocean (Soerensen et al., 2010b). In summer, enhanced biological productivity increases Hg_{aq}^{P} sinking and decreases Hg^0 evasion by shifting speciated Hg_{aq} equilibrium in the ML towards Hg_{aq}^{0} loss. During winter months, the ML deepens and Hg_{aq} in subsurface waters invade the ML by entrainment, and Hg^0 evasion will be enhanced if subsurface waters contain higher Hg_{aq}^{T}. In the parameter inversion, physical transport and Hg_{aq}^{P} sinking are both weakened, as described above. As a result, the parameter inversion overturns seasonality of simulated ocean evasions in both hemispheres (see Figure 2.13), agreeing with results from the emission inversion.

As described in Section 2.1.6, we conduct an additional parameter inversion including six new elements representing Br columns in different latitudinal bands. As shown Figure 2.16, -log K_{OX2} is found to be strongly correlated with Br columns in 30°N-60°N, 30°S-0°, and 60°S-30°S. The other three factors, log K_D, ER_{Soil}, and ER_{Asia}, have no or weak correlations with Br columns. Thus, we suggest that the inversion results of smaller terrestrial emissions and larger Asian anthropogenic emissions are not likely to be affected by the uncertainty in

atmospheric chemistry, but the poor understanding of atmospheric chemistry may limit our ability to further constrain specific ocean model parameters.

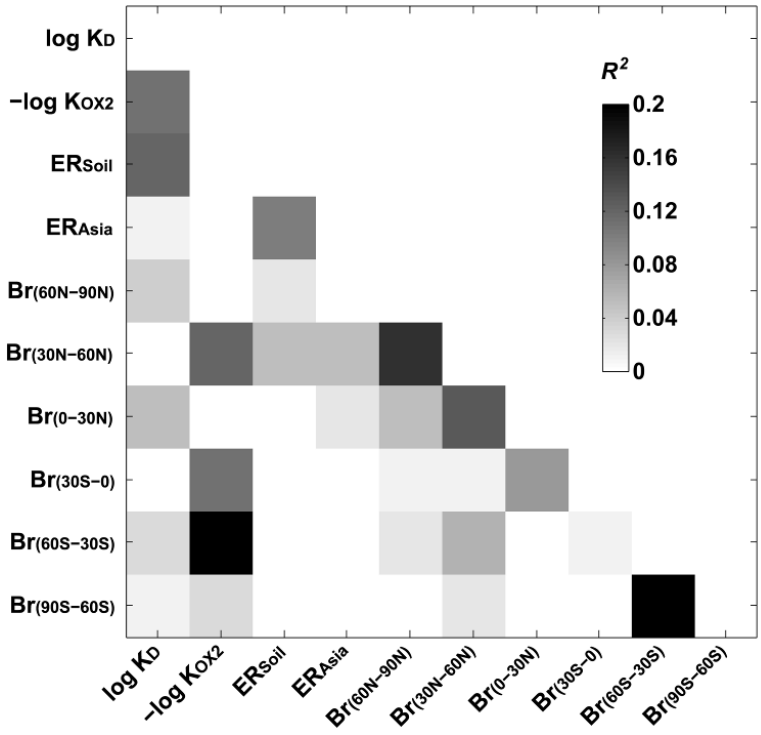

Figure 2.16. Average correlations (R^2) between the optimized parameters derived from the special case of parameter inversion. Diagonal elements (identically equal to 1) are set to 0 for clarity. Each of the 6 bromine elements represents Br columns in a 30° latitudinal band, e.g., "$Br_{(60N-90N)}$" is the Br column from 60N to 90N. In this parameter inversion, we assume that each Br column has a one-sigma uncertainty of 50% and that its best estimate is the current value in GEOS-Chem.

2.4 Implications for the Hg Biogeochemical Cycle

We use a seven-box model in order to explore the long-term impact of our inverted emissions and parameters on the global biogeochemical cycling of mercury (Amos et al., 2013). This seven-box model dynamically couples the atmosphere, three terrestrial reservoirs (fast, slow, and armored), and three ocean reservoirs (surface, subsurface, and deep). All rate coefficients of Hg mass between reservoirs are assumed to be first-order. The simulation is

initialized with geogenic emissions to represent natural mercury cycle, and after reaching steady state, is driven by historical anthropogenic emissions (Horowitz et al., 2014; Streets et al., 2011).

Two long-term box-model simulations are performed. The first uses rate coefficients from the present-day global budget in the reference simulation. The second uses those from our emission and parameter inversions, and has higher anthropogenic emissions, lower reemission from terrestrial surfaces, and less sinking out of surface ocean than the first one does (Table 2.8). The second simulation obtains larger terrestrial mercury reservoirs, highlighting their important role in sequestering legacy mercury. The oceans are a smaller mercury reservoir of ~ 1700 Mmol in the second simulation, compared to that of ~ 2000 Mmol in the first simulation. The former number is more consistent with the estimates of about 1300-1400 Mmol by Lamborg et al. (2014). The first box-model simulation shows that 18% of present-day atmospheric deposition is from primary anthropogenic emissions, 76% is legacy, and 6% is natural (i.e. geogenic emissions). Applying our inversion results into the box model, the second simulation suggests that primary anthropogenic emissions account for a larger fraction (18-23%) of present-day atmospheric deposition. Legacy releases of mercury contribute a smaller proportion (72-76%) but still play a major role.

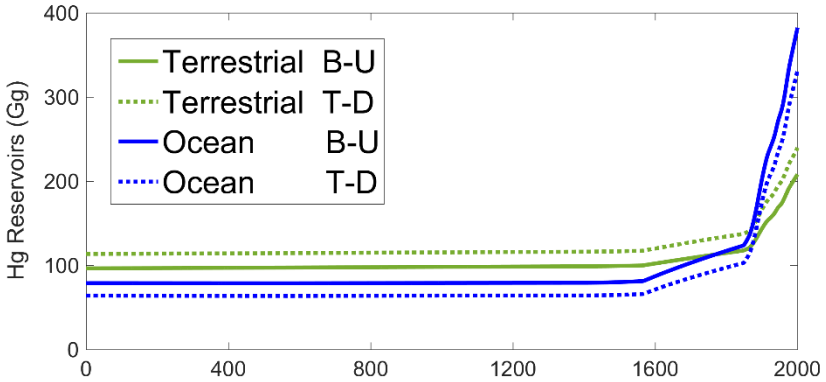

Figure 2.17. Simulated ocean and terrestrial reservoirs of mercury using the 7-box model.

Table 2.8. Present-day reservoirs and fluxes used to calculate first-order rate coefficients in the 7-box model of Hg global cycle. "Default" values are from Amos et al. (2014). The first and second simulations represent the averages of the reference and optimized simulations, respectively. All fluxes are in Mg yr^{-1}.

	Default	First simulation[a]	Second simulation[a]
Atmosphere	5000 Mg	*4700 Mg*	*4400 Mg*
Hg^{II} deposition to land	1500	*1670*	*1620*
Hg^{0} deposition to land	1500	*1430*	*1320*
Hg^{II} deposition to ocean	3600	*4000*	*4000*
Hg^{0} air-sea exchange, gross loss to the ocean	1700	*1600*	*1500*
Surface ocean	2900	*3280 Mg*	*4100 Mg*
Hg^{0} air-sea exchange, gross evasion to atmosphere	4700	*4600*	*4800*
Particle settling to the subsurface ocean	3300	*2280*	*340*
Water transfer to subsurface ocean	5100	*5800*	*7300*
Subsurface ocean	130,000 Mg	*123,000 Mg*	*123,000 Mg*
Particle settling to the deep ocean	480	*460*	*460*
Water transfer to surface ocean	7100	*7000*	*7000*
Water transfer to deep ocean	340	*320*	*320*
Deep ocean	220,000 Mg	—	—
Burial to deep sediments	210	—	—
Water transfer to subsurface ocean	180	—	—
Fast terrestrial reservoir	9600 Mg	—	—
Evasion due to respiration of organic carbon[b]	45	*690*	*360*
Photochemical re-emission of deposited Hg	85	*1270*	*680*
Biomass Burning	290	*200*	*200*
Transfer to the slow pool	330	—	—
Transfer to the armored pool	10	—	—
Riverine discharge to ocean margins	710	—	—
Slow soil reservoir	35,000 Mg	—	—
Evasion due to respiration of organic carbon[b]	25	*370*	*200*
Biomass burning	8	*6*	*6*
Transfer to fast pool	210	—	—
Riverine discharge to ocean margins	20	—	—
Armored soil reservoir	190,000 Mg	—	—
Evasion due to respiration of organic carbon[b]	3	*37*	*20*
Biomass burning	4	*3*	*3*
Transfer to fast pool	15	—	—
Riverine discharge to ocean margins	10	—	—
External inputs		—	—
Geogenic emissions	90	—	—
Anthropogenic emissions	*f(t)*[c]	—	—
Anthropogenic discharges to rivers	*f(t)*[c]	—	—

[a]Italic values show changes of the first and second simulations.

[b]In our simulation cases, the evasions from the soil reservoirs are larger than the default values in Amos et al. (2014).

[c]A function of time as shown in Amos et al. (2014).

2.5 Summary and Conclusion

Here, we perform global-scale inverse modeling combining ground-based Hg^0 observations and GEOS-Chem mercury simulations. Using Bayesian inversion methods, we are able to constrain present-day mercury emission fluxes from major sources (emission inversion) and relevant key parameters in GEOS-Chem (parameter inversion), and reduce uncertainties associated with these fluxes and parameters.

The emission inversion better reproduces ground-based Hg^0 observations (particularly for sites in the Southern Hemisphere and North America) than the reference simulation, and also matches measured Hg^0 over the North Atlantic Ocean and wet deposition fluxes in North America. We obtain a global Hg emission of 5.8 Gg yr^{-1} (uncertainty range: 1.7-10.3 Gg yr^{-1}), smaller than the estimate of 7.5 Gg yr^{-1} using a bottom-up approach (Pirrone et al., 2010). The global ocean accounts for 3.2 Gg yr^{-1} Hg (55% of the total). The terrestrial ecosystem is neither a net source nor a net sink of atmospheric Hg^0, in contrast to its bottom-up estimate as a significant source (Mason, 2009; Pirrone et al., 2010). The optimized Asian anthropogenic emissions range from 650-1770 Mg yr^{-1}, suggesting that bottom-up inventories (550-800 Mg yr^{-1}) may have substantially underestimated their value. The total Asian Hg^0 emission (including anthropogenic, natural and legacy sources) is estimated as 1180-2030 Mg yr^{-1}, consistent with recent studies (Fu et al., 2015; Strode et al., 2008; Pan et al., 2007).

The emission inversion changes seasonal patterns of ocean emissions in both hemispheres. We identify and constrain two ocean model parameters in GEOS-Chem that can explain this seasonal pattern, the rate constant of dark oxidation of Hg_{aq}^0 (K_{OX2}) and the partition coefficient between Hg_{aq}^{2+} and Hg_{aq}^P (K_D). The *a posteriori* K_{OX2} (6×10^{-6} s^{-1}) is larger than its current value in GEOS-Chem (1×10^{-7} s^{-1}), suggesting that dark oxidation of Hg_{aq}^0 is more important than previously thought. The *a posteriori* log K_D (4.2) is smaller than its *a priori* (5.3), leading to less Hg_{aq}^P sinking out of the mixed layer. These changes in parameters affect the simulated global ocean mercury budget, especially mass exchange between the mixed layer and subsurface waters. The parameter inversion changes seasonality of ocean emissions in both hemispheres, agreeing with results from the emission inversion.

Our inversion results suggest changes in our understanding of the timescales of cycling between different mercury reservoirs. Based on these changes, the long-term biogeochemical box-model simulations result in larger estimated terrestrial mercury pools and smaller ocean mercury pools. Legacy mercury accounts for a smaller fraction to present-day atmospheric deposition than previous estimates, whereas the contribution of primary anthropogenic emissions becomes larger (up to 23%).

Our inversion results identify specific knowledge gaps in mercury observation and modeling that currently limit our ability to constrain the biogeochemical cycle of mercury. First, and most important, effective inversions are hampered by the uncertain atmospheric Hg measurements. Only a few experiments have been made to evaluate the comparability of mercury measurements (Gustin et al., 2013). Research aimed at quantifying and reducing measurement uncertainties should be given high priority by the Hg measurement community. Second, observational sites are sparse in some regions (e.g. the Southern Hemisphere). More sites in these regions are necessary to further constrain emissions. Third, uncertainty in atmospheric Hg chemistry also affects our inversion results (specifically, in constraining ocean model parameters). Improving our understanding of atmospheric mercury chemistry at both global and regional scales (e.g. the Polar Regions) requires a combination of both measurement and modeling advances.

Chapter 3 Constraining the Atmosphere–Surface Exchange of Hg^0 over Eastern North America

In this chapter, we use the GEOS-Chem chemical transport model to interpret atmospheric Hg^0 data collected in the 2013 summer Nitrogen, Oxidants, Mercury and Aerosol Distributions, Sources and Sinks (NOMADSS) aircraft campaign and ground- and ship-based observations in terms of their constraints on the atmosphere–surface exchange of Hg^0 over eastern North America. Model–observation comparison suggests that the Northwest Atlantic may be a net source of Hg^0, with high evasion fluxes in summer (our best sensitivity simulation shows an average oceanic Hg^0 flux of 3.3 ng m^{-2} h^{-1} over the Northwest Atlantic), while the terrestrial ecosystem in the eastern United States is likely a net sink of Hg^0 during summer (our best sensitivity simulation shows an average terrestrial Hg^0 flux of -0.6 ng m^{-2} h^{-1} over the eastern United States). The inferred high Hg^0 fluxes from the Northwest Atlantic may result from high wet deposition fluxes of oxidized Hg, which are in turn related to high precipitation rates in this region. We also find that increasing simulated terrestrial fluxes of Hg^0 in spring compared to other seasons can better reproduce observed seasonal variability of Hg^0 concentration at ground-based sites in eastern North America.

3.1 Methodology

In this section, we first present the aircraft-, ground-, and ship-based observations. The GEOS-Chem mercury model simulations we perform are then introduced.

3.1.1 Observations

The NOMADSS campaign was conducted onboard the National Science Foundation (NSF)/National Center for Atmospheric Research (NCAR) C-130 aircraft from June 1 to July 15, 2013, during which 19 research flights were made out of Smyrna, Tennessee (Figure 3.1). NOMADSS was part of the Southeast Atmosphere Study (SAS), a field campaign that focused

on southeastern U.S. regional air quality and climate (Carlton et al., 2016). Mercury concentrations were measured using the onboard University of Washington's Detector for Oxidized Hg Species (DOHGS). Its design, configuration, and calibration have been described in detail in Lyman and Jaffe (2012) and Ambrose et al. (2015). Briefly, DOHGS is used to simultaneously and continuously measure total Hg ($Hg^T = Hg^0 + Hg^{II}$) and Hg^0 concentrations using two parallel channels, with Hg^{II} determined by their difference. The two channels sample ambient air at 1 standard liter per minute from a heated (110 °C) Teflon sample line connected to a rear-facing aircraft inlet. In the Hg^T channel, air passes through a heated (650 °C) quartz pyrolyzer to reduce all Hg^{II} species to Hg^0. In the Hg^0 channel, a trapping sorbent, either quartz wool or cation exchange membrane, is used to selectively remove Hg^{II} from the air. Both channels employ Tekran® 2537B analyzers to detect Hg^0 at a resolution of 2.5 minutes, using cold vapor atomic fluorescence spectrometry after pre-concentration on two alternating gold traps and subsequent thermal desorption. A customized Hg^0 permeation source was applied to perform the pre-, in-, and post-flight calibrations during NOMADSS. Mercury concentrations were reported in nanograms per cubic meter (ng m^{-3}) at standard temperature and pressure. The overall measurement uncertainty was calculated as the quadratic sum of the 1σ precision and calibration uncertainties, varying from 6–10% for Hg^0 among different research flights. The NOMADSS speciated Hg observations have been used to assess oxidation of Hg^0 by bromine in the subtropical Pacific free troposphere (Shah et al., 2016; Gratz et al., 2015), to quantify mercury enhancement ratios for coal-fired power plants (Ambrose et al., 2015), and to evaluate the Hg outflow from the Chicago/Gary urban/industrial area (Gratz et al., 2016).

Other NOMADSS measurements used here to help interpret mercury observations include isoprene, dimethyl sulfide (DMS), propane, SO_2, NO_x, and meteorological and state variables. Isoprene is known as a tracer for terrestrial forest emissions and DMS is a marker for marine emissions. Isoprene was measured using the Proton Transfer Reaction Mass Spectrometer (Yuan et al., 2015). Propane and DMS were measured by the Trace Organic Gas Analyzer, an online Gas Chromatograph Mass Spectrometer (Apel et al., 2010). A Thermo Scientific model 43i-TLE monitor was used to measure SO_2. NO_x data were from an *in situ* chemiluminescence instrument (Ridley and Grahek, 1990). We average all these measurements to a 2.5-minute resolution to be consistent with the DOHGS Hg data.

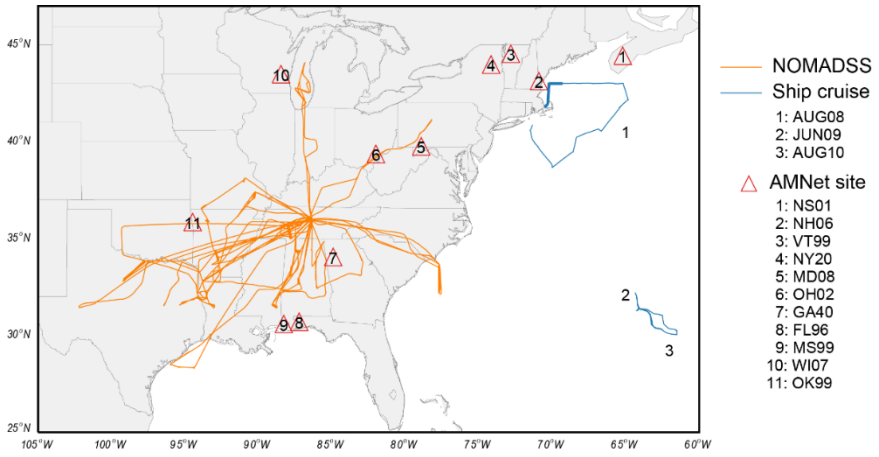

Figure 3.1. Aircraft-, ground-, and ship-based observations used in this study. The orange lines are research flight tracks of the NOMADSS aircraft campaign (out of Smyrna, Tennessee, United States). The red triangles and numbers in them show the locations and names of the 11 rural/remote NADP AMNet sites. The three ship cruise routes in the Northwest Atlantic are shown in blue lines. The thick blue line for the ship cruise during August 2008 (denoted as AUG08) represents the route in the coastal Gulf of Maine where mercury observations are influenced by anomalously high freshwater input.

As shown in Figure 3.1, Hg^0 concentration observations at 11 ground-based rural/remote sites in the eastern United States are drawn from the National Atmospheric Deposition Program's Atmospheric Mercury Network (NADP AMNet). Gay et al. (2013) summarized site characteristics, as well as instrumentation, standard operating procedures, and quality assurance in the NADP AMNet network. Briefly, Tekran® analyzers are used at these sites with sampling intervals of 5–30 minutes. The original high-frequency observational data from 2009 to 2013 are converted into hourly averages and then into monthly averages. We require at least 30 minutes of data to derive an hourly average and at least 10 days of data to derive a monthly average. We use mercury observations from three summertime ship cruises (denoted AUG08, JUN09, and AUG10 for the August 2008, June 2009, and August 2010 cruises, respectively) in the Northwest Atlantic Ocean, to facilitate the analysis of net oceanic Hg^0 flux (Figure 3.1). Concentrations of air Hg^0, aqueous Hg^0 ($Hg_{aq}{}^0$), and total aqueous Hg ($Hg_{aq}{}^T$) along the ship cruise routes are drawn from Soerensen et al. (2013), which also described in detail the methods of atmospheric measurement and seawater collection and analysis. In addition, we also compare the model outputs with the wet deposition flux of Hg^{II} in the eastern United States measured by the NADP Mercury Deposition Network (MDN) (Prestbo and Gay, 2009).

3.1.2 GEOS-Chem Global and Nested Grid Simulations

The global GEOS-Chem CTM (version 9-02) has been described in Section 2.1.2, and here we focus on the nested grid simulation and the parameterizations of the atmosphere–surface exchange. The model uses the GEOS-5 Forward Processing (FP) and GEOS-5.2.0 data for the simulation year of 2013 and the spin-up period of 2010–2012, respectively, due to their different periods covered. The one-way nested grid simulation uses the native GEOS-5 FP horizontal resolution of 0.25° × 0.3125° in North America (130–60° W, 10–60° N). The global simulation with a coarser resolution of 2° × 2.5° (degraded from the native grid) generates initial and boundary conditions for the nested grid simulation. The nested grid simulation of mercury was developed by Zhang et al. (2012b) based on GEOS-5.2.0 (with a native 0.5° × 0.667° resolution in North America), and is updated to the GEOS-5 FP fields. Model results are sampled along flight and ship cruise routes. A non-local planetary boundary layer mixing scheme is used (Lin and McElroy, 2010).

The surface fluxes of Hg^0 at the Earth's surface include anthropogenic sources, biomass burning, geogenic activities, as well as the bi-directional fluxes involved in the atmosphere–terrestrial and atmosphere–ocean exchange. Note that anthropogenic sources also emit a small fraction of Hg^{II}. In our model, the sink of atmospheric Hg^0 is the oxidation by bromine radicals. For all the simulations, biomass burning emissions (382 Mg yr^{-1}) are estimated using a global CO emission database (van der Werf et al., 2010) and a volume ratio of Hg/CO of 2×10^{-7} (Slemr et al., 2014). Geogenic activities (90 Mg yr^{-1}) are spatially distributed based on the locations of mercury mines. GEOS-Chem estimates the bi-directional exchange of Hg^0 between the atmosphere and the terrestrial and oceanic surfaces in different ways. For atmosphere–terrestrial exchange, GEOS-Chem treats the evasion and dry deposition of Hg^0 separately. Dry deposition is parameterized with a resistance-in-series scheme (Wesely, 1989). Hg^0 evasion includes volatilization from soil and rapid recycling of newly deposited Hg. The former is estimated as a function of soil Hg content and solar radiation. The latter is modeled by recycling a fraction of wet/dry deposited Hg^{II} to the atmosphere as Hg^0 immediately after deposition (60% for snow covered land and 20% for all other land uses) (Selin et al., 2008). The net terrestrial flux is calculated as the sum of the three individual processes. GEOS-Chem estimates the atmosphere–ocean exchange of Hg^0 using a standard two-layer diffusion model:

$$F = K\,(Hg_{aq}^{0} - Hg_{air}^{0} / H) \quad (3.1)$$

where F is the net emission flux, K is the mass transfer coefficient estimated by wind speed and temperature-corrected Schmidt numbers for CO_2 and Hg^0 (Nightingale et al., 2000), and H is a temperature dependent Henry's law constant (Andersson et al., 2008). Hg_{aq}^{0} and Hg_{air}^{0} are the modeled concentrations of elemental Hg in the mixed layer waters and in the lowest layer of the atmosphere, respectively. In our model, the ocean mercury in the mixed layer interacts not only with the atmospheric boundary layer but also with the subsurface waters through entrainment/detrainment of the mixed layer and wind-driven Ekman pumping.

Multiple global GEOS-Chem model simulations with nested grid over North America are performed to test different representations and hypotheses of atmosphere–surface exchange of Hg^0, including a reference simulation following Song et al. (2015) referred to here as "REF", a simulation "INV" that is based on global observational constraints from inverse modeling (Song et al., 2015), and four sensitivity simulations (HSO, HOX, HOXSO, and HOCEAN). The global mercury budgets of several model simulations are shown in Table 3.1.

In REF, global anthropogenic mercury emissions are taken from the United Nations Environment Programme (UNEP) for 2010 (AMAP/UNEP, 2013). Over North America, UNEP 2010 emissions are replaced by U.S. EPA's National Emissions Inventory (NEI) and Environment Canada's National Pollutant Release Inventory (NPRI), both based on activity data for 2011 (Environment Canada, 2013; U.S. EPA, 2013). These inventories result in global emissions of 1598 Mg yr^{-1} Hg^0 and 340 Mg yr^{-1} Hg^{II}. Net terrestrial emission fluxes of Hg^0 can be calculated as the sum of soil volatilization, rapid recycling, and dry deposition of Hg^0 over land. In REF, the net terrestrial and oceanic fluxes of Hg^0 are 960 and 2960 Mg yr^{-1}, respectively, at a global scale (see Table 3.1).

Song et al. (2015) optimized four model parameters and emission fluxes, including soil volatilization, Asian anthropogenic emission, and two ocean physicochemical parameters (the rate constant of dark oxidation of Hg_{aq}^{0} and the partition coefficient of Hg_{aq}^{II} on particles), using a Bayesian inversion approach and global ground-based atmospheric mercury observations. These changes are applied in the sensitivity simulation of INV. As shown in Song et al. (2015),

the anthropogenic Asian emission of Hg^0 in the UNEP 2010 inventory is increased by 90%, and the soil volatilization in the REF is reduced by 76% (see Figure 3.2). Changing the two ocean parameters affects the modeled global ocean mercury budget, particularly the mass exchange between the mixed layer and subsurface waters, and also the magnitude and seasonality of Hg^0 evasion from the ocean surfaces. On a global scale, the net terrestrial and oceanic Hg^0 surface fluxes modeled by INV are -280 and 3260 Mg yr^{-1}, respectively (see Table 3.1).

Table 3.1. Global budgets of mercury from three GEOS-Chem model simulations.

	REF	INV	HOXSO
Hg mass in the troposphere (Mg)			
Hg^0	4230	4070	3700
Hg^{II}	520	510	550
Hg mass in the ocean mixed layer (Mg)			
Hg^0	270	250	260
Hg^{II}	3050	3950	4040
Hg emission (Mg yr^{-1})			
Hg^0, anthropogenic	1600	2290	2290
Hg^{II}, anthropogenic	340	340	340
Hg^0, net oceanic	2960	3260	3530
Hg^0, geogenic	90	90	90
Hg^0, biomass burning	380	380	380
Hg^0, soil volatilization	1700	410	610
Hg^0, quick re-evasion	580	560	600
Hg deposition (Mg yr^{-1})			
Hg^0, dry deposition over land	1320	1250	1190
Hg^{II}, dry deposition	730	700	720
Hg^{II}, wet deposition	4450	4320	4880
Hg^{II}, sea salt scavenging	1130	1070	1060
Hg redox (Mg yr^{-1})			
Oxidation of Hg^0 by BrO_x	5970	5750	6320

The global budget of HOCEAN is similar to that of HOXSO, as only net oceanic Hg^0 flux from the Northwest Atlantic during summer is changed.

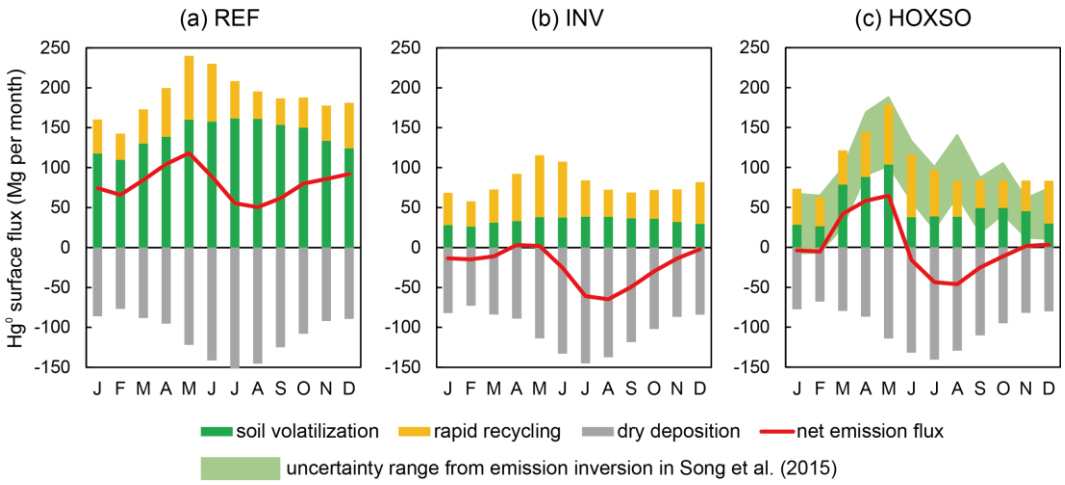

Figure 3.2. Seasonal variations of terrestrial fluxes of Hg^0 from three model simulations. The monthly Hg^0 terrestrial fluxes (soil volatilization, rapid recycling, and dry deposition) modeled by REF, INV, and HOXSO are shown in (a), (b), and (c), respectively. The net emission flux is the sum of the three unidirectional processes. The 1σ uncertainty range from the emission inversion in Song et al. (2015) is also indicated in (c).

Several sensitivity GEOS-Chem model simulations (HOX, HSO, and HOXSO) are conducted by making additional changes to INV. The enhanced concentration levels of Hg^{II} and BrO were measured in the free troposphere during the NOMADSS aircraft campaign, supporting the role of bromine as the dominant Hg^0 oxidant (Gratz et al., 2015). Using the default tropospheric bromine fields and the oxidation mechanism (as described above), modeled Hg^{II} levels are about a factor of 3 too low (Shah et al., 2016). Therefore, in HOX, we increase the rates of Hg^0 oxidation to Hg^{II} by tripling the summertime bromine radical (BrO_x = Br + BrO) concentrations in the tropical and subtropical free troposphere (45° S–45° N; from 750 hPa to the tropopause), in order to match the observed high levels of Hg^{II} during NOMADSS. Shah et al. (2016) showed that using faster oxidation kinetics (Ariya et al., 2002) could also simulate the observed high Hg^{II} levels during NOMADSS. Recent studies have indicated that the bromine fields and kinetics used in current atmospheric models are both very uncertain (Ariya et al., 2015), but a detailed discussion on atmospheric oxidation and reduction is beyond the scope of this work. We hypothesize that the mid-latitude terrestrial flux of Hg^0 in spring may be enhanced based on the evidence from both atmospheric mercury modeling and surface flux measurements (Section 3.3.1). Therefore, in HSO, the springtime soil volatilization

in the mid-latitudes (20°–60°) is increased by a factor of 4 in order to evaluate this hypothesis against atmospheric observations. We will show below that this increase improves the model's ability to reproduce the seasonal pattern of observed Hg^0 concentration in the NADP AMNet network. In "HOXSO", we combine HOX and HSO by increasing both summertime oxidation and springtime soil volatilization. As shown in Table 3.1, these changes influence the modeled net terrestrial Hg^0 emission, Hg^0 oxidation, and Hg^{II} wet deposition. The sensitivity simulation "HOCEAN" is the same as HOXSO, except that net oceanic Hg^0 flux from the Northwest Atlantic during summer is increased by 80% (derived from the comparison between model results of HOXSO and ship cruise observations. In Section 3.2, these model simulation results are compared to different types of observations in eastern North America.

3.2 Results

3.2.1 Observed Hg^0 in NOMADSS

During 19 research flights, 1589 2.5-minute observations of Hg^0 were sampled by the DOHGS. We select those observations within the planetary boundary layer (PBL), where rapid atmosphere–surface exchanges of chemical species take place. PBL heights exhibit significant spatiotemporal variations, and are typically diagnosed from vertical profiles of meteorological parameters measured by radiosonde soundings (Liu and Liang, 2010). However, the PBL height for each NOMADSS data point cannot be determined in such a way since sounding measurements are limited in time and space (Seidel et al., 2010). Here, we select observations below the lower of 1.2 km (a fixed PBL height estimated from the vertical profile of potential temperature observed in all research flights, see Figure 3.3) and the modeled PBL height in the GEOS-5 FP meteorological fields. It should be noted that over the summertime southeastern United States the daytime GEOS-5 FP PBL heights may have a 30–50% positive bias against LIDAR and ceilometer measurements (Kim et al., 2015). From a sensitivity model simulation that decreases the daytime GEOS-5 FP PBL heights by 40%, we find that such potential bias does not significantly affect our results and the conclusion remains unchanged. About 30% (466 data points out of 1589) of the NOMADSS Hg^0 observations are identified within the PBL. The within-PBL Hg^0 observations have a significantly larger ($p < 0.001$) median concentration of 1.47 ± 0.10 ng m^{-3} than free tropospheric Hg^0 observations (1.37 ± 0.12 ng m^{-3}), with

significance determined by the non-parametric Mann-Whitney *U* test (Rosner and Grove, 1999). This vertical gradient indicates Hg^0 oxidation in the free troposphere (Shah et al., 2016). The air within the PBL is characterized by a high water vapor mixing ratio (WVMR) of 12.7 ± 1.4 g kg^{-1} whereas the free troposphere is much drier (WVMR ~ 2.2 ± 2.7 g kg^{-1}). We further remove about 3% (13 data points out of 466) of the within-PBL observations with the highest 1% of concentrations of SO_2, NO_x, or propane to avoid the influence of nearby anthropogenic sources (Ambrose et al., 2015; Miller et al., 2013). Measurements made over Lake Michigan in RF-15 are also screened out.

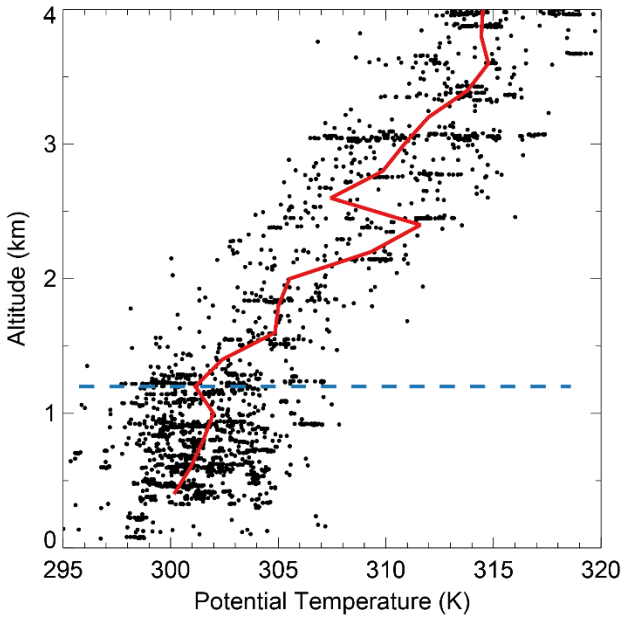

Figure 3.3. Vertical profile of potential temperature observed during all the NOMADSS research flights. The altitude of 0–4 km is shown. Each black circle is an individual 2.5 min observational data point merged based on the sampling interval of the DOHGS. The red line displays the medians of potential temperature for each 0.2 km vertical bin. The dashed blue line indicates the altitude of 1.2 km which is one of the two criteria to select observations within the PBL. This altitude is determined by inspecting the vertical profile of potential temperature. Within 1.2 km, potential temperature is nearly constant with height; whereas above 1.2 km, it increases sharply with altitude.

The selected background within-PBL NOMADSS observations are then divided into two groups: those over terrestrial and over oceanic surfaces. The air over oceanic surfaces was sampled in two flights out to the Northwest Atlantic (RF-14 and RF-16) and one flight out to

the Gulf of Mexico (RF-12). Measurements over terrestrial surfaces were made in 14 out of the 19 flights. The extremely low mixing ratios of isoprene (0.00 ± 0.01 ppbv) and high levels of DMS (8.26 ± 4.37 pptv) observed over oceanic surfaces, compared to those observed over terrestrial surfaces (isoprene of 1.38 ± 0.49 ppbv and DMS of 1.95 ± 1.63 pptv), suggest that the two groups represent different types of air masses (Table 3.2). The median Hg^0 concentration observed over oceanic surfaces (1.55 ± 0.11 ng m^{-3}, N = 73) is significantly higher than that over terrestrial surfaces (1.45 ± 0.09 ng m^{-3}, N = 360) ($p < 0.001$, Mann-Whitney U test).

Table 3.2. Observed and modeled Hg^0 concentrations during NOMADSS.

	Over terrestrial surfaces		**Over oceanic surfaces**		**Mann-Whitney *U* test**
	Median ± MAD	***N. of samples***	**Median ± MAD**	***N. of samples***	
Background within-PBL NOMADSS observations					
Hg^0 (ng m^{-3})	1.45 ± 0.09	*360*	1.55 ± 0.11	*73*	$p < 0.001$
Isoprene (ppbv)	1.38 ± 0.49	*358*	0.00 ± 0.01	*71*	$p < 0.001$
DMS (pptv)	1.95 ± 1.63	*176*	8.26 ± 4.37	*60*	$p < 0.001$
REF					
Hg^0 (ng m^{-3})	1.39 ± 0.03	*360*	1.32 ± 0.03	*73*	$p < 0.001$
INV					
Hg^0 (ng m^{-3})	1.30 ± 0.03	*360*	1.28 ± 0.02	*73*	$p = 0.45$
HOXSO					
Hg^0 (ng m^{-3})	1.29 ± 0.05	*360*	1.26 ± 0.05	*73*	$p < 0.001$
HOCEAN					
Hg^0 (ng m^{-3})	1.29 ± 0.03	*360*	1.29 ± 0.05	*73*	$p = 0.67$

3.2.2 Comparison between Model and Observations

Below, we compare model simulation results with Hg^0 concentration observations from eleven ground-based sites, three ship cruises, and the NOMADSS campaign, as well as the wet deposition data of Hg^{II}. Figure 3.4 shows the average Hg^0 concentration measured at the 11 NADP AMNet ground-based sites. The average observation in 2013 is similar to that in 2009–2012, both of which indicate pronounced seasonal variations with a maximum of Hg^0 in late winter and early spring (about 1.45 ng m^{-3} in February–April) and a minimum in late summer

and early fall (about 1.20 ng m^{-3} in August–October). We use the Normalized Root Mean Square Error (NRMSE) to evaluate the performance of model simulations (see Chapter 2). A smaller NRMSE indicates a better model performance. Compared to the average NADP AMNet observation in 2013, the NRMSE values for REF, INV, HOX, HSO, and HOXSO are 0.14, 0.09, 0.09, 0.10, and 0.05, respectively, and HOXSO has the best performance among them.

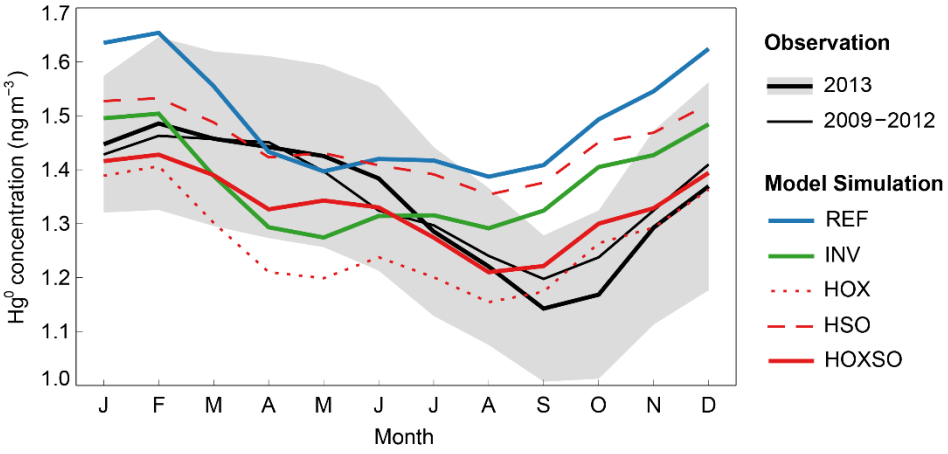

Figure 3.4. Averaged monthly observations and model simulations of Hg^0 concentrations for the NADP AMNet ground-based sites. The thick black line and gray shaded region show the average and 1σ uncertainty range of observed Hg^0 concentration in 2013. The thin black line shows the average observation in 2009–2012. The blue, green, and red solid lines indicate model results from REF, INV, and HOXSO, respectively. The dotted and dashed red lines indicate model results from HOX and HSO, respectively.

As shown in Figure 3.4, HOXSO is also the only simulation that reproduces the observed seasonal pattern of Hg^0 concentration. The two changes applied in HOXSO, the faster summertime Hg^0 oxidation (also made in HOX) and the elevated springtime mid-latitude soil volatilization (also made in HSO), are both essential for modeling this seasonal pattern. The tripled summertime BrO_x accelerates the conversion of Hg^0 to Hg^{II} through oxidation, and thus the modeled Hg^0 concentration in HOXSO shows a similar decreasing gradient (~ -0.06 ng m^{-3} $month^{-1}$) during the summer months with the observation in 2013 (~ -0.08 ng m^{-3} $month^{-1}$) and in 2009–2012 (about -0.04 ng m^{-3} $month^{-1}$). However, the model simulations without enhanced oxidation (REF, INV, and HSO) cannot reproduce this feature in the observed Hg^0

concentration. In contrast, the simulations without elevated soil volatilization (REF, INV, and HOX) show a large decline of about 0.23 ng m^{-3} in modeled Hg^0 during the spring months, which is not seen in the ground-based observations. By increasing springtime soil volatilization, HOXSO better reproduces the observed Hg^0 trend in this season. Since the two sensitivity simulations, HOX and HSO, cannot reproduce the observed seasonal pattern of ground-based Hg^0, hereafter we do not compare their results with ship cruise and aircraft measurements.

Figure 3.5 shows the comparison of Hg^{II} wet deposition fluxes between the MDN measurements and different model simulations (REF, INV, and HOXSO) during 2013 summer over eastern North America. REF and INV have similar insignificant positive biases of +2% and +1%, respectively. This is because only Hg^0 surface fluxes differ between these two simulations. HOXSO shows a large positive bias of +59% due to the enhanced bromine radical fields used in this sensitivity simulation. It is noted that this bias should become smaller if an in-plume Hg^{II} reduction is applied in GEOS-Chem (Zhang et al., 2012b).

Table 3.3 compares the observed and modeled Hg concentrations in both the atmospheric boundary layer and the ocean mixed layer for three summertime ship cruises in the Northwest Atlantic Ocean (Soerensen et al., 2013). These simulations (REF, INV, and HOXSO) produce air Hg^0 concentrations (1.2–1.4 ng m^{-3}) within the uncertainty ranges of the observations. Among these simulations, REF leads to the lowest mixed layer concentrations of both Hg_{aq}^0 and Hg_{aq}^T, whereas HOXSO predicts the highest. Compared with measurements, REF and INV underestimate mixed layer Hg_{aq}^0 concentrations by 17–54% and 12–51%, respectively. HOXSO models comparable Hg_{aq}^0 concentrations for one ship cruise (AUG08), but still underestimates its levels for the other two (up to 40%). On average, HOXSO underestimates the observed mixed layer Hg_{aq}^0 by about 20%. As shown in Figure 3.6b–d, the modeled net oceanic Hg^0 emission fluxes also follow the order of REF < INV < HOXSO. Considering that HOXSO may underestimate mixed layer Hg_{aq}^0 concentrations by 40% and that different gas exchange parameterizations may lead to a 30% variability in estimated oceanic Hg^0 fluxes (Andersson et al., 2007; Sunderland et al., 2010), we conduct an additional sensitivity simulation referred to as HOCEAN, in which the net Hg^0 fluxes from the Northwest Atlantic (100–60° W, 15–45° N) during the summer months (June–July–August) are increased by 80% above the oceanic Hg^0 fluxes in HOXSO. HOCEAN thus represents a potential upper limit of

oceanic emissions from the Northwest Atlantic determined from the above model–observation comparison of ship cruises.

Table 3.3. Observed and modeled air and aqueous Hg for three summertime Northwest Atlantic ship cruises.

	AUG08			JUN09			AUG10		
	air Hg^0	**Hg_{aq}^0**	**Hg_{aq}^T**	**air Hg^0**	**Hg_{aq}^0**	**Hg_{aq}^T**	**air Hg^0**	**Hg_{aq}^0**	**Hg_{aq}^T**
OBS	1.4 ± 0.2	133 ± 14	1.3–2.9	1.4 ± 0.1	120 ± 7	N/R	N/R	196 ± 34	1.2–1.6
REF	1.40	110	1.3	1.33	78	0.9	1.31	91	1.1
INV	1.37	117	1.6	1.31	94	1.2	1.30	96	1.3
HOXSO	1.32	143	1.9	1.32	98	1.3	1.17	123	1.6

N/R, not reported. Observations are obtained from Soerensen et al. (2013). For the cruise in August 2008, we exclude aqueous mercury data measured in the coastal Gulf of Maine because they were affected by anomalously high freshwater inputs. The units of air Hg^0, Hg_{aq}^0, and Hg_{aq}^T are ng m^{-3}, fM (10^{-12} mol m^{-3}), and pM (10^{-9} mol m^{-3}), respectively.

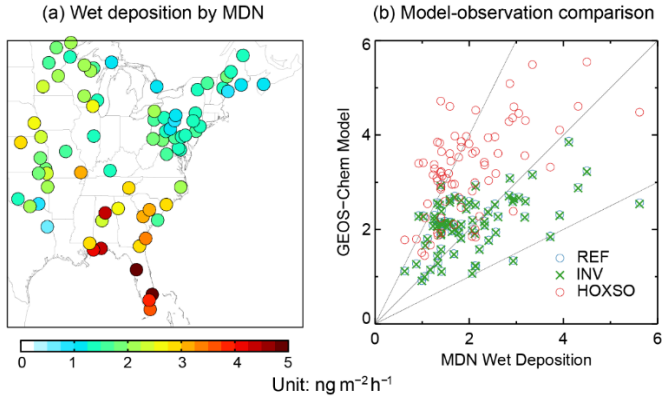

Figure 3.5. The wet deposition data measured by the NADP MDN and its comparison with different model simulations in 2013 summer. The plot in (a) shows the spatial distribution of measurement sites in the eastern North America. The plot in (b) shows the model–observation comparison for REF, INV, and HOXSO. The gray solid lines indicate 1:2, 1:1, and 2:1, respectively.

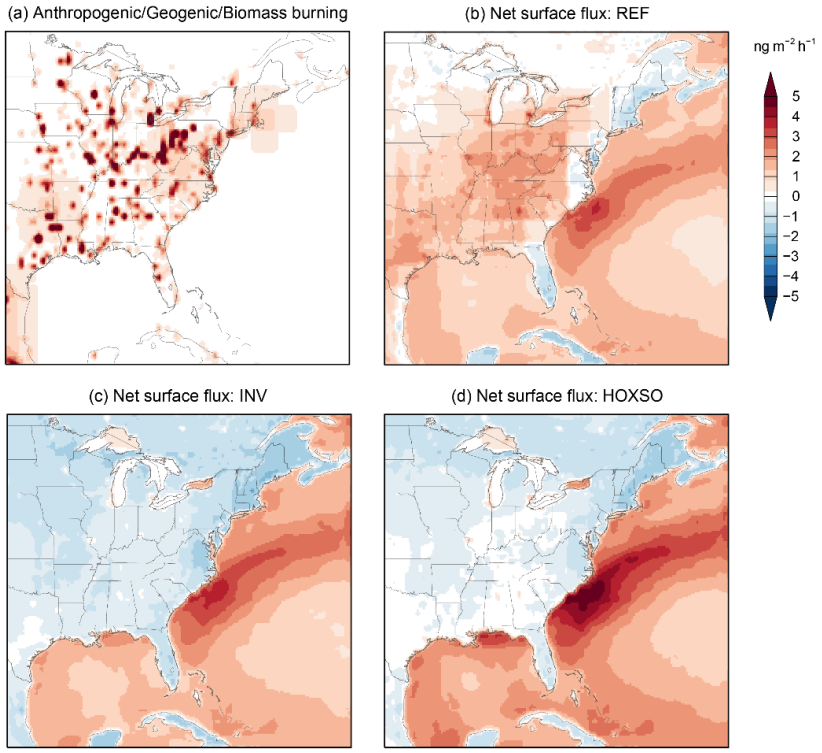

Figure 3.6. Spatial distributions of modeled atmospheric Hg^0 fluxes in eastern North America in summer. The average fluxes during the summer months (June–July–August) are shown. The sum of the three unidirectional emissions (anthropogenic, geogenic, and biomass burning) is shown in (a). The net terrestrial and oceanic fluxes from REF, INV, and HOXSO are plotted in (b), (c), and (d), respectively.

Table 3.2 shows the background within-PBL Hg^0 observations during the NOMADSS aircraft campaign, divided into two groups (over terrestrial and over oceanic surfaces), and the corresponding model results from REF, INV, HOXSO, and HOCEAN. All these model simulations predict lower Hg^0 concentrations than the DOHGS observed. The modeled median concentrations of Hg^0 over terrestrial surfaces range from 1.29–1.39 ng m^{-3}, about 4–11% lower than its observed median of 1.45 ng m^{-3}. This difference generally falls within the overall measurement uncertainty range of 6–10% of the DOHGS. In contrast, by comparing the observed and modeled Hg^0 concentrations (1.33 and 1.30–1.42 ng m^{-3}, respectively) during the NOMADSS period (2013 June–July) for the 11 AMNet ground-based sites in the eastern United States, we do not find a consistent negative bias in our model simulations. As described earlier, the DOHGS observed a significantly higher Hg^0 concentration of 0.10 ng m^{-3} over oceanic surfaces in the Northwest Atlantic than over terrestrial surfaces in the eastern United States.

However, our model simulations cannot reproduce this land–ocean difference. As shown in Table 3.2, REF, INV, and HOXSO indicate that the median Hg^0 concentrations over oceanic surfaces are 0.07 ($p < 0.001$), 0.02 ($p = 0.45$), and 0.03 ($p < 0.001$) ng m^{-3} lower than those over terrestrial surfaces. HOCEAN increases the summertime net Hg^0 flux from the Northwest Atlantic by 80% than HOXSO, and predicts comparable ($p = 0.67$) Hg^0 concentrations over terrestrial surfaces (1.29 ± 0.03 ng m^{-3}) and over oceanic surfaces (1.29 ± 0.05 ng m^{-3}). Among our sensitivity GEOS-Chem model simulations, HOCEAN can be considered as the best simulation with regard to the comparison with Hg^0 observations.

3.3 Discussion

3.3.1 Enhanced Terrestrial Flux of Hg^0 in Spring

We have described that HOXSO can reproduce the seasonal variation of Hg^0 concentration observed at the NADP AMNet ground-based sites with an enhanced springtime soil volatilization in the mid-latitude region (20°–60°). As shown in Figure 3.2, the net terrestrial fluxes of Hg^0 (the sum of soil volatilization, rapid recycling, and dry deposition) modeled by HOXSO are positive in the spring months. We hypothesize that the mid-latitude terrestrial flux of Hg^0 in spring may be enhanced based on the following evidence from both atmospheric mercury modeling and surface flux measurements. Song et al. (2015) quantitatively constrained monthly soil volatilization using worldwide ground-based observations and a Bayesian inversion approach. As shown in Figure 3.2, the 1σ uncertainty range of soil volatilization from the emission inversion revealed an enhancement during the spring months (Song et al., 2015), and increasing the soil volatilization by a factor of 4 agrees well with this modeling result. The measured net Hg^0 fluxes in the mid-latitudes for different land use types (i.e., forest, grassland, agriculture, and bare soil) and different seasons are summarized in Table 3.4. We find that most of them (7 out of 9) show higher terrestrial Hg^0 fluxes in spring (by 40% to a factor of 6) than the averages in other seasons. It has been suggested that springtime agricultural tilling operations can significantly mobilize Hg into the atmosphere from its soil pool (Bash and Miller, 2007). The small vegetation coverage in spring, which allows the penetration of solar radiation to the soil surface, may also be another important factor for the measured high Hg^0 emission fluxes (Choi and Holsen, 2009). It is important to note, however, that only limited terrestrial

flux measurements are available and very large uncertainties exist in them. Net deposition fluxes of Hg^0 during springtime have also been suggested (Converse et al., 2010).

Table 3.4. A summary of measured net emission fluxes of Hg^0 for different land uses and seasons.

Land use	Site location	Hg^0 flux (ng m^{-2} h^{-1})				Ref
		Spring	Summer	Fall	Winter	
Forest	New York (USA)	1.6 ± 3.0	1.5 ± 1.1	0.8 ± 1.0	0.2 ± 0.5	(1)
	Maryland (USA)	1.0 ± 0.9	-0.1 ± 0.4	0.4 ± 1.1	1.4 ± 1.5	(2)
	Tennessee (USA)	0.0 ± 0.3	0.4 ± 0.3	0.9 ± 0.6	0.6 ± 0.5	(3)
	Chongqing (China)	24.3 ± 9.9	12.8 ± 7.2	13.0 ± 6.2	6.1 ± 2.7	(4)
Grassland	Maryland (USA)	2.0 ± 1.0	-0.5 ± 1.5	-0.2 ± 0.7	0.7 ± 0.5	(2)
	Virginia (USA)	-4.8 ± 25.5	2.5 ± 19.1	0.3 ± 16.8	4.1 ± 25.7	(5)
Agriculture	Chongqing (China)	38.1 ± 66.8	7.4 ± 25.2	6.3 ± 11.9	N/R	(6)
	Chongqing (China)	61.2 ± 71.0	30.8 ± 34.0	15.5 ± 38.8	N/R	(6)
Bare soil	Chongqing (China)	25.9 ± 25.5	30.1 ± 27.1	21.8 ± 14.1	5.3 ± 5.1	(4)

N/R, not reported

References: (1) Choi and Holsen (2009), (2) Moore (2011), (3) Kuiken et al. (2008), (4) Ma et al. (2013), (5) Converse et al. (2010), and (6) Zhu et al. (2011).

3.3.2 Implications for Regional Terrestrial and Oceanic Hg^0 Fluxes

The NOMADSS aircraft campaign found higher Hg^0 concentrations over the Northwest Atlantic than over the eastern United States (Table 3.2). Gay et al. (2013) reported a similar finding by combining the NADP AMNet sites into several loosely defined groups, including a coastal/remote group (NS01 and NH06) and a continental/remote group (VT99, NY20, and GA40). Three years of data show that the former group has about 0.07 ng m^{-3} higher Hg^0 concentrations than the latter. However, the Hg^0 measurement systematic uncertainty for these NADP AMNet sites, which is estimated to be about 0.14 ng m^{-3} (10% of the observed Hg^0 concentration of 1.3–1.4 ng m^{-3}), is larger than this 0.07 ng m^{-3} difference between the two site groups, limiting our ability to apply these results in a modeling context. NOMADSS minimizes

potential systematic differences since the DOHGS was used to measure Hg^0 over both terrestrial and oceanic surfaces.

This land–ocean difference of atmospheric Hg^0 concentrations over eastern North America has important implications for regional terrestrial and oceanic Hg^0 fluxes. The modeled net surface fluxes in 100–60° W and 20–50° N during summer are shown in Figure 3.6b–d. Note that all model simulations also include the same three unidirectional sources that occur over land (i.e., anthropogenic, geogenic, and biomass burning), which together emit 3.1 Mg $month^{-1}$ Hg^0 from terrestrial surfaces (corresponding to an average Hg^0 flux of 0.8 ng m^{-2} h^{-1}), as shown in Figure 3.6a. REF emits an average net oceanic flux of 1.3 ng m^{-2} h^{-1} from the Northwest Atlantic and an average net terrestrial flux of 0.8 ng m^{-2} h^{-1} from the eastern United States. (Figure 3.6b). Thus, in REF, the total Hg^0 flux emitted over land (1.6 ng m^{-2} h^{-1}) is larger than that from oceanic surfaces (1.3 ng m^{-2} h^{-1}). As described earlier, in REF, the median Hg^0 over land is 0.07 ng m^{-3} higher ($p < 0.001$) than that over ocean, which is opposite to the observed land–ocean difference in NOMADSS. Among our model simulations, HOCEAN has the lowest terrestrial Hg^0 flux of -0.6 ng m^{-2} h^{-1} (total Hg^0 flux emitted over land is thus 0.2 ng m^{-2} h^{-1}) and the highest oceanic Hg^0 flux of 3.3 ng m^{-2} h^{-1}, and predicts the same Hg^0 concentrations (p = 0.67) over both surfaces in NOMADSS. Consequently, the above comparison between our model results and NOMADSS observations implies either even higher oceanic Hg^0 fluxes from the Northwest Atlantic or lower Hg^0 fluxes emitted from land in the eastern United States, or both, than the fluxes simulated by HOCEAN.

We have demonstrated through the model–observation comparison of ship cruises that HOCEAN represents a potential upper limit of oceanic emissions from the Northwest Atlantic. However, riverine discharges of Hg, an oceanic source that is not considered in the 2D mixed layer slab ocean of GEOS-Chem, may lead to additional Hg^0 emissions from coastal/shelf areas and help to reconcile the difference between model results and NOMADSS observations. Soerensen et al. (2013) found, during the ship cruise AUG08 in the Northwest Atlantic, that enhanced freshwater inputs due to anomalously high precipitation in July 2008 strongly increased the mixed layer Hg_{aq}^0 concentrations and Hg^0 fluxes in waters of the Gulf of Maine approximately 60 km offshore (270 ± 50 fM and 7.2 ± 4.2 ng m^{-2} h^{-1}), when compared to those in more open waters (130 ± 14 fM and 3.8 ± 2.9 ng m^{-2} h^{-1}). A spatial trend of higher Hg_{aq}^0

levels in coastal waters (~ 100 km) than in open waters has also been observed in other cruises (Ci et al., 2011). Two NOMADSS research flights, RF-14 and RF-16, sampled the oceanic air 50–150 km off the coast of South Carolina on July 5 and July 8 of 2013, respectively. Unusually high water discharges were measured in July 2013 for rivers in South Carolina (see Figure 3.8a for an example). Additionally, measurements within the NADP MDN (Gay et al., 2013) showed heavy rainfall and high wet deposition fluxes of Hg in late June and early July 2013, right before the sampling time of these two flights (see Figure 3.8b for an example). Overall, these results suggest that riverine discharges of mercury may contribute to the observed high Hg^0 concentration over the Northwest Atlantic.

HOCEAN simulates an average net terrestrial flux of -0.6 ng m^{-2} h^{-1}, meaning that the simulated terrestrial ecosystem in the eastern United States is a net sink of Hg^0 during summer. The simulated dry deposition of Hg^0 of 2.0 ng m^{-2} h^{-1} is only partially offset by its evasion that includes soil volatilization (0.6 ng m^{-2} h^{-1}) and rapid recycling of newly deposited Hg (0.8 ng m^{-2} h^{-1}). The global terrestrial flux measurement database (Agnan et al., 2016) suggests a small positive median Hg^0 flux of 0.1 ng m^{-2} h^{-1} (50% uncertainty range: -0.1 to 0.5 ng m^{-2} h^{-1}) over background bare soil, which is in agreement with measured vertical profiles of Hg^0 in soil pores (Obrist et al., 2014). However, forest is the most important land use type in the eastern United States, especially during summer when the leaf area index is maximum (thus leaf surface areas are several times larger than underlying soil surface areas) (Buermann et al., 2001; Drummond and Loveland, 2010). Figure 3.7 shows the different atmosphere-terrestrial mercury exchange processes involved in a forest ecosystem. Canopies can reduce Hg^0 evasion from underlying soils by absorbing most of the incoming solar radiation and suppressing the rising of soil temperature (Choi and Holsen, 2009; Wang et al., 2006). Foliage is well-known to constitute a net sink of atmospheric Hg^0 through stomatal and non-stomatal uptake (Stamenkovic and Gustin, 2009; Wang et al., 2014b), and the median Hg^0 flux measured over leaves at background forest sites is -0.12 ng m^{-2} h^{-1} with a 50% uncertainty range from -1.48 to 1.65 ng m^{-2} h^{-1} (Agnan et al., 2016). Hg translocation from soil to leaves is unlikely to be significant (Cui et al., 2014; Fay and Gustin, 2007). Therefore, it is not unreasonable to consider the summertime terrestrial ecosystem in the eastern United States as a net sink of Hg^0, given relatively low soil evasion and high foliage uptake. However, it is not possible to provide an accurate estimate for the magnitude of this sink, since reliable flux measurements over forests

are currently lacking, and the mechanism of Hg transport in plant/vegetation is not well understood (Agnan et al., 2016).

The unidirectional sources over land (i.e., anthropogenic, geogenic, and biomass burning) are also uncertain and their fluxes may be higher or lower than the values applied in our model. However, their uncertainties are small compared to those associated with terrestrial and oceanic fluxes in the studied region. In summer, simulated geogenic activities and biomass burning emit little atmospheric Hg^0 from the eastern United States (< 0.1 ng m^{-2} h^{-1} on average), and thus the contributions of their uncertainties on Hg^0 fluxes are insignificant in this context. The NEI 2011 inventory used in our model has an average Hg^0 flux of 0.7 ng m^{-2} h^{-1} in the eastern United States. In general, anthropogenic emissions in North America are considered to be relatively well constrained (1σ error around ± 30%) (Pacyna et al., 2010; AMAP/UNEP, 2013). Although U.S. EPA will not release the NEI inventory in 2013 (the year in which NOMADSS took place), another estimate, the Toxics Release Inventory (U.S. EPA, 2015), shows that the magnitudes of reported mercury anthropogenic emissions for 2011 and 2013 differ only slightly (< 2%).

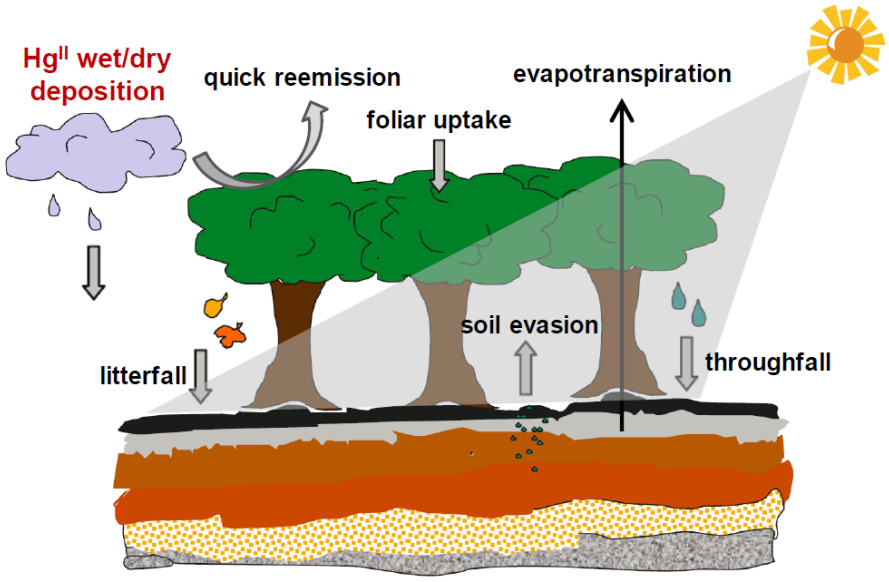

Figure 3.7. Different atmosphere-terrestrial mercury exchange processes involved in a forest ecosystem.

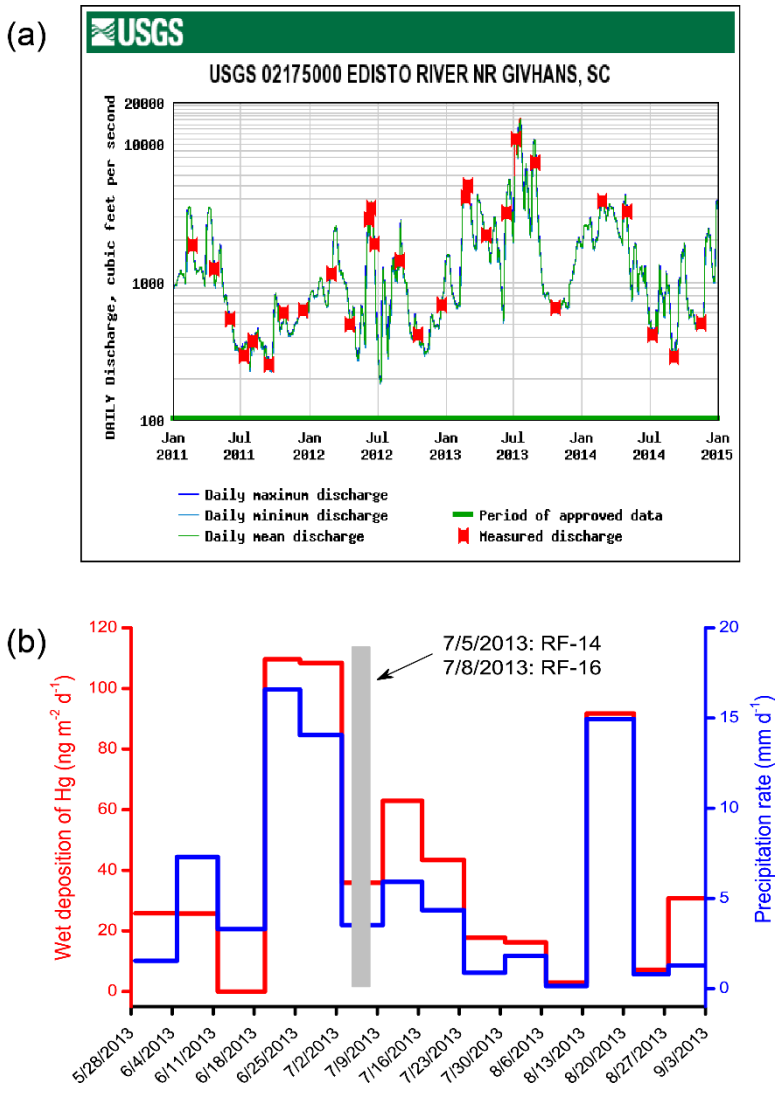

Figure 3.8. Examples of temporal changes in river water discharge from South Carolina into the Northwest Atlantic during recent years and measurements of precipitation rate and wet deposition flux of mercury in South Carolina during 2013 summer. The plot in (a) shows daily water discharges of the Edisto River measured at a USGS station (No. 02175000) near Givhans, South Carolina, from 2011–2014. Notice that vertical axis is expressed in a log scale, and that the highest water discharge during recent years was measured in July 2013. The plot in (b) shows measurements at a NADP Mercury Deposition Network (MDN) station (No. SC05; 32.9430° N, 79.6592° W) in 2013 summer. Both precipitation rate and Hg wet deposition peaked from June 19 to July 2, 2013, right before the over-water sampling dates (July 5 and 8, 2013) of the two NOMADSS research flights (RF-14 and RF-16). Similar temporal patterns of river water discharges, precipitation rates, and Hg wet deposition fluxes can be found for other stations in South Carolina on the USGS web page (http://waterdata.usgs.gov/usa/nwis/) and on the NADP MDN web page (http://nadp.sws.uiuc.edu/mdn/)

3.3.3 Origin of High Hg^0 Flux from the Northwest Atlantic

Based on the comparison between model results and aircraft and ship cruise observations, our analysis suggests a high Hg^0 flux from the Northwest Atlantic. In our simulations, this high Hg^0 flux helps to explain the land–ocean differences of observed atmospheric Hg^0 concentrations in the eastern North America, and also agrees with the observed high aqueous Hg^0 levels in the mixed layer. In contrast, a recent study classified Hg^0 data observed at the Mace Head station on the Northeastern Atlantic coast of Ireland into different air mass groups according to their geographical origins (Weigelt et al., 2015). Air masses originating mostly from the Northeast Atlantic were found to have generally lower Hg^0 concentrations (0.07 ± 0.04 ng m^{-3} calculated from monthly means and 0.04 ± 0.05 ng m^{-3} from monthly medians, both using data in 2010–2013) than those from continental Europe. As shown in Figure 3.9, our model simulations of the Northwest Atlantic, particularly the waters near the continental United States, have overall higher Hg^0 fluxes when compared to the Northeast Atlantic. This is qualitatively consistent with the different land–ocean patterns of observed atmospheric Hg^0 over the Northeast and Northwest Atlantic.

The model also enables us to identify physicochemical processes that lead to simulated high Hg^0 fluxes in the Northwest Atlantic (and the relatively low fluxes in the Northeast Atlantic). As suggested by Equation (3.1), the modeled Hg^0 fluxes are positively correlated with the mixed layer Hg_{aq}^0 concentrations, which are in turn determined by multiple processes in the mixed layer, including photochemical- and biological- redox reactions and adsorption/desorption on particles, and the vertical interactions of the mixed layer with the above atmosphere and subsurface waters. The wet/dry deposition of Hg^{II} from the atmosphere is a source of mercury in the mixed layer, whereas Hg^0 evasion into the atmosphere is a sink. Vertical exchanges between the mixed layer and subsurface waters include entrainment/detrainment, wind-driven Ekman pumping, and particle sinking (biological carbon pump) (Soerensen et al., 2010a; Batrakova et al., 2014; Song et al., 2015). Figure 3.10a shows the spatial distribution of net Hg^0 fluxes (modeled by HOXSO) from the North Atlantic Ocean (100° W–20° E, 20–60° N) in summer. The spatial distributions of modeled Hg fluxes associated with several above-mentioned processes are shown in Figure 3.10b–e. A comparison of the magnitude of these Hg fluxes indicates that the high wet deposition of Hg^{II} into the

Northwest Atlantic is the dominant process determining the simulated high net oceanic flux of Hg^0 from this region. The wet deposition of Hg^{II} is closely related to the precipitation rate, which also has a spatial pattern with generally higher values in the Northwest Atlantic, in particular the waters near the continental United States, and lower values in the Northeast Atlantic (Figure 3.10f). The summertime precipitation in the North Atlantic is influenced by the North Atlantic Subtropical High (NASH, also known as the Bermuda High), a semi-permanent high pressure system in the lower troposphere (Li et al., 2012). As shown in Figure 3.10f, strong precipitation is located along the western boundary of the NASH, which can be represented by the 1560 m geopotential contour line at 850 hPa (Li et al., 2011), while the precipitation rate in eastern side of the NASH is very small. Overall, the high simulated Hg^0 flux from the Northwest Atlantic is mainly a result of high wet deposition of Hg^{II}, which is in turn linked to high precipitation rates in this region during summer. Given the uncertainties in modeling oceanic mercury and the limited representation of these processes in our slab ocean model, however, our ability to draw process-based conclusions from this study is limited. Similarly, a more detailed 3D oceanic mercury model (Zhang et al., 2014) suggests that high wet deposition of Hg^{II} leads to high Hg^0 flux from the Northwest Atlantic (Zhang Y, personal communication).

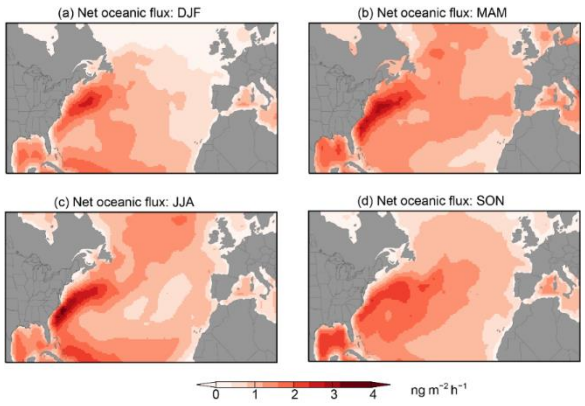

Figure 3.9. Seasonal variability and spatial distribution of modeled net oceanic Hg^0 flux from the North Atlantic. Results of the model simulation HOXSO are shown. The modeled net oceanic Hg^0 fluxes for different seasons are plotted in (a) December–January–February, (b) March–April–May, (c) June–July–August, and (d) September–October–November.

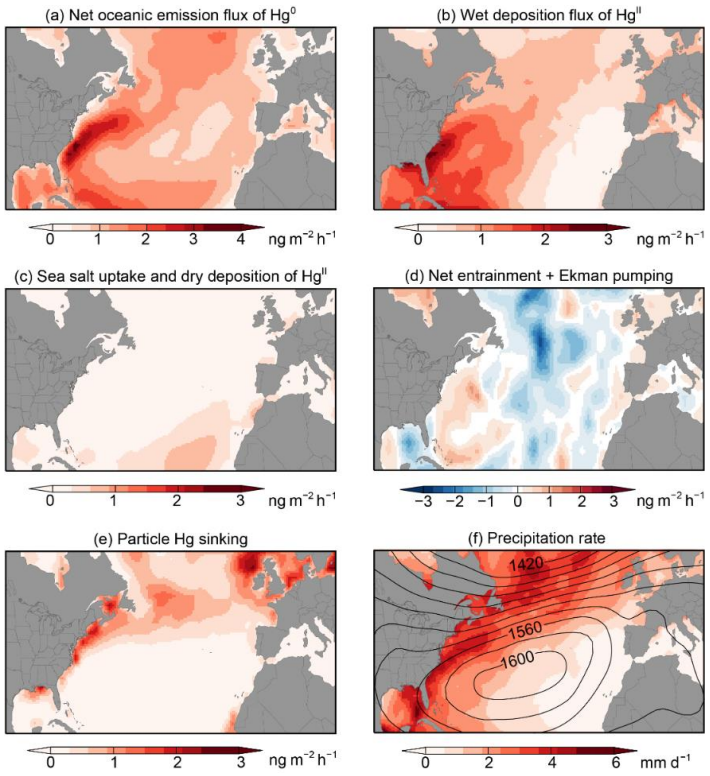

Figure 3.10. Spatial distributions of modeled vertical exchange fluxes in the North Atlantic in summer. Model results from HOXSO are shown. The plots in (a–e) indicate different mercury exchange fluxes between the atmosphere and the mixed layer and between the mixed layer and subsurface waters. The spatial distribution of precipitation rate is shown in (f) overlaid with geopotential height contour lines at 850 hPa. The geopotential height data are obtained from the NCEP/NCAR reanalysis (http://www.esrl.noaa.gov/psd/data/gridded/reanalysis/).

3.4 Conclusions

Atmosphere–surface exchange of Hg^0 in eastern North America is constrained by combining aircraft-based observations made during the 2013 summer NOMADSS campaign (as well as ground- and ship-based measurements) and GEOS-Chem CTM simulations. As a consistent instrumentation (the DOHGS) measured Hg throughout NOMADSS, the systematic uncertainty of Hg^0 concentration measurements at different locations is minimized. Within the PBL, significantly higher median Hg^0 concentrations were observed over oceanic surfaces of the Northwest Atlantic than over terrestrial surfaces of the eastern United States during NOMADSS ($p < 0.001$). The model simulation (HOCEAN) with a low (negative) terrestrial Hg^0 flux and a high (positive) oceanic flux in this region obtains the same Hg^0 concentrations

(p = 0.67) over both surfaces. Riverine discharges of mercury, an oceanic source that is not included in GEOS-Chem but may be significant in the NOMADSS period, may help to reconcile the model–observation discrepancy. By analyzing processes in the 2D mixed layer slab ocean of GEOS-Chem, we show that inferred high Hg^0 emission fluxes from the Northwest Atlantic may be a result of high wet deposition fluxes of oxidized mercury, which are in turn linked to high precipitation rates in this region. Given relatively low soil evasion and high foliage uptake, it is likely that terrestrial ecosystem in the summer eastern United States acts as a net sink of Hg^0. Increasing simulated terrestrial fluxes of Hg^0 in spring compared to other seasons can better reproduce seasonal variability of observed Hg^0 concentration at ground-based sites in eastern North America.

Chapter 4 A Model Calculation of the Diurnal Cycles of Mercury at Dome Concordia on the Antarctic Plateau

The remote Antarctic plateau receives significant inputs of mercury because this element is subject to long-range atmospheric transport and is readily cycled between surfaces and the atmosphere (Dommergue et al., 2010; Selin, 2009). Up to now, the variability of mercury over the plateau and its controlling processes have not been well understood. Previous measurements have suggested that a photochemically driven mercury cycle occurs at the air–snow interface and that the air was enriched in Hg^{II} (Brooks et al., 2008). Recently, Angot et al. (2016) reported the first year-round record of Hg^0 at the French-Italian Concordia Research Station, Dome C (75°06' S, 123°21' E). The observed Hg^0 concentrations in near surface air at Dome C showed a distinct diurnal cycle during summer, with a maximum around noon and a minimum around midnight. Such a pronounced diurnal cycle has not been observed at several coastal Antarctic stations (Pfaffhuber et al., 2012; Temme et al., 2003a) or at Summit Station, Greenland (Brooks et al., 2011). Despite these insights provided by mercury measurements over the Antarctic plateau, however, there remain many unanswered questions. For example, the oxidation mechanism of Hg^0 is unclear. We build a one-dimensional chemical and transport model of mercury and use it to simulate the diurnal cycles of mercury at Dome C during the summer and winter seasons of the year 2013. The goal of this study is to quantitatively explore and identify the most important processes contributing to the mercury variabilities at Dome C with implications for other polar regions.

4.1 Methodology

We describe a one-dimensional chemical and transport model for investigating the diurnal cycles of mercury in the atmospheric boundary layer (ABL) and surface snowpack at Dome C. As shown in Figure 4.1, the ABL consists of multiple vertical levels. The free troposphere and the surface snowpack are above and below the ABL, respectively. The parameterization of

vertical transport includes turbulent diffusion within the ABL, exchange between the top-most ABL level and the free troposphere, and deposition to and reemission from the underlying snowpack. Horizontal transport is not considered in our model and the reason will be given later. Mercury chemistry in the ABL consists of three gas phase oxidation schemes of Hg^0 initiated by OH, O_3, and Br, respectively. The model tracks both Hg^0 and Hg^{II} in a surface snow reservoir. The deposited Hg^{II} is photoreduced to Hg^0 which is reemitted into the bottom-most ABL level. These physical and chemical processes will be introduced in detail in the following subsections.

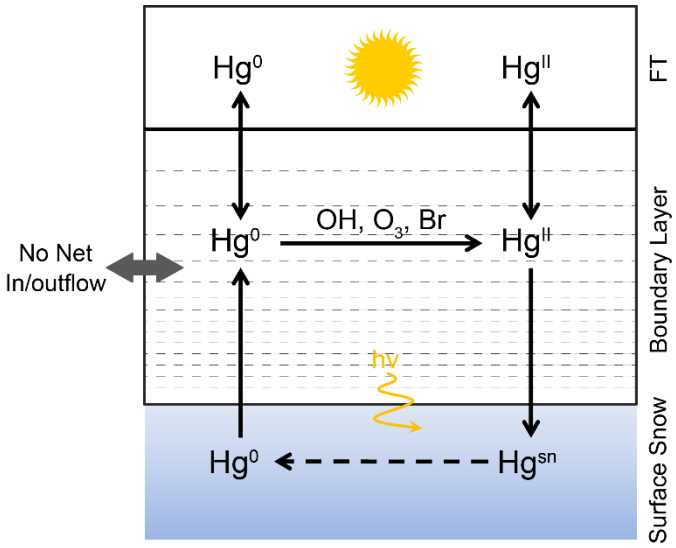

Figure 4.1. A schematic diagram of the 1-D chemical and transport model for mercury. FT represents free troposphere.

4.1.1 Vertical Transport

In our 1-D model, vertical transport is represented using the turbulent diffusion coefficients (K_z) calculated by a regional climate model Modèle Atmosphérique Régional, MAR (Gallée and Schayes, 1994). Briefly, MAR uses primitive equations with the hydrostatic approximation. Turbulence is parameterized using the Monin–Obukhov Similarity Theory and the local $E - \varepsilon$ model within and above the surface layer, respectively. The radiative transfer scheme in MAR

is the same as in ERA-40 reanalysis. Surface processes follow the "soil-ice-snow-vegetation-atmosphere transfer" scheme. More details on MAR and its validation at Dome C in summer and winter are given in Gallée and Gorodetskaya (2010) and Gallée et al. (2015). MAR simulations are shown to be in good agreement with meteorological observations at Dome C except under overcast sky conditions when cloud cover and downward longwave solar radiation tend to be underestimated (thus affecting the simulation of turbulence). K_z and other outputs from MAR have been used to estimate turbulent fluxes and/or mixing ratios of NO_x, HONO, and HCHO at Dome C (Legrand et al., 2014; Preunkert et al., 2015). Similar to these studies, the MAR data used in our 1-D model are obtained on a horizontal grid of 20 km centered at Dome C. The vertical resolution is 1.8 m from the snow surface up to the height of 28 m, and gradually decreases upward.

Model simulations are conducted using K_z and other meteorological outputs from MAR for the summer (Nov to Feb) and winter (May to mid-Aug) seasons of 2013 (Angot et al., 2016). We filter out the days with air masses originating from the Antarctic coast or the high troposphere above 500 hPa, through one-week backward trajectories computed using the Hybrid Single Particle Lagrangian Integrated Trajectory model (Figure 4.2) (Stein et al., 2015). HYSPLIT simulations are run every day starting at 10 m above surface on 1200 UTC, driven by meteorological data from the Global Data Assimilation System (GDAS, 1° × 1° resolution). The overcast sky days in summer are also removed based on the pictures taken at Dome C (Picard et al., 2016).

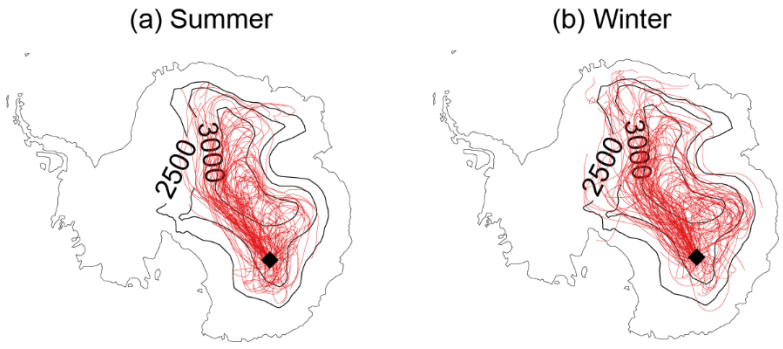

Figure 4.2. One-week backward trajectories arriving at Dome C in 2013 summer and winter. Days selected for our model simulations are shown only. The contours indicate altitude above sea level in meters.

The summertime ABL can be divided vertically into two superimposed domains, the mixed layers and the residual layers (Figure 4.3a), which interact with each other through entrainment and detrainment (Jacob and Wofsy, 1988). The depth of the mixed layers experiences a clear diurnal cycle as a result of the changing solar zenith angle (although the Sun is always above the horizon). The mixed layers are stable and shallow at night, deepen in the daytime, and then collapse rapidly. The wintertime ABL is even shallower and shows no diurnal cycle because of lack of solar radiation (Figure 4.3b). Above the ABL, we assume a well-mixed free troposphere where mercury concentrations are prescribed, as introduced in Section 4.1.3. Vertical exchange between the free troposphere and the top-most ABL level is estimated using the K_z at that level.

Our 1-D mercury model only considers vertical transport and assumes no net in/outflow in the horizontal direction. This assumption is justified at Dome C because of several reasons which include (1) the vertical mixing is very strong in the shallow ABL, (2) the terrain is flat and homogeneous, and (3) only days with air masses circulating in the lower troposphere over the plateau are used in our calculation.

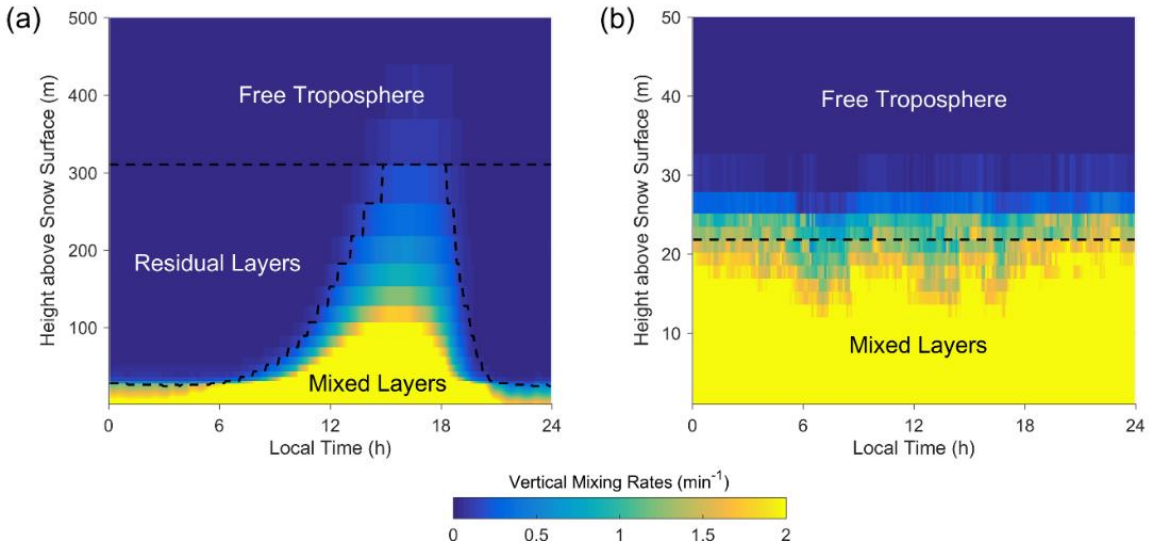

Figure 4.3. Vertical structures of the lower atmosphere in summer (a) and winter (b) represented by the average diurnal cycles of the mixing rates between adjacent vertical levels.

4.1.2 Atmospheric Mercury Chemistry

Our mercury model focuses on gas phase chemistry, and specifically, the OH, O_3, and Br oxidation schemes converting Hg^0 to Hg^{II}. Their rate constants from theoretical and experimental studies are summarized in Table 4.1. It should be noted that the actual mechanisms of $Hg^0 + O_3$ (R1) and Hg^0 + OH (R2) remain unclear. They are unlikely to proceed as pure gas phase reactions because the formation of a potential product HgO is highly endothermic (Hynes et al., 2009). The surface influence and/or the formation of a stable intermediate may make these reactions viable under atmospheric conditions (Subir et al., 2011). The two-step Br-initiated oxidation scheme (R3–R6) has been proven to explain the springtime Atmospheric Mercury Depletion Events (AMDEs) in the polar regions (Steffen et al., 2008), and may serve as the dominant oxidation pathway for Hg^0 in the global atmosphere (Holmes et al., 2006). The recombination of Hg^0 and Br atoms forms a thermally unstable Hg^IBr radical, which either dissociates or is further oxidized to the more stable Hg^{II} by a second radical (NO_2, HO_2, OH, Br, and BrO).

The concentrations of the primary oxidants (O_3, OH, and Br) and the secondary oxidants (NO_2, HO_2, and BrO) in the ABL need to be prescribed in the model. The O_3 and NO_x data in near surface air are obtained from *in situ* measurements at Dome C (Angot et al., 2016). The summertime HO_x data in near surface air are estimated from measurements in the Oxidant Production in Antarctic Lands and Export (OPALE) campaign during the summer 2011/2012 (Kukui et al., 2014). The wintertime HO_x data have not been measured but should be negligible due to lack of solar radiation. No direct surface measurements of BrO are yet available at Dome C. Legrand et al. (2016b) measured total gaseous inorganic bromine species (such as Br, BrO, HOBr, and Br_2) and concluded that BrO should be less than 1 pptv. In the same study, the p-TOMCAT model showed that the average BrO was 0.4 and 0.05 pptv in summer and winter, respectively, which agreed very well with the predictions from the GEOS-Chem model (0.4 and 0.07 pptv in summer and winter, respectively) (Sherwen et al., 2016). The concentrations of Br are calculated assuming a photochemical steady state between Br and BrO (Holmes et al., 2010; Platt and Janssen, 1995), as shown in Equation (4.1):

$$[Br] / [BrO] = (J_{BrO} + k_{BrO+NO} [NO]) / k_{Br+O3} [O_3] \quad (4.1)$$

where J_{BrO} is the photolysis frequency of BrO, and $k_{BrO+NO} = 8.8 \times 10^{-12} e^{260/T}$ and $k_{Br+O3} = 1.6 \times 10^{-11} e^{-780/T}$ (both in cm^3 $molecule^{-1}$ s^{-1}) are the rate constants for $BrO + NO \rightarrow Br + NO_2$ and $Br + O_3 \rightarrow BrO + O_2$, respectively. The value of J_{BrO} at local noon is archived from the GEOS-Chem model simulation with its diurnal cycle imposed based on downward shortwave solar radiation (BrO has a banded absorption spectrum in 290–380 nm). The values of k_{BrO+NO} and k_{Br+O3} are from JPL Evaluation Number 17 (available at http://jpldataeval.jpl.nasa.gov/).

We assume no vertical variability for O_3 and BrO throughout the ABL. Studies have shown that the snow surface processes (i.e., the photolysis of bromide and the subsequent evasion) do not contribute to the atmospheric BrO levels significantly (Legrand et al., 2016b). The vertical distributions of NO_x and HO_x are assumed by a model simulation of a hypothetical tracer, in which this tracer has an emission flux from the surface and a specified lifetime of several hours (Frey et al., 2015). These assumptions are based on the sources and sinks of these chemical species and agree with limited measurements of vertical profiles (Frey et al., 2015; Legrand et al., 2016a; Helmig et al., 2008; Thomas et al., 2011).

The model does not consider the oxidation of Hg^0 by NO, NO_2, and NO_3 because their products are too weakly bound theoretically (Dibble et al., 2012), although a positive correlation was found between Hg^{II} and NO_3 in a case study (Peleg et al., 2015). The kinetics of gas phase reactions of Hg^0 with many other species, including F, F_2, Cl, Cl_2, I, I_2, Br_2, BrCl, ICl, HCl, HOCl, ClO, BrO, and H_2O_2, have also been reported (Subir et al., 2011; Lin and Pehkonen, 1999; Ariya et al., 2015). However, either their concentrations or reaction rate constants are low enough so that these pathways are unimportant at Dome C, as discussed below. **Cl, F, and I.** The oxidation of Hg^0 by these halogen atoms has comparable rate constants with Hg^0 + Br (Dibble et al., 2012; Donohoue et al., 2005). However, Cl atoms react with CH_4, and thus their typical concentrations are three orders of magnitude lower than Br atoms in the polar regions (Hynes et al., 2009; Simpson et al., 2007). The concentrations of F are also very low because it reacts with water vapor (Subir et al., 2011). $Hg^{I}I$ is much more unstable than $Hg^{I}Br$ and undergoes thermal dissociation rapidly (Goodsite et al., 2004). **Cl_2, I_2, Br_2, BrCl, ICl, HCl, HOCl, and ClO.** The reactions of Hg^0 with these species have very low rate constants (from

10^{-19} to 10^{-17} cm^3 $molecule^{-1}$ s^{-1}, or even lower) (Ariya et al., 2015; Subir et al., 2011). **F_2.** The rate constant is 1.8×10^{-15} cm^3 $molecule^{-1}$ s^{-1} (Sumner et al., 2005). The atmospheric F_2 concentration is unknown but should be very low given its sources and sinks. **BrO**. The rate constant has been assumed to be from 10^{-15} to 10^{-14} cm^3 $molecule^{-1}$ s^{-1} in several studies (Wang et al., 2014a; Ye et al., 2016), at least 50 times lower than that by Br. Considering a Br/BrO ratio of 1:3 at Dome C (a typical ratio in summer), the BrO scheme is unimportant compared to the Br-initialized one. **H_2O_2.** According to a rate constant of $< 10^{-18}$ cm^3 $molecule^{-1}$ s^{-1} and a mixing ratio of 170 pptv measured at Dome C, the oxidation by H_2O_2 is negligible in summer (Ariya et al., 2015; Kukui et al., 2014).

The chemistry of mercury in the global atmosphere should include gas, aqueous, and heterogeneous reactions, but the current state of our understanding of their kinetics and mechanisms are far from complete (Hynes et al., 2009; Subir et al., 2012; Lin et al., 2006). Aqueous phase redox reactions occur mostly in cloud droplets; however, the likely importance of aqueous reactions is minimal in our simulations as the air over the Antarctic plateau is cold and dry and only clear sky days are selected. The surfaces allowing for heterogeneous reactions are aerosol, cloud droplets, snow, ice, water, soil, and vegetation (Subir et al., 2012). Only surface snow and drifting/blowing snow may be relevant in this particular environment (Six et al., 2004, 2005; Libois et al., 2014). There is some evidence that heterogeneous reactions on snow surfaces are possible at Dome C (Angot et al., 2016), but they are unlikely to substantially influence the diurnal variations of mercury.

4.1.3 Mercury in the Free Troposphere

To the best of our knowledge, there have been no mercury measurements in the free troposphere over the Antarctic plateau. Therefore, we rely on the simulated free tropospheric concentrations from global chemical and transport models, and specifically, the GEOS-Chem, GMHG, and GLEMOS models in a recent intercomparison study (AMAP/UNEP, 2015). They are very different in their parameterizations of spatial resolutions, natural and legacy emissions, and atmospheric chemistry. As shown in Figure 4.4, we validate these models against mercury observations at two background stations in the Southern Hemisphere, Amsterdam Island (AMS, 37°48' S, 77°33' E) and Cape Point, South Africa (CPT, 34°21' S, 18°29' E). For each season, we further correct the simulated mercury concentrations in each model using the corresponding

factor calculated from the model-observation comparison at AMS and CPT, assuming that these two stations can represent the background mercury levels in the Southern Hemisphere. This is a reasonable assumption given the long lifetime of mercury in the atmosphere.

Table 4.1. Gas phase mercury reactions used in our model.

No.	Reaction	Rate constant[a]	Reference
R1	$Hg^0 + O_3 \rightarrow Hg^{II}$	**1.7×10^{-18} (High)**	Iverfeldt and Lindqvist (1986)
		6.4×10^{-19}	Sumner et al. (2005)
		6.2×10^{-19}	Snider et al. (2008)
		$8.43 \times 10^{-17}\ e^{-11700/RT}$	Pal and Ariya (2004)
		3×10^{-20} (Low)	Hall (1995)
R2	$Hg^0 + OH \rightarrow Hg^{II}$	**$3.2 \times 10^{-13} \times (T/298)^{-3.06}$ (High)**	Goodsite et al. (2004)
		$3.55 \times 10^{-14}\ e^{2440/RT}$	Pal and Ariya (2004)
		8.7×10^{-14} (Low)	Sommar et al. (2001)
R3	$Hg^0 + Br \rightarrow Hg^IBr$	**3.2×10^{-12} (High)**	Ariya et al. (2002)
		$1.0 \times 10^{-12}\ e^{1738/RT}$	Khalizov et al. (2003)
		1.2×10^{-12}	Shepler et al. (2007)
		$1.5 \times 10^{-32} \times (T/298)^{-1.76} \times [M]$	Goodsite et al. (2012)
		$1.46 \times 10^{-32} \times (T/298)^{-1.86} \times [M]$ (Low)	Donohoue et al. (2006)
R4[b]	$Hg^IBr \rightarrow Hg^0 + Br$	$k_4\ [s^{-1}] = k_3 / (9.14 \times 10^{-24}\ e^{7801/T})$	Dibble et al. (2012)
R5	$Hg^IBr + Br \rightarrow Hg^0 + Br_2$	3.9×10^{-11}	Balabanov et al. (2005)
R6[c]	$Hg^IBr + X \rightarrow Hg^{II}$	8.6×10^{-11}	Ye et al. (2016)

[a] The unit of rate constants is $cm^3\ molec^{-1}\ s^{-1}$ unless otherwise stated. [R] = $J\ K^{-1}\ mol^{-1}$, [T] = K and [M] = $molec\ cm^{-3}$. "High" and "Low" in the parentheses indicate the highest and lowest reaction rate constants determined by different kinetic studies, respectively.

[b] R3 and R4 are a pair of reversible reactions, and k_4 is usually computed from k_3 and the equilibrium constant K_{eq}: $k_4 = k_3 / K_{eq}$. K_{eq} is calculated to be $9.25 \times 10^{-23} \times (T/298)^{-2.76}\ e^{7292/T}\ cm^3\ molec^{-1}$ by Goodsite et al. (2012), which is very close to the value given in this table ($K_{eq} = 9.14 \times 10^{-24}\ e^{7801/T}\ cm^3\ molec^{-1}$).

[c] X = OH, Br, HO_2, NO_2, BrO.

The corrected concentrations of speciated mercury ($Hg^T = Hg^0 + Hg^{II}$) from these global models are shown in Figure 4.5. In the lower free troposphere (500–600 hPa), all models predict

comparable Hg^T concentrations in both summer and winter, in the range of 0.9–1.0 ng m^{-3}. Hg^{II} concentrations are nearly zero in winter from all models, suggesting very low oxidation rates. The most obvious differences among different models are the simulated Hg^{II} concentrations in summer due to their different chemistry schemes. GEOS-Chem, GMHG, and GLEMOS use Br, OH, and OH/O_3 as the major oxidants of Hg^0, respectively. It is also noted that these models use the reaction rate constants at the low bounds. Thus in our modeling, the prescribed free tropospheric speciated mercury concentrations are adjusted based on the choice of oxidants, the concentrations of oxidants, and the choice of rate constants in different scenarios.

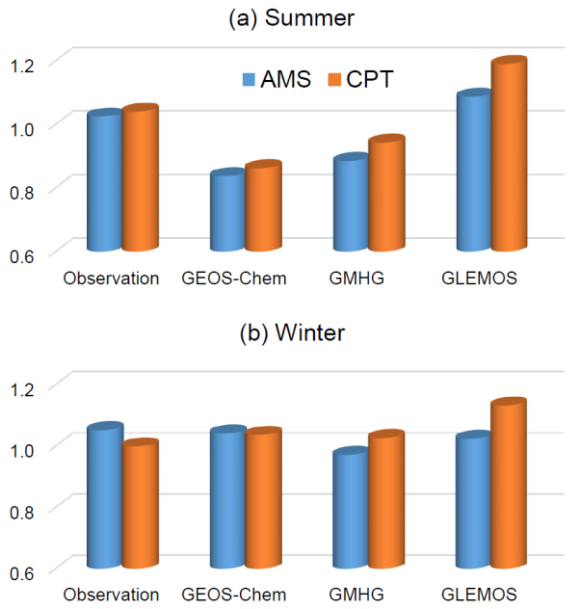

Figure 4.4. Comparison of Hg^0 concentration at AMS and CPT between observations and models (GEOS-Chem, GMHG, and GLEMOS) in 2013 summer and winter. The unit is ng m^{-3}.

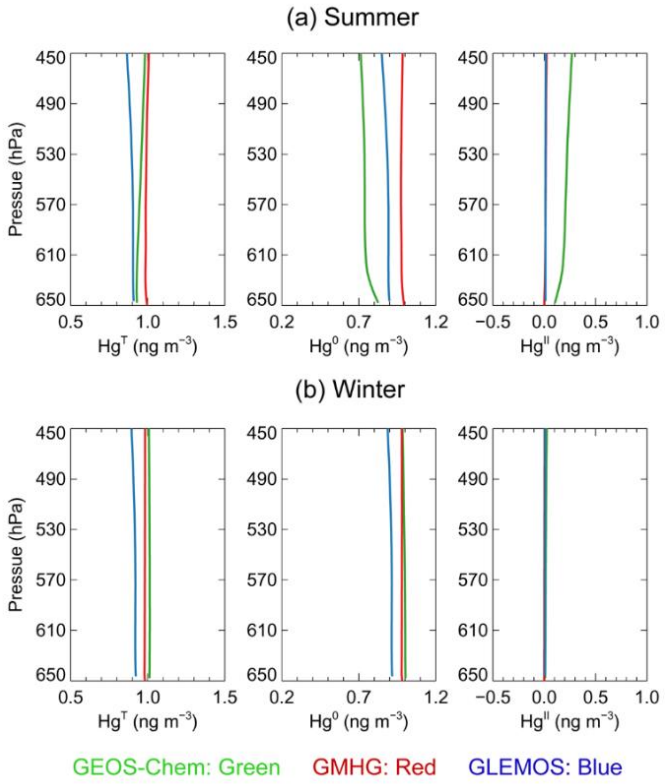

Figure 4.5. Vertical profiles of the simulated speciated mercury concentrations in the lower atmosphere in 2013 summer and winter. Note that the surface pressure at Dome C is about 650 hPa.

4.1.4 Mercury in Surface Snow and its Air–Snow Exchange

The atmosphere–surface exchange processes included in our model are dry deposition of Hg^{II} to and reemission of Hg^0 from the surface snowpack. The dry deposition flux is simply determined by the mercury concentration in the bottom-most ABL level and a prescribed dry deposition velocity (V_d) which has not been well constrained. The best estimate of V_d on the snow surface is 1 cm s^{-1} for Hg^{II} based on available studies, though it can be as high as 5 cm s^{-1} (Lindberg et al., 2002; Skov et al., 2006). Therefore, 1 cm s^{-1} is set as the default value for V_d, and the sensitivity of our model to this parameter will be discussed in Section 4.2.3.

Our knowledge of the postdepositional processes of mercury is still very limited. Previous research has suggested that, during the sunlit period, both photoreduction and photooxidation of mercury occur in surface snow, which very likely outcompete dark chemical processes and

thus control mercury levels in the snow interstitial air (Dommergue et al., 2003; Faïn et al., 2008; Poulain et al., 2004). Previous models have simply assumed a first-order photoreduction of snow Hg^{II} to Hg^0 in surface snowpack (e.g., Durnford et al., 2012; Toyota et al., 2014). At Dome C, the light penetration depth is about 10 cm (France et al., 2011). Accordingly, in our model, Hg^0 and Hg^{II} levels are tracked in a surface snow mercury reservoir with a 20 cm depth. The photoreduction of Hg^{II} is assumed to be proportional to the $J(O^1D)$, the photolysis rate of O_3, as observational studies have suggested that the UV-B is the most relevant solar radiation range (Durnford et al., 2012; Kukui et al., 2014). The average lifetime of surface snow Hg^{II} against photoreduction needs to be specified the model, which may range from several days to several weeks (Toyota et al., 2014). Brooks et al. (2008) estimated a lifetime of surface snow mercury of about 2 weeks at the South Pole. We later discuss the sensitivity to this assumed lifetime in our model. During summer, it has been measured that the average total mercury concentration is about 10 ng/L corresponding to about 600 ng m^{-2} mercury in this surface snow reservoir, which is used as the initial condition in our simulations. During winter, the air–snow exchange of mercury is weak because the oxidation of Hg^0 (and thus the formation of Hg^{II}) is much slower than that in summer, and thus we assume no reemission of Hg^0 from the snowpack.

The diffusive flux of Hg^0 from the snowpack to the lowest atmospheric layer is determined by the concentration difference of Hg^0 and the molecular and turbulent diffusion coefficients. The molecular diffusion coefficient is set to 6×10^{-6} m^2 s^{-1}. The value of the turbulent diffusion coefficient is parameterized using the near surface air turbulent kinetic energy (Durnford et al., 2012). The summertime Hg^0 concentration in the snow interstitial air is observed to peak at 10 cm below surface, where its concentration is 0.1–0.3 ng m^{-3} higher ($p < 0.05$) than at 50 cm above surface (Angot et al., 2016). This indicates a significant formation of Hg^0 in the surface snowpack and its subsequent reemission into the atmosphere.

4.2 Results and Discussion

In this section, the model simulation results during summer and winter are described, and then the crucial processes controlling the diurnal variabilities of mercury are discussed. The model sensitivities to several important parameters are also investigated. At the end, we answer

the question why such a diurnal pattern was not seen at Summit, Greenland, a station located in a similar environment to Dome C, Antarctica.

4.2.1 Summer

As described in Section 4.1, our model investigates three gas phase oxidation schemes of Hg^0. The concentrations of the primary oxidants in the mixed layers, O_3, OH, and Br, are shown in Figure 4.6a–c. Multiple model scenarios are conducted by varying both the concentrations of the oxidants and the reaction rate constants (Table 4.1) within their uncertainty ranges. The calculated lifetimes (τ) of Hg^0 in the mixed layers are shown in Figure 4.6d–f.

In summer, the Br scheme (τ ~ 1–10 days) is more efficient than the O_3 and OH schemes (τ ~ 10–10^3 days). The high rates of the two-step Br-initiated reactions at Dome C can be attributed to a combination of several factors, including low temperature, continuous sunlight, and high NO_x levels. The photodenitrification of the surface snowpack results in significant emissions of NO_x into the shallow ABL. The near surface NO_x concentrations of ~ 300 pptv at Dome C (Figure 4.7) are unusually large, at least an order of magnitude higher than in the Antarctic coast (Frey et al., 2015). As suggested by the relationship between Br and BrO in Equation (4.1), the continuous sunlight and high NO levels at Dome C lead to relatively high Br concentrations (e.g., [Br] = 0.13 pptv when [BrO] = 0.4 pptv) and thus high first step oxidation rates of Hg^0 + Br. In addition, the second step reaction of the intermediate Hg^IBr and NO_2 (the dominant oxidant among NO_2, HO_2, OH, Br, and BrO) can easily outcompete the dissociation of Hg^IBr in near surface air. This is partly because Hg^IBr is more stable under low temperatures (Table 4.1) and has a lifetime of ~ 10^3 seconds against thermal dissociation, and partly because NO_2 at Dome C is enriched in near surface air and oxidizes Hg^IBr very rapidly (in the order of seconds).

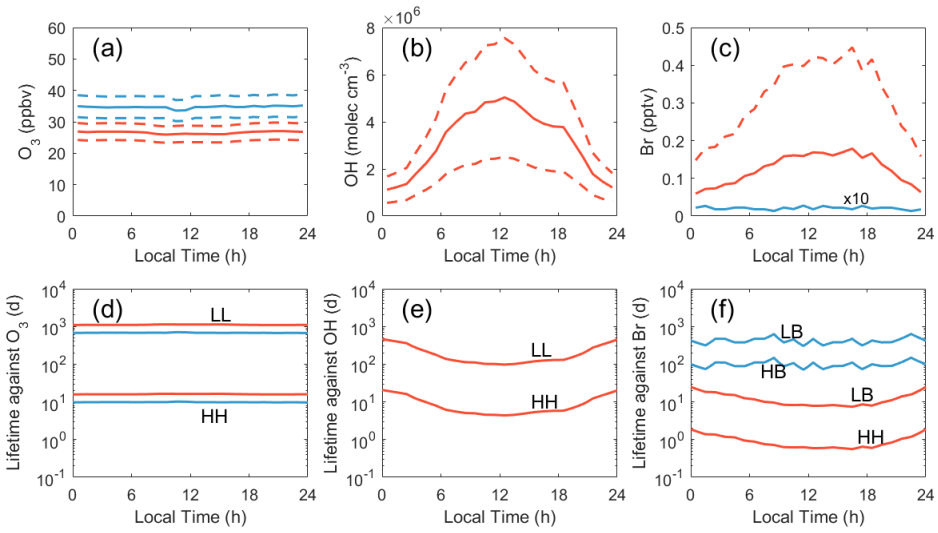

Figure 4.6. Diurnal variations of O_3, OH, and Br in near surface air in summer and winter. Red lines show the summer data and blue lines winter data. The solid lines in (a–c) are the observed average and the best estimate, whereas the dashed lines are the high and low bounds. The wintertime Br mixing ratio is multiplied by a factor of 10 for clarity, as shown in the blue solid line in (c). The lifetimes of Hg^0 against oxidation by O_3, OH, and Br are indicated in (d), (e), and (f), respectively. The two capital letters show the choice of the oxidant concentration (the former) and the choice of reaction rate constant (the latter). "H" means high, "L" low, and "B" best estimate. OH concentrations in winter are negligible and thus not shown.

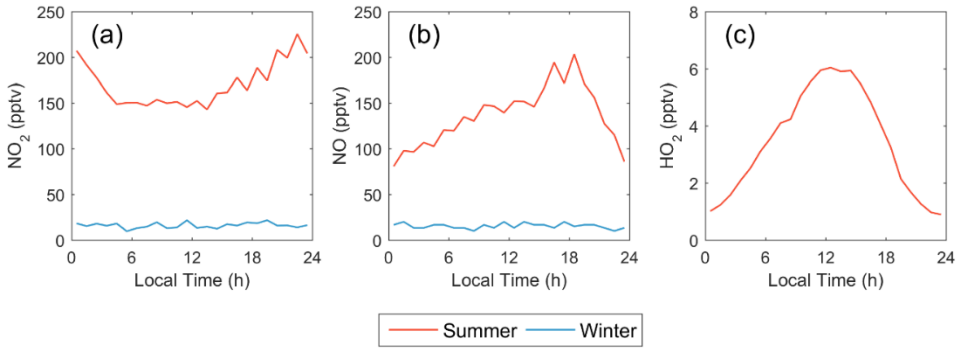

Figure 4.7. Concentrations of NO_2, NO, and HO_2 in near surface air in summer and winter. HO_2 concentrations in winter are negligible and not shown.

The observed mercury concentrations in summer at Dome C are shown in Figure 4.8a. Measurements were made at three inlets (0.25 m, 2.1 m and 10.7 m) and have been introduced

in detail in Angot et al. (2016) including the techniques and quality control programs. The average Hg^0 concentration of 0.5 ng m^{-3} at Dome C, which is significantly lower than the levels recorded at the same period in the Antarctic coastal stations, suggests that an intensive oxidation of Hg^0 occurs over the plateau (Angot et al., 2016). The pronounced diurnal cycle of Hg^0, with a maximum around noon and a minimum around midnight, has not been observed at several coastal Antarctic stations (Pfaffhuber et al., 2012; Temme et al., 2003a) or at Summit Station, Greenland (Brooks et al., 2011).

The configurations for several model scenarios are shown in Table 4.2. In all these scenarios, a V_d of 1 cm s^{-1} is used, and the free tropospheric total mercury concentration is assumed to be 0.9 ng m^{-3}. The lifetime of mercury in surface snow against the photoreduction is set to 2 weeks. The free tropospheric Hg^{II} concentrations are based on the choice of oxidants, the concentrations of oxidants, and the rate constants. The model scenarios using the OH and O_3 oxidation schemes (S1_O3_HH and S2_OH_HH) overestimate the concentrations of Hg^0 and do not show pronounced diurnal variations of Hg^0, even when the high oxidant levels and the high reaction rate constants are assumed. In the above two scenarios, the lifetimes of Hg^0 against oxidation are about 10 days (Figure 4.6), and the simulated average Hg^{II} concentrations are very small. The model scenarios using the Br oxidation scheme may predict comparable concentrations of Hg^0 (S3_Br_HH, $\tau \sim$ 1–2 days) or overestimate its concentrations (S4_Br_HB, S5_Br_LH and S6_Br_LB). The S3_Br_HH scenario best reproduces observations of Hg^0 for both its concentrations and the diurnal variations. Note that GEOS-Chem uses the low reaction rate constants and predicts BrO levels that are consistent with the "best estimate" values. Our model simulations suggest that the rate constants and the Br concentrations should be in the high bounds in order to reproduce the observed diurnal cycles of Hg^0 at Dome C. This result is in consistency with the speciated mercury measurements and modeling in the free troposphere performed over the eastern United States (Shah et al., 2016). Our model simulations show that the near surface air at Dome C is enriched in Hg^{II}, which has a pronounced diurnal cycle peaking in the afternoon. Thus the deposition of Hg^{II} is also elevated.

Table 4.2. Model scenarios with varying physical and chemical parameters in summer.

Code	Oxidant	k	Conc.	Free troposphere		V_d	Lifetime in surface snow (week)
				Hg^T	Hg^{II}		
S1_O3_HH	O_3	High	High	0.9	0.1	1	2
S2_OH_HH	OH	High	High	0.9	0.1	1	2
S3_Br_HH	Br	High	High	0.9	0.7	1	2
S4_Br_HB	Br	High	Best	0.9	0.5	1	2
S5_Br_LH	Br	Low	High	0.9	0.4	1	2
S6_Br_LB	Br	Low	Best	0.9	0.2	1	2

The unit of free tropospheric Hg concentrations is ng m^{-3}. The unit of V_d is cm s^{-1}. The unit of Hg^{II} deposition flux is ng m^{-2} d^{-1}.

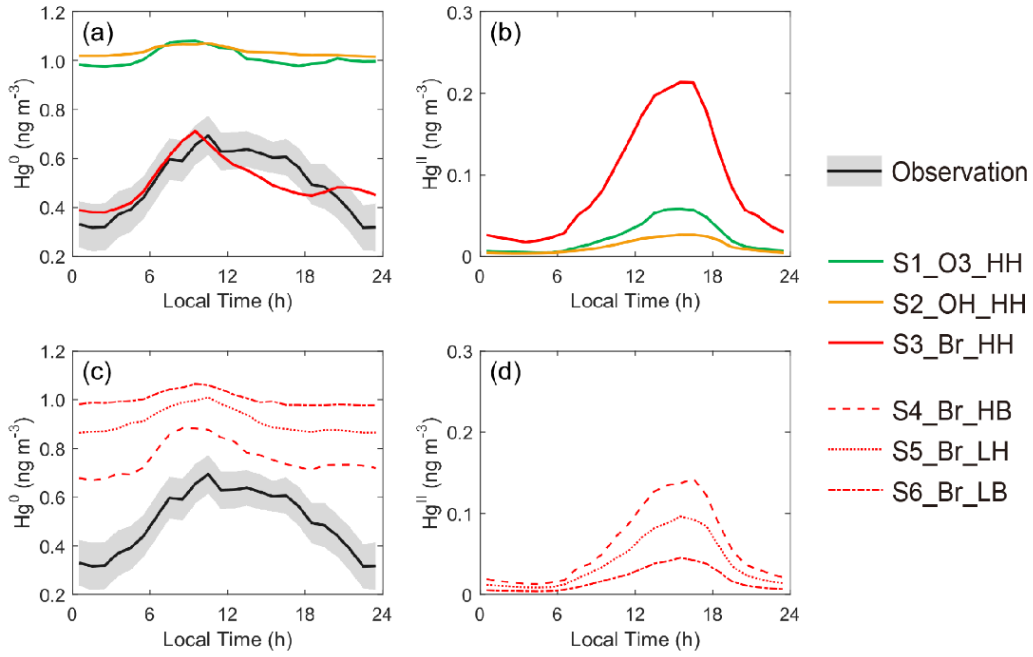

Figure 4.8. Diurnal cycles of speciated mercury concentrations in summer at Dome C. The observation is the averaged Hg^0 from the three inlets at the heights of 0.25, 2.1, and 10 meters above surface, respectively. The shaded region in the observation indicates the 95% confidence interval. The models show the averaged mercury concentrations at the corresponding vertical levels. The two capital letters at the end of each model scenario mean the choice of the oxidant concentration (the former) and the choice of reaction rate constant (the latter). "H" means high, "L" low, and "B" best estimate.

Examples of the averaged vertical and diurnal profiles of the simulated speciated mercury concentrations in the ABL are shown in Figure 4.9. The model scenario S3_Br_HH is shown which best reproduces the observed Hg^0 concentrations. The pronounced diurnal cycle of Hg^0 is confined in the lowest vertical levels in the ABL. The high concentrations of Hg^0 in the lowest levels during the daytime are driven by the ventilation of Hg^0 in the surface snowpack, when the mixed layers are convective and thus the vertical mixing is enhanced. The residual layers are enriched in Hg^{II}, in part due to lack of deposition.

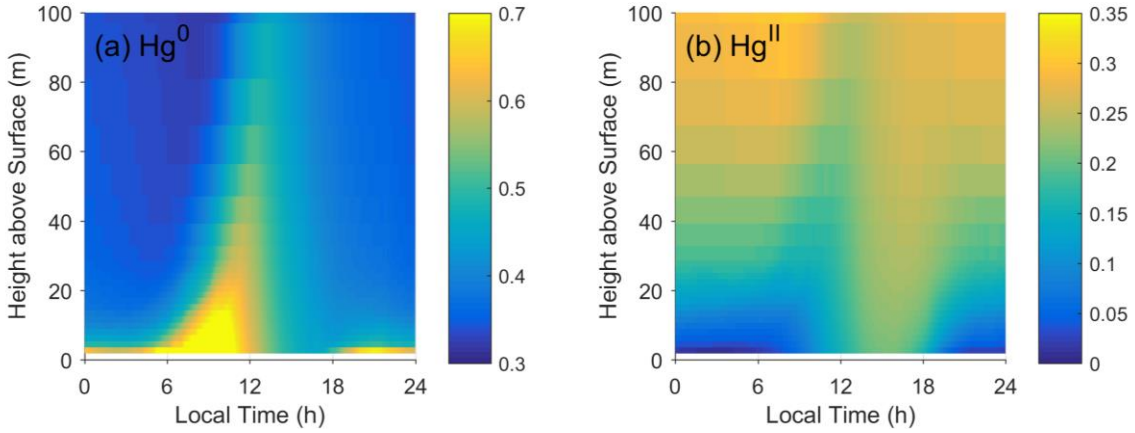

Figure 4.9. Vertical distributions of the simulated speciated mercury concentrations in the ABL. Results from the scenario S3_Br_HH are shown. The unit is ng m^{-3}.

Figure 4.10 shows the diurnal profiles of the modeled mercury fluxes in several scenarios: S1_O3_HH, S2_OH_HH, and S3_Br_HH. The fluxes include Hg^0 oxidation (separated into > 20 m and < 20 m), Hg^{II} deposition onto snow, Hg^{II} photoreduction in surface snow, Hg^0 reemission from snow and the exchange of mercury between the top-most ABL layer and the free troposphere. As shown, the Hg^0 reemission from snow is essentially the same with the Hg^{II} photoreduction in surface snow, which is because most of the mercury in surface snow exists as Hg^{II}. The diurnal profile of the Hg^{II} deposition follows the Hg^{II} concentration in the mixed layers. As described earlier, the S3_Br_HH can best reproduce the observed diurnal profiles of Hg^0 concentration. In this scenario, the surface snow mercury fluxes are much more important than the exchange fluxes with the free troposphere.

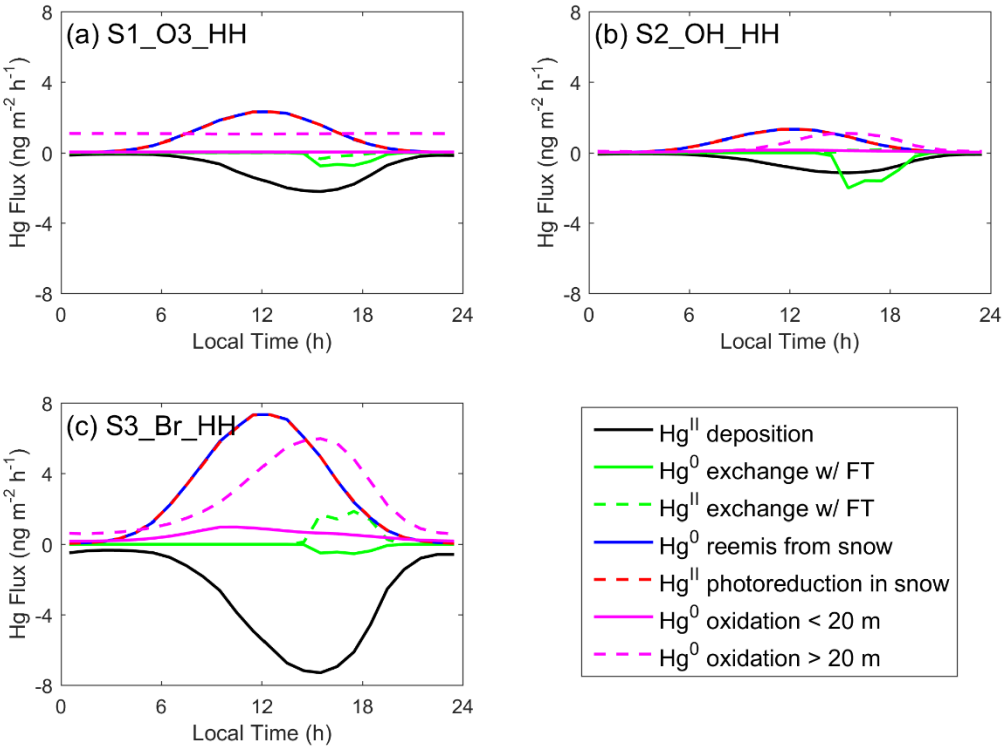

Figure 4.10. Modeled mercury fluxes in different scenarios.

The observations and model simulation results in January and February from S3_Br_HH are shown in Figure 4.11. As the solar radiation fluxes are different in these two months (which affect the concentrations of oxidants and the turbulent diffusion fluxes), we expect the modeled mercury concentrations are also somewhat different. Generally, the diurnal variation of both observed and modeled Hg^0 concentrations are smaller in February, although such difference is insignificant and the shapes of diurnal variations are not the same. It implies that an important task which remains to study is investigating the mercury variabilities in different seasons such as fall and spring.

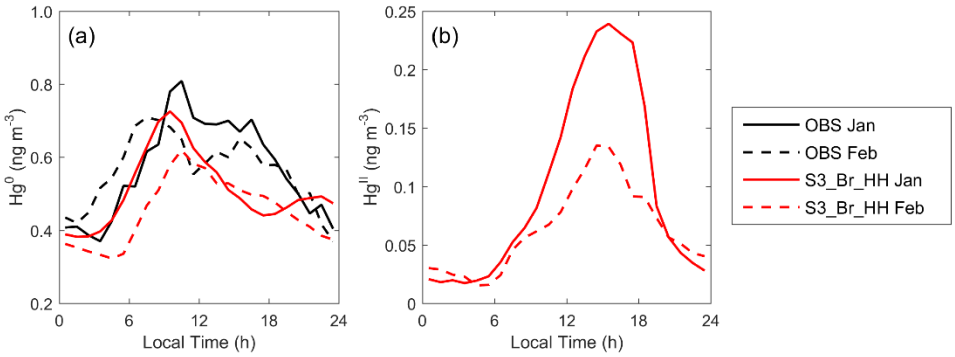

Figure 4.11. Observed and modeled average mercury concentrations in Jan and Feb.

4.2.2 Winter

As described in Section 4.1.1, the mixed layers in winter are extremely shallow (only about 20 m) and do not show diurnal variations. The calculated lifetimes (τ) of Hg^0 for the O_3 and Br oxidation schemes are in the range of 10–10^3 and 10^2–10^3 days, respectively (Figure 4.6). The concentrations of OH in winter are only in the order of 10^3 molec cm^{-3} and thus its role in the oxidation of Hg^0 is negligible. Global mercury models consistently suggest in the lower free troposphere that Hg^{II} concentrations are nearly zero (Figure 4.5).

The observed and simulated diurnal cycles of Hg^0 concentrations in winter are shown in Figure 4.12. In these model scenarios, the free tropospheric Hg^0 and Hg^{II} concentrations are set as 0.9 and 0.0 ng m^{-3}. Due to lack of solar radiation, deposited Hg^{II} onto the snowpack is not reduced into Hg^0. The scenario S1_O3_HH has the highest possible oxidation rates of Hg^0 (τ ~ 10 days) in winter. As expected, both observation and modeling show little diurnal variability. The modeled Hg^0 concentration in the near surface air is very close to the free tropospheric Hg^0 concentration. The difference of the modeled Hg^0 concentration between the no chemistry scenario and S1_O3_HH is also very small (< 0.01 ng m^{-3}). We conclude that the near surface Hg^0 concentration in winter is dominated by the exchange with the free troposphere, but not by the oxidation within the shallow boundary layer.

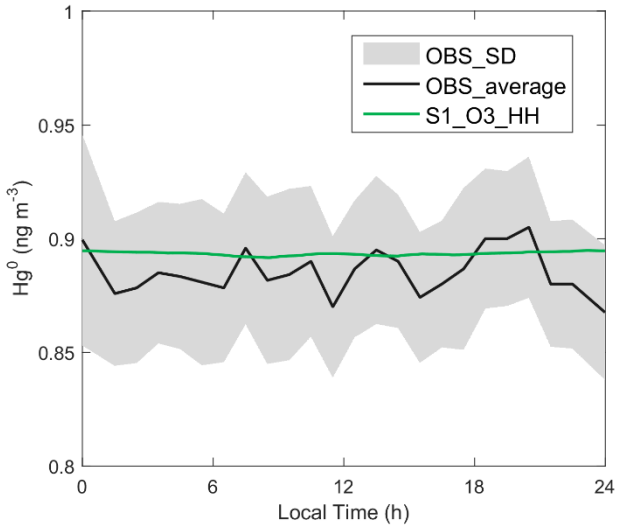

Figure 4.12. Diurnal cycles of mercury concentrations in winter at Dome C. The observation is the averaged Hg^0 from the three inlets at the heights of 0.25, 2.1, and 10 meters above surface, respectively. The shaded region in the observation indicates the 95% confidence interval. The models show the averaged mercury concentrations at the corresponding vertical levels. The two capital letters at the end of each model scenario mean the choice of the oxidant concentration (the former) and the choice of reaction rate constant (the latter). "H" means high, "L" low, and "B" best estimate.

An interesting phenomenon observed at Dome C was that a 20–30% decrease of Hg^0 concentrations occurred during winter (May to mid-Aug). At the same period, Hg^0 levels at the Antarctic coastal stations remained stable (Angot et al., 2016). Several possible mechanisms, including gas phase oxidation by O_3, heterogeneous reactions on the snow surface, and dry deposition of Hg^0, were discussed in Angot et al. (2016). Our mercury modeling suggests that Hg^0 concentrations in the boundary layer are controlled by the free tropospheric conditions. Furthermore, in winter deep convection days occur frequently when the air masses below several hundreds of meters are well mixed and thus mercury levels in the boundary layer and in the lower free troposphere become uniform (Figure 4.13). Therefore, it is very likely that such decrease observed in the boundary layer may occur in the vertical air columns at Dome C. This also implies that surface processes, either heterogeneous reactions on the snow surface or dry deposition of Hg^0, may not be the reason. The decrease of 20–30% from May to mid-Aug corresponds to an *e*-folding time of about 400 days, which falls in the range of the O_3 and Br oxidation schemes as described earlier.

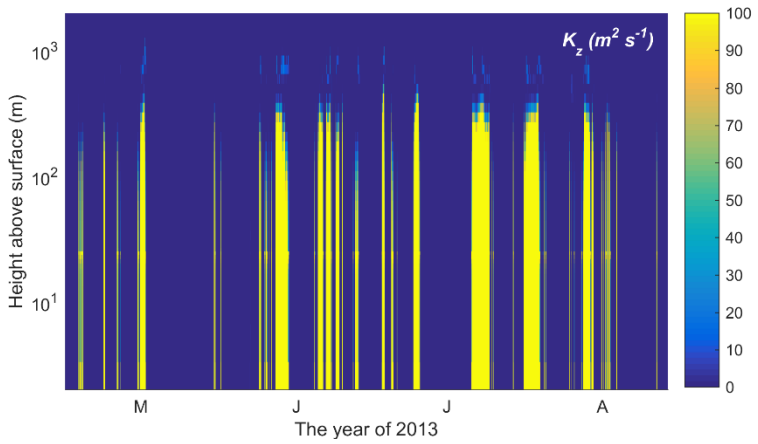

Figure 4.13. Profiles of the vertical turbulent diffusion coefficients during winter.

4.2.3 Sensitivity Analysis

Some parameters and/or processes in our mercury model are not well constrained due to the limitation of our current knowledge on mercury cycling. Therefore, we have performed additional sensitivity simulations. As mentioned above, the best estimate of V_d on the snow surface is 1 cm s^{-1} for Hg^{II}, which is also set as the default value in the model. However, the measured V_d can be as high as 5 cm s^{-1}. We conduct several sensitivity simulations in summer using the V_d of 0.5 cm s^{-1} and 5 cm s^{-1} and the results are shown in Figure 4.14. We find that increasing the value of V_d could enhance the simulated concentrations of Hg^0 and also make the diurnal cycles more pronounced. This is because of the increased deposition of Hg^{II} to and thus the reemission of Hg^0 from the surface snowpack.

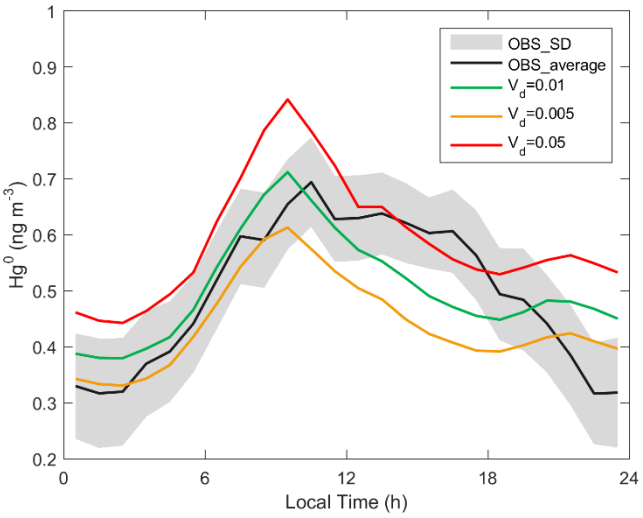

Figure 4.14. Diurnal cycles of simulated mercury concentrations in summer using different Hg^{II} deposition velocities V_d (m s^{-1}). The black curve and the gray shaded region indicate the average observation and its 95% confidence interval.

Another important parameter is the lifetime of surface snow Hg against the photoreduction, which may range from several days to several weeks (Toyota et al., 2014). The model scenarios above assume a lifetime of about 2 weeks according to the study at the South Pole by Brooks et al. (2008). Here we conduct sensitivity simulations by varying the lifetime to 1 week and 3 weeks (see Figure 4.15). A short lifetime could enhance the simulated concentrations of Hg^0 and also make the diurnal cycles more pronounced. However, we find that our conclusion that bromine oxidation is important remains. In addition, the mixing ratios of NO and NO_2 are important model inputs in summer because they significantly affect the concentrations of Br and BrO and the second step oxidation rates of Hg^IBr. It has been suggested that there may be a positive bias in NO_2 measurements and a negative bias in NO measurements thus resulting in too large $[NO_2]/[NO]$ ratios (Frey et al., 2015). Here, we conduct a sensitivity simulation in which the $[NO_2]/[NO]$ ratios are reduced by a factor of 3 (Frey et al., 2015). It is found that assuming a different $[NO_2]/[NO]$ ratio does not significantly affect the simulated Hg^0 concentrations.

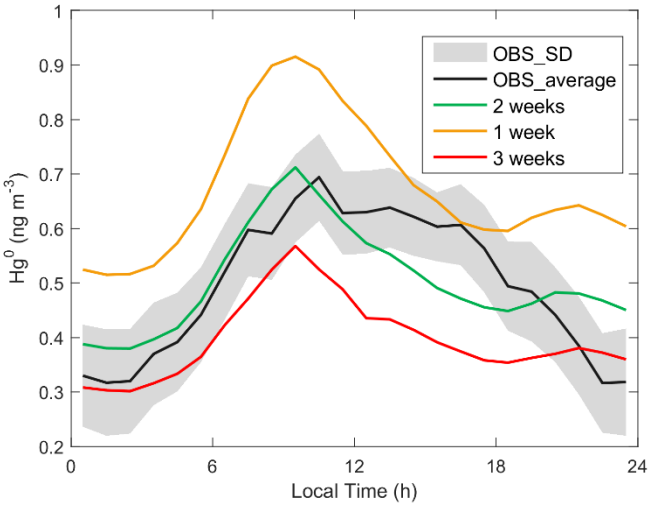

Figure 4.15. Diurnal profiles of simulated mercury concentrations in summer using different lifetime of mercury photoreduction in surface snowpack. The black curve and the gray shaded region indicate the average observation and its 95% confidence interval.

4.2.4 Comparison with Summit, Greenland

Both Dome C, Antarctica (75°06' S, 123°21' E, 3220 m above sea level) and Summit, Greenland (72.6° N, 38.5° W, 3200 m above sea level) are located in the polar plateau regions and far from the ocean (several hundreds of kilometers). As a result, their meteorological and chemical conditions share many similarities. In summer, both stations have shallow ABLs which are stable at night but convective during the daytime (Van Dam et al., 2013). Active bromine chemistry was found to occur (Thomas et al., 2011) and the average BrO mixing ratios were observed to be 0.9 pptv by LP-DOAS and 1.5 pptv by CIMS in summer (Liao et al., 2011; Stutz et al., 2011), compared to its best estimate of 0.4 pptv and the upper limit of 1 pptv at Dome C. Thus, it is expected that these two stations may have similar variabilities of mercury in the boundary layer. Brooks et al. (2011) conducted speciated mercury measurements at Summit in the 2007–2008 summer as part of the collaborative Greenland Summit Halogen-HO_x experiment (GSHOX) campaigns. However, they did not observe the pronounced diurnal cycle of Hg^0 concentrations that peaks at local noon time, as was seen at Dome C. In fact, the diurnal variations of Hg^0 concentrations were hardly discernible. Below we discuss several factors that contribute to the differences observed at these two stations.

First, although the BrO levels at Summit are comparable or may be higher than those at Dome C, the levels of Br at Summit, the primary oxidant of Hg^0, may be lower. As shown in Equation (4.1), the [Br]/[BrO] ratios are positively related to the NO levels and negatively related to the O_3 levels. Measurements have shown that the average summertime NO_x mixing ratio at Summit (~ 20 pptv) is much lower than that at Dome C (~ 300 pptv) (Kramer et al., 2015; Frey et al., 2013). The average summertime O_3 mixing ratio at Summit (~ 50 ppbv) is about the double of that at Dome C (~ 25 ppbv). A back-of-the-envelope calculation shows, assuming the same BrO level, that the mixing ratio of Br at Dome C is on average a factor of 8 higher than that at Summit.

Second, the thermal dissociation of the intermediate Hg^IBr at Summit is an order of magnitude higher than at Dome C as this reaction rate strongly depends on temperature. In addition, the second step oxidation of Hg^IBr by NO_2 is significantly slower at Summit than at Dome C. In fact, at Summit, the second step oxidation and the dissociation of Hg^IBr have comparable reaction rates. This is in contrast with the situation at Dome C where the second step reaction by NO_2 can easily outcompete the dissociation of Hg^IBr.

In summary, we expect from the analysis above that the Br-initiated oxidation should be much slower at Summit than at Dome C, leading to the smaller deposition fluxes of Hg^{II} on the snowpack and also the reemission fluxes of Hg^0. This is consistent with the difference of the measured average total mercury levels in surface snow: 5.6 ng L^{-1} at Summit and 10.4 ng L^{-1} at Dome C, respectively. The measured Hg^{II} concentrations in the near surface air at Summit are also much lower than the levels modeled at Dome C.

4.3 Conclusion

A one-dimensional chemical and transport model has been built and used to simulate the mercury cycles at Dome C on the Antarctic plateau. The model consists of the oxidation of Hg^0, the deposition of Hg^{II} onto snow, the photoreduction of Hg^{II} to Hg^0 in surface snow, and finally the reemission of Hg^0 back into the atmosphere, as well as the exchange of mercury with its free tropospheric pool.

In summer, the oxidation of Hg^0 initiated by bromine ($\tau \sim 1–10$ days) is more efficient than by O_3 and OH ($\tau \sim 10–10^3$ days) in part due to cold temperature and high NO_x levels. Sensitivity simulations suggest that the rate constant of Hg^0 + Br and the mixing ratio of Br should be close to the upper uncertainty bound in order to match the observation. Reemission of Hg^0 from the snowpack is also necessary. The near surface air is modeled to be enriched in Hg^{II}, consistent with the earlier findings (Angot et al., 2016; Brooks et al., 2008).

In winter, the model shows that Hg^0 concentration is dominated by its exchange with the free troposphere, but not by its oxidation in the shallow boundary layer. The slow decrease of Hg^0 concentration during the winter period can be explained by either O_3 or Br initiated oxidation but unlikely due to surface processes.

The reasons why the pronounced diurnal cycles of Hg^0 concentrations were not observed in Summit, Greenland are that the Br-initiated oxidation is much slower, leading to smaller deposition fluxes of Hg^{II} and reemission fluxes of Hg^0. This is consistent with the low total mercury levels in surface snow and the low Hg^{II} concentrations in the near surface air.

As described in the Section 4.2, an important future work is to investigate the mercury variabilities in different seasons such as fall and spring. This can greatly help interpreting the results obtained in the analysis of diurnal variations in summer and winter.

Finally, our model simulations reveal several specific research needs in order to obtain a better understanding of mercury cycling over the Antarctic plateau: (1) measurements of bromine species; (2) measurements of deposition velocities of mercury species; (3) improvement of chemical kinetics and mechanisms; and (4) improvement of physical and chemical processes within the surface snowpack.

Chapter 5 Conclusion

Mercury is a critical environmental concern and understanding its biogeochemical cycling is necessary for evaluating its adverse human health effects and designing effective regulation strategies. Although of great importance in its biogeochemical cycling, the surface fluxes of mercury, either the anthropogenic emission sources or the bi-directional exchange fluxes of Hg^0 at terrestrial and ocean surfaces, are still poorly constrained given current bottom-up approaches. The three research projects presented in this thesis have quantified the surface fluxes of mercury at different spatial scales by combining observations and models.

In the first research project, the global-scale inverse modeling combines ground-based Hg^0 observations and the GEOS-Chem (a 3-dimensional chemical transport model) simulations and obtains a total mercury emission of 5.8 Gg yr^{-1} (an uncertainty range: from 1.7 to 10.3 Gg yr^{-1}). The inversion results show that the ocean is a major source and accounts for 3.2 Gg yr^{-1} (55% of the total), which is generally consistent with bottom-up estimates and assumptions in several other global models. It is concluded that the terrestrial ecosystem is neither a net source nor a net sink of atmospheric Hg^0 on a global scale, in contrast to its bottom-up estimate by Pirrone et al. (2010) as a significant net source. The optimized Asian anthropogenic emissions range from 650-1770 Mg yr^{-1}, suggesting that bottom-up inventories (550-800 Mg yr^{-1}) underestimate their contributions. Several very recent studies and data sets indicate that bottom-up inventories may have missed important emission sectors, underestimated activity levels, and overestimated abatement efficiencies, and thus support our conclusion.

The emission inversion changes seasonal patterns of ocean emissions in both hemispheres. Two ocean model parameters related to the redox chemistry and vertical transport are identified to explain such changes and are then constrained using the inversion approach. Results suggest that dark oxidation of aqueous Hg^0 is more important and less particulate mercury is removed from the ocean mixed layer than previously thought. The parameter changes can affect the simulated global ocean mercury budgets, especially the mass exchange between the mixed layer and subsurface waters. The inversions also suggest changes in the timescales of mercury cycling between different reservoirs. The legacy mercury releases tend to reside in the terrestrial system

rather than in the ocean. In this project, we also find that the uncertain atmospheric mercury chemical mechanisms and the potential large systematic uncertainty of the Hg^0 measurements at different ground-based sites may limit the assessment of mercury surface fluxes.

In the second research project, the GEOS-Chem nested grid mercury model simulations are compared to aircraft observations of Hg^0 over the eastern North America, which provides new insights into the regional atmosphere-surface exchange. Because a consistent instrument system (UW-DOHGS) was used to measure Hg^0 concentrations over both ocean and terrestrial surfaces, the influence of the potential systematic uncertainty of each Hg^0 measurement should be minimal. Different model scenarios are performed and the model-observation comparison suggests that the Northwest Atlantic may be a net source of Hg^0, with high evasion fluxes in summer, whereas the terrestrial ecosystem in the eastern United States is likely a net sink of Hg^0 during summer. These are in consistency with the conclusions in the global-scale inverse modeling. The inferred high Hg^0 emission fluxes from the Northwest Atlantic may be a result of the high wet deposition fluxes of Hg^{II}, which are in turn linked to high precipitation rates in this region. The importance of riverine discharge, currently a missing source in GEOS-Chem, is identified.

The Antarctic plateau is an ideal region to study the mercury exchange at the atmosphere-snow surfaces as it is far from most anthropogenic sources and the terrain is very homogeneous. In the third project, a one-dimensional chemical and transport model of mercury is built and used to simulate the diurnal cycles of mercury at Dome Concordia during the summer and winter seasons, in order to quantitatively explore and identify the most important processes contributing to the mercury variability. Through the comparisons of model simulations and observations, we suggest a rapid mercury cycle occurring in summer on the Antarctic plateau, which includes the rapid oxidation of atmospheric Hg^0 by a bromine initiated scheme, the deposition of Hg^{II} onto snow, the photoreduction of Hg^{II} to Hg^0 in surface snow, and the reemission of Hg^0 back into the air. Several physical and chemical factors, including continuous sunlight, cold temperature, shallow boundary layer, and high NO_x levels at Dome Concordia, favor Hg^0 oxidation by bromine and can also explain why such a diurnal cycle at Dome Concordia were not seen at other locations (e.g., the Summit, Greenland). The exchange between the atmosphere and the snow is rapid and the recycling time for mercury in the surface

snowpack is roughly one week but highly uncertain. Our model shows that little diurnal variation exists in winter due to lack of solar radiation, which is consistent with the observations, and that Hg^0 concentration in the shallow atmospheric boundary layer is largely affected by its exchange with the free troposphere.

These projects in this thesis have also identified several knowledge gaps and research needs in mercury observation and modeling which should be paid attention to in the future.

First, the uncertain Hg^0 concentration measurements have strongly hampered a further understanding of surface exchange fluxes and anthropogenic emissions, as described in our global-scale inverse modeling. Hg^{II} concentration measurements are even more uncertain, and so we cannot include them in our analysis. Therefore, research aimed at quantifying and reducing their measurement uncertainties should be given high priority by the scientific community (Jaffe et al., 2014).

Second, more observational stations are needed and in particular in some regions such as the Southern Hemisphere and the polar areas.

Third, improving our knowledge on atmospheric mercury redox chemistry (both chemical kinetics and actual mechanisms) is crucial at both global and regional scales, which requires a combination of both measurement and model advances.

Bibliography

Agnan, Y., Le Dantec, T., Moore, C. W., Edwards, G. C., and Obrist, D.: New constraints on terrestrial surface–atmosphere fluxes of gaseous elemental mercury using a global database, *Environ Sci Technol*, 50, 507-524, doi:10.1021/acs.est.5b04013, 2016.

AMAP/UNEP: Technical background report for the Global Mercury Assessment 2013, Arctic Monitoring and Assessment Programme, Oslo, Norway/UNEP Chemicals Branch Geneva, Switzerland, 2013.

AMAP/UNEP: Global mercury modelling: Update of modelling results in the Global Mercury Assessment 2013, Arctic Monitoring and Assessment Programme, Oslo, Norway/UNEP Chemicals Branch, Geneva, Switzerland, iv + 32 pp, 2015.

Ambrose, J. L., Gratz, L. E., Jaffe, D. A., Campos, T., Flocke, F. M., Knapp, D. J., Stechman, D. M., Stell, M., Weinheimer, A. J., Cantrell, C. A., and Mauldin, R. L.: Mercury emission ratios from coal-fired power plants in the Southeastern United States during NOMADSS, *Environ Sci Technol*, doi:10.1021/acs.est.5b01755, 2015.

Amos, H. M., Jacob, D. J., Holmes, C. D., Fisher, J. A., Wang, Q., Yantosca, R. M., Corbitt, E. S., Galarneau, E., Rutter, A. P., Gustin, M. S., Steffen, A., Schauer, J. J., Graydon, J. A., St. Louis, V. L., Talbot, R. W., Edgerton, E. S., Zhang, Y., and Sunderland, E. M.: Gas-particle partitioning of atmospheric Hg(II) and its effect on global mercury deposition, *Atmos Chem Phys*, 12, 591-603, doi:10.5194/acp-12-591-2012, 2012.

Amos, H. M., Jacob, D. J., Streets, D. G., and Sunderland, E. M.: Legacy impacts of all-time anthropogenic emissions on the global mercury cycle, *Global Biogeochem Cy*, 27, 410-421, doi:10.1002/gbc.20040, 2013.

Amos, H. M., Jacob, D. J., Kocman, D., Horowitz, H. M., Zhang, Y., Dutkiewicz, S., Horvat, M., Corbitt, E. S., Krabbenhoft, D. P., and Sunderland, E. M.: Global biogeochemical implications of mercury discharges from rivers and sediment burial, *Environ Sci Technol*, 48, 9514-9522, doi:10.1021/es502134t, 2014.

Amyot, M., Gill, G. A., and Morel, F. M. M.: Production and loss of dissolved gaseous mercury in coastal seawater, *Environ Sci Technol*, 31, 3606-3611, doi:10.1021/es9703685, 1997.

Andersson, M. E., Gårdfeldt, K., Wängberg, I., Sprovieri, F., Pirrone, N., and Lindqvist, O.: Seasonal and daily variation of mercury evasion at coastal and off shore sites from the Mediterranean Sea, *Mar Chem*, 104, 214-226, doi:10.1016/j.marchem.2006.11.003, 2007.

Andersson, M. E., Gårdfeldt, K., Wängberg, I., and Strömberg, D.: Determination of Henry's law constant for elemental mercury, *Chemosphere*, 73, 587-592, doi:10.1016/j.chemosphere.2008.05.067, 2008.

Andersson, M. E., Sommar, J., Gårdfeldt, K., and Jutterström, S.: Air–sea exchange of volatile mercury in the North Atlantic Ocean, *Mar Chem*, 125, 1-7, doi:10.1016/j.marchem.2011.01.005, 2011.

Angot, H., Barret, M., Magand, O., Ramonet, M., and Dommergue, A.: A 2-year record of atmospheric mercury species at a background Southern Hemisphere station on Amsterdam Island, *Atmos Chem Phys*, 14, 11461-11473, doi:10.5194/acp-14-11461-2014, 2014.

Angot, H., Magand, O., Helmig, D., Ricaud, P., Quennehen, B., Gallée, H., Del Guasta, M., Sprovieri, F., Pirrone, N., Savarino, J., and Dommergue, A.: New insights into the atmospheric mercury cycling

in central Antarctica and implications on a continental scale, *Atmos Chem Phys*, 16, 8249-8264, doi:10.5194/acp-16-8249-2016, 2016.

Antia, A. N., Koeve, W., Fischer, G., Blanz, T., Schulz-Bull, D., Schölten, J., Neuer, S., Kremling, K., Kuss, J., Peinert, R., Hebbeln, D., Bathmann, U., Conte, M., Fehner, U., and Zeitzschel, B.: Basin-wide particulate carbon flux in the Atlantic Ocean: Regional export patterns and potential for atmospheric CO_2 sequestration, *Global Biogeochem Cy*, 15, 845-862, doi:10.1029/2000gb001376, 2001.

Apel, E. C., Emmons, L. K., Karl, T., Flocke, F., Hills, A. J., Madronich, S., Lee-Taylor, J., Fried, A., Weibring, P., Walega, J., Richter, D., Tie, X., Mauldin, L., Campos, T., Weinheimer, A., Knapp, D., Sive, B., Kleinman, L., Springston, S., Zaveri, R., Ortega, J., Voss, P., Blake, D., Baker, A., Warneke, C., Welsh-Bon, D., de Gouw, J., Zheng, J., Zhang, R., Rudolph, J., Junkermann, W., and Riemer, D. D.: Chemical evolution of volatile organic compounds in the outflow of the Mexico City Metropolitan area, *Atmos Chem Phys*, 10, 2353-2375, doi:10.5194/acp-10-2353-2010, 2010.

Ariya, P. A., Khalizov, A., and Gidas, A.: Reactions of gaseous mercury with atomic and molecular halogens: kinetics, product studies, and atmospheric implications, *J Phys Chem A*, 106, 7310-7320, doi:10.1021/jp020719o, 2002.

Ariya, P. A., Amyot, M., Dastoor, A., Deeds, D., Feinberg, A., Kos, G., Poulain, A., Ryjkov, A., Semeniuk, K., Subir, M., and Toyota, K.: Mercury physicochemical and biogeochemical transformation in the atmosphere and at atmospheric interfaces: A review and future directions, *Chem Rev*, 115, 3760-3802, doi:10.1021/cr500667e, 2015.

Aspmo, K., Gauchard, P.-A., Steffen, A., Temme, C., Berg, T., Bahlmann, E., Banic, C., Dommergue, A., Ebinghaus, R., Ferrari, C., Pirrone, N., Sprovieri, F., and Wibetoe, G.: Measurements of atmospheric mercury species during an international study of mercury depletion events at Ny-Ålesund, Svalbard, spring 2003. How reproducible are our present methods?, *Atmos Environ*, 39, 7607-7619, doi:10.1016/j.atmosenv.2005.07.065, 2005.

Aspmo, K., Temme, C., Berg, T., Ferrari, C., Gauchard, P.-A., Fain, X., and Wibetoe, G.: Mercury in the atmosphere, snow and melt water ponds in the North Atlantic Ocean during Arctic summer, *Environ Sci Technol*, 40, 4083-4089, doi:10.1021/es052117z, 2006.

Bagnato, E., Tamburello, G., Avard, G., Martinez-Cruz, M., Enrico, M., Fu, X., Sprovieri, M., and Sonke, J. E.: Mercury fluxes from volcanic and geothermal sources: an update, *Geological Society, London, Special Publications*, 410, doi:10.1144/sp410.2, 2014.

Baker, D. F., Law, R. M., Gurney, K. R., Rayner, P., Peylin, P., Denning, A. S., Bousquet, P., Bruhwiler, L., Chen, Y. H., Ciais, P., Fung, I. Y., Heimann, M., John, J., Maki, T., Maksyutov, S., Masarie, K., Prather, M., Pak, B., Taguchi, S., and Zhu, Z.: TransCom 3 inversion intercomparison: Impact of transport model errors on the interannual variability of regional CO_2 fluxes, 1988–2003, *Global Biogeochem Cy*, 20, GB1002, doi:10.1029/2004gb002439, 2006.

Balabanov, N. B., Shepler, B. C., and Peterson, K. A.: Accurate global potential energy surface and reaction dynamics for the ground state of $HgBr_2$, *J Phys Chem A*, 109, 8765-8773, doi:10.1021/jp053415l, 2005.

Bash, J. O., and Miller, D. R.: A note on elevated total gaseous mercury concentrations downwind from an agriculture field during tilling, *Sci Total Environ*, 388, 379-388, doi:10.1016/j.scitotenv.2007.07.012, 2007.

Batrakova, N., Travnikov, O., and Rozovskaya, O.: Chemical and physical transformations of mercury in the ocean: a review, *Ocean Sci*, 10, 1047-1063, doi:10.5194/os-10-1047-2014, 2014.

Bey, I., Jacob, D. J., Yantosca, R. M., Logan, J. A., Field, B. D., and Aalto, P. P.: Global modeling of tropospheric chemistry with assimilated meteorology: Model description and evaluation, *J Geophys Res Atmos*, 106, 23073-23095, doi:10.1029/2001jd000807, 2001.

Brooks, S., Arimoto, R., Lindberg, S., and Southworth, G.: Antarctic polar plateau snow surface conversion of deposited oxidized mercury to gaseous elemental mercury with fractional long-term burial, *Atmos Environ*, 42, 2877-2884, doi:10.1016/j.atmosenv.2007.05.029, 2008.

Brooks, S., Moore, C., Lew, D., Lefer, B., Huey, G., and Tanner, D.: Temperature and sunlight controls of mercury oxidation and deposition atop the Greenland ice sheet, *Atmos Chem Phys*, 11, 8295-8306, doi:10.5194/acp-11-8295-2011, 2011.

Brunke, E. G., Labuschagne, C., Ebinghaus, R., Kock, H. H., and Slemr, F.: Gaseous elemental mercury depletion events observed at Cape Point during 2007–2008, *Atmos Chem Phys*, 10, 1121-1131, doi:10.5194/acp-10-1121-2010, 2010.

Brunner, D., Henne, S., Keller, C. A., Reimann, S., Vollmer, M. K., O'Doherty, S., and Maione, M.: An extended Kalman-filter for regional scale inverse emission estimation, *Atmos Chem Phys*, 12, 3455-3478, doi:10.5194/acp-12-3455-2012, 2012.

Buermann, W., Dong, J., Zeng, X., Myneni, R. B., and Dickinson, R. E.: Evaluation of the utility of satellite-based vegetation leaf area index data for climate simulations, *J Climate*, 14, 3536-3550, doi:10.1175/1520-0442(2001)014<3536:eotuos>2.0.co;2, 2001.

Bullock, O. R., Atkinson, D., Braverman, T., Civerolo, K., Dastoor, A., Davignon, D., Ku, J.-Y., Lohman, K., Myers, T. C., Park, R. J., Seigneur, C., Selin, N. E., Sistla, G., and Vijayaraghavan, K.: The North American Mercury Model Intercomparison Study (NAMMIS): Study description and model-to-model comparisons, *J Geophys Res Atmos*, 113, D17310, doi:10.1029/2008jd009803, 2008.

Bullock, O. R., Atkinson, D., Braverman, T., Civerolo, K., Dastoor, A., Davignon, D., Ku, J.-Y., Lohman, K., Myers, T. C., Park, R. J., Seigneur, C., Selin, N. E., Sistla, G., and Vijayaraghavan, K.: An analysis of simulated wet deposition of mercury from the North American Mercury Model Intercomparison Study, *J Geophys Res Atmos*, 114, D08301, doi:10.1029/2008jd011224, 2009.

Carlton, A. G., de Gouw, J., Jimenez, J. L., Guenther, A., Cohen, R. C., Brown, S., Warneke, C., Jaffe, D. A., Wennberg, P. O., Turpin, B. J., Goldstein, A. H., Surratt, J., Brock, C., Nenes, A., Ambrose, J. L., Baker, K. R., Edgerton, S., Farkas, C., Farmer, D., Gratz, L., Hunt, S., Jaeglé, L., Mak, J., McClure, C., Murphy, D., Nauyen, T. K., Pirece, J. R., Selin, N. E., Shaw, S., Shah, V., Shepson, P. B., Song, S., Stutz, J., Trainer, M., Washenfelder, R. A., and Zhou, X.: The Southeast Atmosphere Studies (SAS): Coordinated investigation and discovery to answer critical questions about fundamental atmospheric processes, *to be submitted to Bull Amer Meteor Soc*, 2016.

Chen, H. S., Wang, Z. F., Li, J., Tang, X., Ge, B. Z., Wu, X. L., Wild, O., and Carmichael, G. R.: GNAQPMS-Hg v1.0, a global nested atmospheric mercury transport model: model description, evaluation and application to trans-boundary transport of Chinese anthropogenic emissions, *Geosci Model Dev*, 8, 2857-2876, doi:10.5194/gmd-8-2857-2015, 2015.

Chen, Y.-H., and Prinn, R. G.: Estimation of atmospheric methane emissions between 1996 and 2001 using a three-dimensional global chemical transport model, *J Geophys Res*, 111, D10307, doi:10.1029/2005jd006058, 2006.

Cheng, I., Zhang, L., Mao, H., Blanchard, P., Tordon, R., and Dalziel, J.: Seasonal and diurnal patterns of speciated atmospheric mercury at a coastal-rural and a coastal-urban site, *Atmos Environ*, 82, 193-205, doi:10.1016/j.atmosenv.2013.10.016, 2014.

Choi, H.-D., and Holsen, T. M.: Gaseous mercury fluxes from the forest floor of the Adirondacks, *Environ Pollut*, 157, 592-600, doi:10.1016/j.envpol.2008.08.020, 2009.

Ci, Z., Zhang, X., and Wang, Z.: Elemental mercury in coastal seawater of Yellow Sea, China: Temporal variation and air–sea exchange, *Atmos Environ*, 45, 183-190, doi:10.1016/j.atmosenv.2010.09.025, 2011.

Cohen, M. D., Draxler, R. R., Artz, R. S., Blanchard, P., Gustin, M. S., Han, Y.-J., Holsen, T. M., Jaffe, D. A., Kelley, P., and Lei, H.: Modeling the global atmospheric transport and deposition of mercury to the Great Lakes, *Elementa: Science of the Anthropocene*, 4, 000118, doi:10.12952/journal.elementa.000118, 2016.

Cole, A., Steffen, A., Eckley, C., Narayan, J., Pilote, M., Tordon, R., Graydon, J., St. Louis, V., Xu, X., and Branfireun, B.: A survey of mercury in air and precipitation across Canada: Patterns and trends, *Atmosphere*, 5, 635, doi:10.3390/atmos5030635, 2014.

Cole, A. S., Steffen, A., Pfaffhuber, K. A., Berg, T., Pilote, M., Poissant, L., Tordon, R., and Hung, H.: Ten-year trends of atmospheric mercury in the high Arctic compared to Canadian sub-Arctic and mid-latitude sites, *Atmos Chem Phys*, 13, 1535-1545, doi:10.5194/acp-13-1535-2013, 2013.

Converse, A. D., Riscassi, A. L., and Scanlon, T. M.: Seasonal variability in gaseous mercury fluxes measured in a high-elevation meadow, *Atmos Environ*, 44, 2176-2185, doi:10.1016/j.atmosenv.2010.03.024, 2010.

Cossa, D., Heimbürger, L.-E., Lannuzel, D., Rintoul, S. R., Butler, E. C. V., Bowie, A. R., Averty, B., Watson, R. J., and Remenyi, T.: Mercury in the Southern Ocean, *Geochim Cosmochim Ac*, 75, 4037-4052, doi:10.1016/j.gca.2011.05.001, 2011.

Cui, L., Feng, X., Lin, C.-J., Wang, X., Meng, B., Wang, X., and Wang, H.: Accumulation and translocation of 198Hg in four crop species, *Environ Toxicol Chem*, 33, 334-340, doi:10.1002/etc.2443, 2014.

Dastoor, A., Ryzhkov, A., Durnford, D., Lehnherr, I., Steffen, A., and Morrison, H.: Atmospheric mercury in the Canadian Arctic. Part II: Insight from modeling, *Sci Total Environ*, 509–510, 16-27, doi:10.1016/j.scitotenv.2014.10.112, 2015.

Dastoor, A. P., and Durnford, D. A.: Arctic Ocean: Is it a sink or a source of atmospheric mercury?, *Environ Sci Technol*, doi:10.1021/es404473e, 2013.

de Foy, B., Wiedinmyer, C., and Schauer, J. J.: Estimation of mercury emissions from forest fires, lakes, regional and local sources using measurements in Milwaukee and an inverse method, *Atmos Chem Phys*, 12, 8993-9011, doi:10.5194/acp-12-8993-2012, 2012.

de Foy, B., Tong, Y., Yin, X., Zhang, W., Kang, S., Zhang, Q., Zhang, G., Wang, X., and Schauer, J. J.: First field-based atmospheric observation of the reduction of reactive mercury driven by sunlight, *Atmos Environ*, 134, 27-39, doi:10.1016/j.atmosenv.2016.03.028, 2016.

De Simone, F., Gencarelli, C. N., Hedgecock, I. M., and Pirrone, N.: Global atmospheric cycle of mercury: a model study on the impact of oxidation mechanisms, *Environ Sci Pollut Res*, 21, 4110-4123, doi:10.1007/s11356-013-2451-x, 2014.

Demers, J. D., Blum, J. D., and Zak, D. R.: Mercury isotopes in a forested ecosystem: Implications for air-surface exchange dynamics and the global mercury cycle, *Global Biogeochem Cy*, 27, 222-238, doi:10.1002/gbc.20021, 2013.

Denkenberger, J. S., Driscoll, C. T., Branfireun, B. A., Eckley, C. S., Cohen, M., and Selvendiran, P.: A synthesis of rates and controls on elemental mercury evasion in the Great Lakes Basin, *Environ Pollut*, 161, 291-298, doi:10.1016/j.envpol.2011.06.007, 2012.

Dibble, T. S., Zelie, M. J., and Mao, H.: Thermodynamics of reactions of ClHg and BrHg radicals with atmospherically abundant free radicals, *Atmos Chem Phys*, 12, 10271-10279, doi:10.5194/acp-12-10271-2012, 2012.

Dommergue, A., Ferrari, C. P., Poissant, L., Gauchard, P.-A., and Boutron, C. F.: Diurnal cycles of gaseous mercury within the snowpack at Kuujjuarapik/Whapmagoostui, Québec, Canada, *Environ Sci Technol*, 37, 3289-3297, doi:10.1021/es026242b, 2003.

Dommergue, A., Sprovieri, F., Pirrone, N., Ebinghaus, R., Brooks, S., Courteaud, J., and Ferrari, C. P.: Overview of mercury measurements in the Antarctic troposphere, *Atmos Chem Phys*, 10, 3309-3319, doi:10.5194/acp-10-3309-2010, 2010.

Dommergue, A., Barret, M., Courteaud, J., Cristofanelli, P., Ferrari, C. P., and Gallée, H.: Dynamic recycling of gaseous elemental mercury in the boundary layer of the Antarctic Plateau, *Atmos Chem Phys*, 12, 11027-11036, doi:10.5194/acp-12-11027-2012, 2012.

Donohoue, D. L., Bauer, D., and Hynes, A. J.: Temperature and pressure dependent rate coefficients for the reaction of Hg with Cl and the reaction of Cl with Cl: A pulsed laser photolysis−pulsed laser induced fluorescence study, *J Phys Chem A*, 109, 7732-7741, doi:10.1021/jp051354l, 2005.

Donohoue, D. L., Bauer, D., Cossairt, B., and Hynes, A. J.: Temperature and pressure dependent rate coefficients for the reaction of Hg with Br and the reaction of Br with Br: A pulsed laser photolysis-pulsed laser induced fluorescence study, *J Phys Chem A*, 110, 6623-6632, doi:10.1021/jp054688j, 2006.

Driscoll, C. T., Mason, R. P., Chan, H. M., Jacob, D. J., and Pirrone, N.: Mercury as a global pollutant: sources, pathways, and effects, *Environ Sci Technol*, 47, 4967-4983, doi:10.1021/es305071v, 2013.

Drummond, M. A., and Loveland, T. R.: Land-use pressure and a transition to forest-cover loss in the Eastern United States, *BioScience*, 60, 286-298, doi:10.1525/bio.2010.60.4.7, 2010.

Durnford, D., Dastoor, A., Figueras-Nieto, D., and Ryjkov, A.: Long range transport of mercury to the Arctic and across Canada, *Atmos Chem Phys*, 10, 6063-6086, doi:10.5194/acp-10-6063-2010, 2010.

Durnford, D., Dastoor, A., Ryzhkov, A., Poissant, L., Pilote, M., and Figueras-Nieto, D.: How relevant is the deposition of mercury onto snowpacks? – Part 2: A modeling study, *Atmos Chem Phys*, 12, 9251-9274, doi:10.5194/acp-12-9251-2012, 2012.

Ebinghaus, R., Jennings, S. G., Schroeder, W. H., Berg, T., Donaghy, T., Guentzel, J., Kenny, C., Kock, H. H., Kvietkus, K., Landing, W., Mühleck, T., Munthe, J., Prestbo, E. M., Schneeberger, D., Slemr, F., Sommar, J., Urba, A., Wallschläger, D., and Xiao, Z.: International field intercomparison measurements of atmospheric mercury species at Mace Head, Ireland, *Atmos Environ*, 33, 3063-3073, doi:10.1016/S1352-2310(98)00119-8, 1999.

Ebinghaus, R., Jennings, S. G., Kock, H. H., Derwent, R. G., Manning, A. J., and Spain, T. G.: Decreasing trends in total gaseous mercury observations in baseline air at Mace Head, Ireland from 1996 to 2009, *Atmos Environ*, 45, 3475-3480, doi:10.1016/j.atmosenv.2011.01.033, 2011.

Edwards, G. C., and Howard, D. A.: Air-surface exchange measurements of gaseous elemental mercury over naturally enriched and background terrestrial landscapes in Australia, *Atmos Chem Phys*, 13, 5325-5336, doi:10.5194/acp-13-5325-2013, 2013.

Ericksen, J. A., Gustin, M. S., Xin, M., Weisberg, P. J., and Fernandez, G. C. J.: Air–soil exchange of mercury from background soils in the United States, *Sci Total Environ*, 366, 851-863, doi:10.1016/j.scitotenv.2005.08.019, 2006.

Faïn, X., Ferrari, C. P., Dommergue, A., Albert, M., Battle, M., Arnaud, L., Barnola, J. M., Cairns, W., Barbante, C., and Boutron, C.: Mercury in the snow and firn at Summit Station, Central Greenland, and implications for the study of past atmospheric mercury levels, *Atmos Chem Phys*, 8, 3441-3457, doi:10.5194/acp-8-3441-2008, 2008.

Fay, L., and Gustin, M.: Assessing the influence of different atmospheric and soil mercury concentrations on foliar mercury concentrations in a controlled environment, *Water Air Soil Pollut*, 181, 373-384, doi:10.1007/s11270-006-9308-6, 2007.

Fisher, J. A., Jacob, D. J., Soerensen, A. L., Amos, H. M., Steffen, A., and Sunderland, E. M.: Riverine source of Arctic Ocean mercury inferred from atmospheric observations, *Nat Geosci*, 5, 499-504, doi:10.1038/ngeo1478, 2012.

Fitzgerald, W. F., Lamborg, C. H., and Hammerschmidt, C. R.: Marine biogeochemical cycling of mercury, *Chem Rev*, 107, 641-662, doi:10.1021/cr050353m, 2007.

France, J. L., King, M. D., Frey, M. M., Erbland, J., Picard, G., Preunkert, S., MacArthur, A., and Savarino, J.: Snow optical properties at Dome C (Concordia), Antarctica; implications for snow emissions and snow chemistry of reactive nitrogen, *Atmos Chem Phys*, 11, 9787-9801, doi:10.5194/acp-11-9787-2011, 2011.

Frey, M. M., Brough, N., France, J. L., Anderson, P. S., Traulle, O., King, M. D., Jones, A. E., Wolff, E. W., and Savarino, J.: The diurnal variability of atmospheric nitrogen oxides (NO and NO_2) above the Antarctic Plateau driven by atmospheric stability and snow emissions, *Atmos Chem Phys*, 13, 3045-3062, doi:10.5194/acp-13-3045-2013, 2013.

Frey, M. M., Roscoe, H. K., Kukui, A., Savarino, J., France, J. L., King, M. D., Legrand, M., and Preunkert, S.: Atmospheric nitrogen oxides (NO and NO_2) at Dome C, East Antarctica, during the OPALE campaign, *Atmos Chem Phys*, 15, 7859-7875, doi:10.5194/acp-15-7859-2015, 2015.

Friedli, H. R., Arellano, A. F., Cinnirella, S., and Pirrone, N.: Initial estimates of mercury emissions to the atmosphere from global biomass burning, *Environ Sci Technol*, 43, 3507-3513, doi:10.1021/es802703g, 2009.

Fu, X. W., Feng, X., Dong, Z. Q., Yin, R. S., Wang, J. X., Yang, Z. R., and Zhang, H.: Atmospheric gaseous elemental mercury (GEM) concentrations and mercury depositions at a high-altitude mountain peak in south China, *Atmos Chem Phys*, 10, 2425-2437, doi:10.5194/acp-10-2425-2010, 2010.

Fu, X. W., Feng, X., Liang, P., Deliger, Zhang, H., Ji, J., and Liu, P.: Temporal trend and sources of speciated atmospheric mercury at Waliguan GAW station, Northwestern China, *Atmos Chem Phys*, 12, 1951-1964, doi:10.5194/acp-12-1951-2012, 2012a.

Fu, X. W., Feng, X., Shang, L. H., Wang, S. F., and Zhang, H.: Two years of measurements of atmospheric total gaseous mercury (TGM) at a remote site in Mt. Changbai area, Northeastern China, *Atmos Chem Phys*, 12, 4215-4226, doi:10.5194/acp-12-4215-2012, 2012b.

Fu, X. W., Zhang, H., Lin, C. J., Feng, X. B., Zhou, L. X., and Fang, S. X.: Correlation slopes of GEM / CO, GEM / CO_2, and GEM / CH_4 and estimated mercury emissions in China, South Asia, the Indochinese Peninsula, and Central Asia derived from observations in northwestern and southwestern China, *Atmos Chem Phys*, 15, 1013-1028, doi:10.5194/acp-15-1013-2015, 2015.

Gallée, H., and Schayes, G.: Development of a three-dimensional meso-γ primitive equation model: katabatic winds simulation in the area of Terra Nova Bay, Antarctica, *Mon Wea Rev*, 122, 671-685, doi:10.1175/1520-0493(1994)122<0671:DOATDM>2.0.CO;2, 1994.

Gallée, H., and Gorodetskaya, I.: Validation of a limited area model over Dome C, Antarctic Plateau, during winter, *Clim Dyn*, 34, 61-72, doi:10.1007/s00382-008-0499-y, 2010.

Gallée, H., Preunkert, S., Argentini, S., Frey, M. M., Genthon, C., Jourdain, B., Pietroni, I., Casasanta, G., Barral, H., Vignon, E., Amory, C., and Legrand, M.: Characterization of the boundary layer at Dome C (East Antarctica) during the OPALE summer campaign, *Atmos Chem Phys*, 15, 6225-6236, doi:10.5194/acp-15-6225-2015, 2015.

Gårdfeldt, K., and Jonsson, M.: Is bimolecular reduction of Hg(II) complexes possible in aqueous systems of environmental importance, *J Phys Chem A*, 107, 4478-4482, doi:10.1021/jp0275342, 2003.

Gårdfeldt, K., Sommar, J., Ferrara, R., Ceccarini, C., Lanzillotta, E., Munthe, J., Wängberg, I., Lindqvist, O., Pirrone, N., Sprovieri, F., Pesenti, E., and Strömberg, D.: Evasion of mercury from coastal and open waters of the Atlantic Ocean and the Mediterranean Sea, *Atmos Environ*, 37, Supplement 1, 73-84, doi:10.1016/S1352-2310(03)00238-3, 2003.

Gay, D. A., Schmeltz, D., Prestbo, E., Olson, M., Sharac, T., and Tordon, R.: The Atmospheric Mercury Network: Measurement and initial examination of an ongoing atmospheric mercury record across North America, *Atmos Chem Phys*, 13, 11339-11349, doi:10.5194/acp-13-11339-2013, 2013.

Giang, A., and Selin, N. E.: Benefits of mercury controls for the United States, *P Natl Acad Sci*, 113, 286-291, doi:10.1073/pnas.1514395113, 2016.

Goodsite, M. E., Plane, J. M. C., and Skov, H.: A theoretical study of the oxidation of Hg^0 to $HgBr_2$ in the troposphere, *Environ Sci Technol*, 38, 1772-1776, doi:10.1021/Es034680s, 2004.

Goodsite, M. E., Plane, J. M. C., and Skov, H.: Correction to a theoretical study of the oxidation of Hg0 to HgBr2 in the troposphere, *Environ Sci Technol*, 46, 5262-5262, doi:10.1021/es301201c, 2012.

Grant, S. L., Kim, M., Lin, P., Crist, K. C., Ghosh, S., and Kotamarthi, V. R.: A simulation study of atmospheric mercury and its deposition in the Great Lakes, *Atmos Environ*, 94, 164-172, doi:10.1016/j.atmosenv.2014.05.033, 2014.

Gratz et al.: Airborne observations of mercury emissions from the Chicago/Gary urban/industrial area during the 2013 NOMADSS campaign, *submitted to Atmos Environ*, 2016.

Gratz, L. E., Ambrose, J. L., Jaffe, D. A., Shah, V., Jaeglé, L., Stutz, J., Festa, J., Spolaor, M., Tsai, C., Selin, N. E., Song, S., Zhou, X., Weinheimer, A. J., Knapp, D. J., Montzka, D. D., Flocke, F. M., Campos, T. L., Apel, E., Hornbrook, R., Blake, N. J., Hall, S., Tyndall, G. S., Reeves, M., Stechman, D., and Stell, M.: Oxidation of mercury by bromine in the subtropical Pacific free troposphere, *Geophys Res Lett*, 42, 10494-10502, doi:10.1002/2015GL066645, 2015.

Graydon, J. A., St. Louis, V. L., Hintelmann, H., Lindberg, S. E., Sandilands, K. A., Rudd, J. W. M., Kelly, C. A., Hall, B. D., and Mowat, L. D.: Long-term wet and dry deposition of total and methyl mercury in the remote boreal ecoregion of Canada, *Environ Sci Technol*, 42, 8345-8351, doi:10.1021/es801056j, 2008.

Gurney, K. R., Law, R. M., Denning, A. S., Rayner, P. J., Baker, D., Bousquet, P., Bruhwiler, L., Chen, Y.-H., Ciais, P., Fan, S., Fung, I. Y., Gloor, M., Heimann, M., Higuchi, K., John, J., Maki, T., Maksyutov, S., Masarie, K., Peylin, P., Prather, M., Pak, B. C., Randerson, J., Sarmiento, J., Taguchi, S., Takahashi, T., and Yuen, C.-W.: Towards robust regional estimates of CO_2 sources and sinks using atmospheric transport models, *Nature*, 415, 626-630, doi:10.1038/415626a, 2002.

Gustin, M. S., Lindberg, S. E., and Weisberg, P. J.: An update on the natural sources and sinks of atmospheric mercury, *Appl Geochem*, 23, 482-493, doi:10.1016/j.apgeochem.2007.12.010, 2008.

Gustin, M. S., Huang, J., Miller, M. B., Peterson, C., Jaffe, D. A., Ambrose, J., Finley, B. D., Lyman, S. N., Call, K., Talbot, R., Feddersen, D., Mao, H., and Lindberg, S. E.: Do we understand what the mercury speciation instruments are actually measuring? Results of RAMIX, *Environ Sci Technol*, 47, 7295-7306, doi:10.1021/es3039104, 2013.

Hall, B.: The Gas Phase Oxidation of Elemental Mercury by Ozone, in: Mercury as a Global Pollutant: Proceedings of the Third International Conference held in Whistler, British Columbia, July 10–14, 1994, edited by: Porcella, D. B., Huckabee, J. W., and Wheatley, B., Springer Netherlands, Dordrecht, 301-315, 1995.

Hammerschmidt, C. R., and Bowman, K. L.: Vertical methylmercury distribution in the subtropical North Pacific Ocean, *Mar Chem*, 132–133, 77-82, doi:10.1016/j.marchem.2012.02.005, 2012.

Helmig, D., Johnson, B., Oltmans, S. J., Neff, W., Eisele, F., and Davis, D. D.: Elevated ozone in the boundary layer at South Pole, *Atmos Environ*, 42, 2788-2803, doi:10.1016/j.atmosenv.2006.12.032, 2008.

Henson, S. A., Sanders, R., Madsen, E., Morris, P. J., Le Moigne, F., and Quartly, G. D.: A reduced estimate of the strength of the ocean's biological carbon pump, *Geophys Res Lett*, 38, L04606, doi:10.1029/2011gl046735, 2011.

Holmes, C. D., Jacob, D. J., and Yang, X.: Global lifetime of elemental mercury against oxidation by atomic bromine in the free troposphere, *Geophys Res Lett*, 33, L20808, doi:10.1029/2006gl027176, 2006.

Holmes, C. D., Jacob, D. J., Corbitt, E. S., Mao, J., Yang, X., Talbot, R., and Slemr, F.: Global atmospheric model for mercury including oxidation by bromine atoms, *Atmos Chem Phys*, 10, 12037-12057, doi:10.5194/acp-10-12037-2010, 2010.

Horowitz, H. M., Jacob, D. J., Amos, H. M., Streets, D. G., and Sunderland, E. M.: Historical mercury releases from commercial products: global environmental implications, *Environ Sci Technol*, doi:10.1021/es501337j, 2014.

Huang, J., Golombek, A., Prinn, R., Weiss, R., Fraser, P., Simmonds, P., Dlugokencky, E. J., Hall, B., Elkins, J., Steele, P., Langenfelds, R., Krummel, P., Dutton, G., and Porter, L.: Estimation of regional emissions of nitrous oxide from 1997 to 2005 using multinetwork measurements, a chemical transport model, and an inverse method, *J Geophys Res Atmos*, 113, D17313, doi:10.1029/2007jd009381, 2008.

Hui, M., Zhang, L., Wang, Z., and Wang, S.: The mercury mass flow and emissions of coal-fired power plants in China, *China Environmental Science*, 35, 2241-2250, 2015.

Hynes, A., Donohoue, D., Goodsite, M., and Hedgecock, I.: Our current understanding of major chemical and physical processes affecting mercury dynamics in the atmosphere and at the air-water/terrestrial interfaces, in: Mercury Fate and Transport in the Global Atmosphere, edited by: Mason, R., and Pirrone, N., Springer US, 427-457, 2009.

Iverfeldt, Å., and Lindqvist, O.: Atmospheric oxidation of elemental mercury by ozone in the aqueous phase, *Atmos Environ (1967)*, 20, 1567-1573, doi:10.1016/0004-6981(86)90245-3, 1986.

Jacob, D. J., and Wofsy, S. C.: Photochemistry of biogenic emissions over the Amazon forest, *J Geophys Res Atmos*, 93, 1477-1486, doi:10.1029/JD093iD02p01477, 1988.

Jaffe, D., Prestbo, E., Swartzendruber, P., Weiss-Penzias, P., Kato, S., Takami, A., Hatakeyama, S., and Kajii, Y.: Export of atmospheric mercury from Asia, *Atmos Environ*, 39, 3029-3038, doi:10.1016/j.atmosenv.2005.01.030, 2005.

Jaffe, D. A., Lyman, S., Amos, H. M., Gustin, M. S., Huang, J., Selin, N. E., Levin, L., ter Schure, A., Mason, R. P., Talbot, R., Rutter, A., Finley, B., Jaeglé, L., Shah, V., McClure, C., Ambrose, J., Gratz, L., Lindberg, S., Weiss-Penzias, P., Sheu, G.-R., Feddersen, D., Horvat, M., Dastoor, A., Hynes, A. J., Mao, H., Sonke, J. E., Slemr, F., Fisher, J. A., Ebinghaus, R., Zhang, Y., and Edwards, G.: Progress on understanding atmospheric mercury hampered by uncertain measurements, *Environ Sci Technol*, 48, 7204-7206, doi:10.1021/es5026432, 2014.

Jung, G., Hedgecock, I. M., and Pirrone, N.: ECHMERIT V1.0 – a new global fully coupled mercury-chemistry and transport model, *Geosci Model Dev*, 2, 175-195, doi:10.5194/gmd-2-175-2009, 2009.

Kentisbeer, J., Leeson, S. R., Malcolm, H. M., Leith, I. D., Braban, C. F., and Cape, J. N.: Patterns and source analysis for atmospheric mercury at Auchencorth Moss, Scotland, *Env Sci Process Impact*, doi:10.1039/c3em00700f, 2014.

Khalizov, A. F., Viswanathan, B., Larregaray, P., and Ariya, P. A.: A theoretical study on the reactions of Hg with halogens: atmospheric implications, *J Phys Chem A*, 107, 6360-6365, doi:10.1021/jp0350722, 2003.

Kikuchi, T., Ikemoto, H., Takahashi, K., Hasome, H., and Ueda, H.: Parameterizing soil emission and atmospheric oxidation-reduction in a model of the global biogeochemical cycle of mercury, *Environ Sci Technol*, 47, 12266-12274, doi:10.1021/es401105h, 2013.

Kim, P. S., Jacob, D. J., Fisher, J. A., Travis, K., Yu, K., Zhu, L., Yantosca, R. M., Sulprizio, M. P., Jimenez, J. L., Campuzano-Jost, P., Froyd, K. D., Liao, J., Hair, J. W., Fenn, M. A., Butler, C. F., Wagner, N. L., Gordon, T. D., Welti, A., Wennberg, P. O., Crounse, J. D., St. Clair, J. M., Teng, A. P., Millet, D. B., Schwarz, J. P., Markovic, M. Z., and Perring, A. E.: Sources, seasonality, and trends of southeast US aerosol: an integrated analysis of surface, aircraft, and satellite observations with the GEOS-Chem chemical transport model, *Atmos Chem Phys*, 15, 10411-10433, doi:10.5194/acp-15-10411-2015, 2015.

Kocman, D., Horvat, M., Pirrone, N., and Cinnirella, S.: Contribution of contaminated sites to the global mercury budget, *Environ Res*, 125, 160-170, doi:10.1016/j.envres.2012.12.011, 2013.

Kramer, L. J., Helmig, D., Burkhart, J. F., Stohl, A., Oltmans, S., and Honrath, R. E.: Seasonal variability of atmospheric nitrogen oxides and non-methane hydrocarbons at the GEOSummit station, Greenland, *Atmos Chem Phys*, 15, 6827-6849, doi:10.5194/acp-15-6827-2015, 2015.

Kuiken, T., Zhang, H., Gustin, M., and Lindberg, S.: Mercury emission from terrestrial background surfaces in the eastern USA. Part I: Air/surface exchange of mercury within a southeastern deciduous forest (Tennessee) over one year, *Appl Geochem*, 23, 345-355, doi:10.1016/j.apgeochem.2007.12.006, 2008.

Kukui, A., Legrand, M., Preunkert, S., Frey, M. M., Loisil, R., Gil Roca, J., Jourdain, B., King, M. D., France, J. L., and Ancellet, G.: Measurements of OH and RO_2 radicals at Dome C, East Antarctica, *Atmos Chem Phys*, 14, 12373-12392, doi:10.5194/acp-14-12373-2014, 2014.

Kuss, J., Holzmann, J., and Ludwig, R.: An elemental mercury diffusion coefficient for natural waters determined by molecular dynamics simulation, *Environ Sci Technol*, 43, 3183-3186, doi:10.1021/es8034889, 2009.

Kuss, J., Zülicke, C., Pohl, C., and Schneider, B.: Atlantic mercury emission determined from continuous analysis of the elemental mercury sea-air concentration difference within transects between 50°N and 50°S, *Global Biogeochem Cy*, 25, GB3021, doi:10.1029/2010gb003998, 2011.

Kuss, J.: Water–air gas exchange of elemental mercury: An experimentally determined mercury diffusion coefficient for Hg^0 water–air flux calculations, *Limnol Oceanogr*, 59, 1461-1467, doi:10.4319/lo.2014.59.5.1461, 2014.

Lalonde, J. D., Amyot, M., Kraepiel, A. M. L., and Morel, F. M. M.: Photooxidation of Hg(0) in artificial and natural waters, *Environ Sci Technol*, 35, 1367-1372, doi:10.1021/es001408z, 2001.

Lalonde, J. D., Amyot, M., Orvoine, J., Morel, F. M. M., Auclair, J.-C., and Ariya, P. A.: Photoinduced oxidation of Hg^0(aq) in the waters from the St. Lawrence Estuary, *Environ Sci Technol*, 38, 508-514, doi:10.1021/es034394g, 2004.

Lamborg, C. H., Hammerschmidt, C. R., Gill, G. A., Mason, R. P., and Gichuki, S.: An intercomparison of procedures for the determination of total mercury in seawater and recommendations regarding mercury speciation during GEOTRACES cruises, *Limnol Oceanogr Methods*, 10, 90-100, doi:10.4319/lom.2012.10.90, 2012.

Lamborg, C. H., Hammerschmidt, C. R., Bowman, K. L., Swarr, G. J., Munson, K. M., Ohnemus, D. C., Lam, P. J., Heimburger, L.-E., Rijkenberg, M. J. A., and Saito, M. A.: A global ocean inventory of anthropogenic mercury based on water column measurements, *Nature*, 512, 65-68, doi:10.1038/nature13563, 2014.

Lan, X., Talbot, R., Castro, M., Perry, K., and Luke, W.: Seasonal and diurnal variations of atmospheric mercury across the US determined from AMNet monitoring data, *Atmos Chem Phys*, 12, 10569-10582, doi:10.5194/acp-12-10569-2012, 2012.

Laurier, F., and Mason, R.: Mercury concentration and speciation in the coastal and open ocean boundary layer, *J Geophys Res Atmos*, 112, D06302, doi:10.1029/2006jd007320, 2007.

Legrand, M., Preunkert, S., Frey, M., Bartels-Rausch, T., Kukui, A., King, M. D., Savarino, J., Kerbrat, M., and Jourdain, B.: Large mixing ratios of atmospheric nitrous acid (HONO) at Concordia (East Antarctic Plateau) in summer: a strong source from surface snow?, *Atmos Chem Phys*, 14, 9963-9976, doi:10.5194/acp-14-9963-2014, 2014.

Legrand, M., Preunkert, S., Savarino, J., Frey, M. M., Kukui, A., Helmig, D., Jourdain, B., Jones, A. E., Weller, R., Brough, N., and Gallée, H.: Inter-annual variability of surface ozone at coastal (Dumont d'Urville, 2004–2014) and inland (Concordia, 2007–2014) sites in East Antarctica, *Atmos Chem Phys*, 16, 8053-8069, doi:10.5194/acp-16-8053-2016, 2016a.

Legrand, M., Yang, X., Preunkert, S., and Theys, N.: Year-round records of sea salt, gaseous, and particulate inorganic bromine in the atmospheric boundary layer at coastal (Dumont d'Urville) and central (Concordia) East Antarctic sites, *J Geophys Res Atmos*, 121, 997-1023, doi:10.1002/2015JD024066, 2016b.

Lei, H., Liang, X. Z., Wuebbles, D. J., and Tao, Z.: Model analyses of atmospheric mercury: present air quality and effects of transpacific transport on the United States, *Atmos Chem Phys*, 13, 10807-10825, doi:10.5194/acp-13-10807-2013, 2013.

Li, L., Li, W., and Kushnir, Y.: Variation of the North Atlantic subtropical high western ridge and its implication to Southeastern US summer precipitation, *Clim Dyn*, 39, 1401-1412, doi:10.1007/s00382-011-1214-y, 2012.

Li, W., Li, L., Fu, R., Deng, Y., and Wang, H.: Changes to the North Atlantic Subtropical High and its role in the intensification of summer rainfall variability in the Southeastern United States, *J Climate*, 24, 1499-1506, doi:10.1175/2010jcli3829.1, 2011.

Liao, J., Huey, L. G., Tanner, D. J., Brough, N., Brooks, S., Dibb, J. E., Stutz, J., Thomas, J. L., Lefer, B., Haman, C., and Gorham, K.: Observations of hydroxyl and peroxy radicals and the impact of BrO at Summit, Greenland in 2007 and 2008, *Atmos Chem Phys*, 11, 8577-8591, doi:10.5194/acp-11-8577-2011, 2011.

Libois, Q., Picard, G., Arnaud, L., Morin, S., and Brun, E.: Modeling the impact of snow drift on the decameter-scale variability of snow properties on the Antarctic Plateau, *J Geophys Res Atmos*, 119, 11,662-611,681, doi:10.1002/2014JD022361, 2014.

Lin, C.-J., Gustin, M. S., Singhasuk, P., Eckley, C., and Miller, M.: Empirical models for estimating mercury flux from soils, *Environ Sci Technol*, 44, 8522-8528, doi:10.1021/es1021735, 2010.

Lin, C. J., and Pehkonen, S. O.: The chemistry of atmospheric mercury: A review, *Atmos Environ*, 33, 2067-2079, doi:10.1016/s1352-2310(98)00387-2, 1999.

Lin, C. J., Pongprueksa, P., Lindberg, S. E., Pehkonen, S. O., Byun, D., and Jang, C.: Scientific uncertainties in atmospheric mercury models I: Model science evaluation, *Atmos Environ*, 40, 2911-2928, doi:10.1016/j.atmosenv.2006.01.009, 2006.

Lin, J.-T., and McElroy, M. B.: Impacts of boundary layer mixing on pollutant vertical profiles in the lower troposphere: Implications to satellite remote sensing, *Atmos Environ*, 44, 1726-1739, doi:10.1016/j.atmosenv.2010.02.009, 2010.

Lindberg, S., Bullock, R., Ebinghaus, R., Engstrom, D., Feng, X., Fitzgerald, W., Pirrone, N., Prestbo, E., and Seigneur, C.: A synthesis of progress and uncertainties in attributing the sources of mercury in deposition, *Ambio*, 36, 19-33, doi:10.1579/0044-7447(2007)36[19:asopau]2.0.co;2, 2007.

Lindberg, S. E., Brooks, S., Lin, C. J., Scott, K. J., Landis, M. S., Stevens, R. K., Goodsite, M., and Richter, A.: Dynamic oxidation of gaseous mercury in the Arctic troposphere at polar sunrise, *Environ Sci Technol*, 36, 1245-1256, doi:10.1021/es0111941, 2002.

Liu, S., and Liang, X.-Z.: Observed diurnal cycle climatology of planetary boundary layer height, *J Climate*, 23, 5790-5809, doi:10.1175/2010jcli3552.1, 2010.

Locatelli, R., Bousquet, P., Chevallier, F., Fortems-Cheney, A., Szopa, S., Saunois, M., Agusti-Panareda, A., Bergmann, D., Bian, H., Cameron-Smith, P., Chipperfield, M. P., Gloor, E., Houweling, S., Kawa, S. R., Krol, M., Patra, P. K., Prinn, R. G., Rigby, M., Saito, R., and Wilson, C.: Impact of transport model errors on the global and regional methane emissions estimated by inverse modelling, *Atmos Chem Phys*, 13, 9917-9937, doi:10.5194/acp-13-9917-2013, 2013.

Loux, N. T.: A critical assessment of elemental mercury air/water exchange parameters, *Chem Spec Bioavailab*, 16, 127-138, doi:10.3184/095422904782775018, 2004.

Lyman, S. N., Gustin, M. S., Prestbo, E. M., and Marsik, F. J.: Estimation of dry deposition of atmospheric mercury in Nevada by direct and indirect methods, *Environ Sci Technol*, 41, 1970-1976, doi:10.1021/es062323m, 2007.

Lyman, S. N., and Jaffe, D. A.: Formation and fate of oxidized mercury in the upper troposphere and lower stratosphere, *Nature Geosci*, 5, 114-117, doi:10.1038/ngeo1353, 2012.

Ma, M., Wang, D., Sun, R., Shen, Y., and Huang, L.: Gaseous mercury emissions from subtropical forested and open field soils in a national nature reserve, southwest China, *Atmos Environ*, 64, 116-123, doi:10.1016/j.atmosenv.2012.09.038, 2013.

Mason, R. P., and Fitzgerald, W. F.: The distribution and biogeochemical cycling of mercury in the equatorial Pacific Ocean, *Deep-Sea Res Pt I*, 40, 1897-1924, doi:10.1016/0967-0637(93)90037-4, 1993.

Mason, R. P., Rolfhus, K. R., and Fitzgerald, W. F.: Mercury in the North Atlantic, *Mar Chem*, 61, 37-53, doi:10.1016/S0304-4203(98)00006-1, 1998.

Mason, R. P., Lawson, N. M., and Sheu, G. R.: Mercury in the Atlantic Ocean: factors controlling air–sea exchange of mercury and its distribution in the upper waters, *Deep-Sea Res Pt II*, 48, 2829-2853, doi:10.1016/S0967-0645(01)00020-0, 2001.

Mason, R. P., and Sheu, G. R.: Role of the ocean in the global mercury cycle, *Global Biogeochem Cy*, 16, 1093, doi:10.1029/2001gb001440, 2002.

Mason, R. P.: Mercury emissions from natural processes and their importance in the global mercury cycle, in: Mercury Fate and Transport in the Global Atmosphere, edited by: Mason, R. P., and Pirrone, N., Springer, New York, NY, USA, 2009.

McClure, C., Jaffe, D. A., and Edgerton, E. S.: Evaluation of the KCl denuder method for gaseous oxidized mercury using $HgBr_2$ at an in-service AMNet site, *Environ Sci Technol*, doi:10.1021/es502545k, 2014.

Mergler, D., Anderson, H. A., Chan, L. H. M., Mahaffey, K. R., Murray, M., Sakamoto, M., and Stern, A. H.: Methylmercury exposure and health effects in humans: a worldwide concern, *Ambio*, 36, 3-11, doi:10.1579/0044-7447(2007)36[3:meahei]2.0.co;2, 2007.

Miller, S. M., Wofsy, S. C., Michalak, A. M., Kort, E. A., Andrews, A. E., Biraud, S. C., Dlugokencky, E. J., Eluszkiewicz, J., Fischer, M. L., Janssens-Maenhout, G., Miller, B. R., Miller, J. B., Montzka, S. A., Nehrkorn, T., and Sweeney, C.: Anthropogenic emissions of methane in the United States, *P Natl Acad Sci*, 110, 20018-20022, doi:10.1073/pnas.1314392110, 2013.

MOEJ: Ministry of the Environment, Japan: Monitoring results of atmosphere mercury background concentration (In Japanese), available at: http://www.env.go.jp/press/press.php?serial=16473, 2013.

Moore, C. W.: Factors influencing surface atmosphere exchange of gaseous elemental mercury in western Maryland, University of Maryland, College Park, Marine-Estuarine-Environmental Sciences Program, College Park, Maryland, USA, 2011.

Müller, D., Wip, D., Warneke, T., Holmes, C. D., Dastoor, A., and Notholt, J.: Sources of atmospheric mercury in the tropics: continuous observations at a coastal site in Suriname, *Atmos Chem Phys*, 12, 7391-7397, doi:10.5194/acp-12-7391-2012, 2012.

Munson, K. M., Lamborg, C. H., Swarr, G. J., and Saito, M. A.: Mercury species concentrations and fluxes in the Central Tropical Pacific Ocean, *Global Biogeochem Cy*, 29, 656-676, doi:10.1002/2015GB005120, 2015.

Muntean, M., Janssens-Maenhout, G., Song, S., Selin, N. E., Olivier, J. G. J., Guizzardi, D., Maas, R., and Dentener, F.: Trend analysis from 1970 to 2008 and model evaluation of EDGARv4 global gridded anthropogenic mercury emissions, *Sci Total Environ*, 494–495, 337-350, doi:10.1016/j.scitotenv.2014.06.014, 2014.

Munthe, J., Wängberg, I., Pirrone, N., Iverfeldt, Å., Ferrara, R., Ebinghaus, R., Feng, X., Gårdfeldt, K., Keeler, G., Lanzillotta, E., Lindberg, S. E., Lu, J., Mamane, Y., Prestbo, E., Schmolke, S., Schroeder, W. H., Sommar, J., Sprovieri, F., Stevens, R. K., Stratton, W., Tuncel, G., and Urba, A.: Intercomparison of methods for sampling and analysis of atmospheric mercury species, *Atmos Environ*, 35, 3007-3017, doi:10.1016/S1352-2310(01)00104-2, 2001.

NADP/MDN: Mercury Deposition Network, National Atmospheric Deposition Program, available at: http://nadp.sws.uiuc.edu/mdn/, 2012.

NBSC: China Energy Statistical Yearbook 2014, available at: http://www.stats.gov.cn/tjsj/, 2015.

Nightingale, P. D., Malin, G., Law, C. S., Watson, A. J., Liss, P. S., Liddicoat, M. I., Boutin, J., and Upstill-Goddard, R. C.: In situ evaluation of air-sea gas exchange parameterizations using novel conservative and volatile tracers, *Global Biogeochem Cy*, 14, 373-387, doi:10.1029/1999gb900091, 2000.

Obrist, D., Pokharel, A. K., and Moore, C.: Vertical profile measurements of soil air suggest immobilization of gaseous elemental mercury in mineral soil, *Environ Sci Technol*, 48, 2242-2252, doi:10.1021/es4048297, 2014.

Pal, B., and Ariya, P. A.: Gas-phase HO•-Initiated reactions of elemental mercury: kinetics, product studies, and atmospheric implications, *Environ Sci Technol*, 38, 5555-5566, doi:10.1021/es0494353, 2004.

Pan, L., Chai, T., Carmichael, G. R., Tang, Y., Streets, D., Woo, J.-H., Friedli, H. R., and Radke, L. F.: Top-down estimate of mercury emissions in China using four-dimensional variational data assimilation, *Atmos Environ*, 41, 2804-2819, doi:10.1016/j.atmosenv.2006.11.048, 2007.

Park, S.-Y., Kim, P.-R., and Han, Y.-J.: Mercury exchange flux from two different soil types and affecting parameters, *Asian J Atmos Environ*, 7, 199-208, doi:10.5572/ajae.2013.7.4.199, 2013.

Parrella, J. P., Jacob, D. J., Liang, Q., Zhang, Y., Mickley, L. J., Miller, B., Evans, M. J., Yang, X., Pyle, J. A., Theys, N., and Van Roozendael, M.: Tropospheric bromine chemistry: Implications for present and pre-industrial ozone and mercury, *Atmos Chem Phys*, 12, 6723-6740, doi:10.5194/acp-12-6723-2012, 2012.

Peleg, M., Tas, E., Obrist, D., Matveev, V., Moore, C., Gabay, M., and Luria, M.: Observational evidence for involvement of nitrate radicals in nighttime oxidation of mercury, *Environ Sci Technol*, 49, 14008-14018, doi:10.1021/acs.est.5b03894, 2015.

Pfaffhuber, K. A., Berg, T., Hirdman, D., and Stohl, A.: Atmospheric mercury observations from Antarctica: seasonal variation and source and sink region calculations, *Atmos Chem Phys*, 12, 3241-3251, doi:10.5194/acp-12-3241-2012, 2012.

Picard, G., Libois, Q., Arnaud, L., Verin, G., and Dumont, M.: Development and calibration of an automatic spectral albedometer to estimate near-surface snow SSA time series, *Cryosphere*, 10, 1297-1316, doi:10.5194/tc-10-1297-2016, 2016.

Pirrone, N., Cinnirella, S., Feng, X. B., Finkelman, R. B., Friedli, H. R., Leaner, J., Mason, R., Mukherjee, A. B., Stracher, G. B., Streets, D. G., and Telmer, K.: Global mercury emissions to the atmosphere from anthropogenic and natural sources, *Atmos Chem Phys*, 10, 5951-5964, doi:10.5194/acp-10-5951-2010, 2010.

Pirrone, N., Aas, W., Cinnirella, S., Ebinghaus, R., Hedgecock, I. M., Pacyna, J., Sprovieri, F., and Sunderland, E. M.: Toward the next generation of air quality monitoring: Mercury, *Atmos Environ*, 80, 599-611, doi:10.1016/j.atmosenv.2013.06.053, 2013.

Platt, U., and Janssen, C.: Observation and role of the free radicals NO3, ClO, BrO and IO in the troposphere, *Farad Discuss*, 100, 175-198, doi:10.1039/FD9950000175, 1995.

Pohl, C., Croot, P. L., Hennings, U., Daberkow, T., Budeus, G., and Loeff, M. R. v. d.: Synoptic transects on the distribution of trace elements (Hg, Pb, Cd, Cu, Ni, Zn, Co, Mn, Fe, and Al) in surface waters of the Northern- and Southern East Atlantic, *J Marine Syst*, 84, 28-41, doi:10.1016/j.jmarsys.2010.08.003, 2011.

Poissant, L., Pilote, M., Beauvais, C., Constant, P., and Zhang, H. H.: A year of continuous measurements of three atmospheric mercury species (GEM, RGM and Hgp) in southern Québec, Canada, *Atmos Environ*, 39, 1275-1287, doi:10.1016/j.atmosenv.2004.11.007, 2005.

Pongprueksa, P., Lin, C. J., Singhasuk, P., Pan, L., Ho, T. C., and Chu, H. W.: Application of CMAQ at a hemispheric scale for atmospheric mercury simulations, *Geosci Model Dev Discuss*, 4, 1723-1754, doi:10.5194/gmdd-4-1723-2011, 2011.

Poulain, A. J., Lalonde, J. D., Amyot, M., Shead, J. A., Raofie, F., and Ariya, P. A.: Redox transformations of mercury in an Arctic snowpack at springtime, *Atmos Environ*, 38, 6763-6774, doi:10.1016/j.atmosenv.2004.09.013, 2004.

Prestbo, E. M., and Gay, D. A.: Wet deposition of mercury in the U.S. and Canada, 1996–2005: Results and analysis of the NADP mercury deposition network (MDN), *Atmos Environ*, 43, 4223-4233, doi:10.1016/j.atmosenv.2009.05.028, 2009.

Preunkert, S., Legrand, M., Frey, M. M., Kukui, A., Savarino, J., Gallée, H., King, M., Jourdain, B., Vicars, W., and Helmig, D.: Formaldehyde (HCHO) in air, snow, and interstitial air at Concordia (East Antarctic Plateau) in summer, *Atmos Chem Phys*, 15, 6689-6705, doi:10.5194/acp-15-6689-2015, 2015.

Prinn, R. G.: Measurement equation for trace chemicals in fluids and solution of its inverse, in: Inverse Methods in Global Biogeochemical Cycles, Geophys Monogr Ser, AGU, Washington, DC, 3-18, 2000.

Prinn, R. G., Heimbach, P., Rigby, M., Dutkiewicz, S., Melillo, J. M., Reilly, J. M., Kicklighter, D. W., and Waugh, C.: A strategy for a global observing system for verification of national greenhouse gas emissions, MIT Joint Program on the Science and Policy of Global Change, 2011.

Qureshi, A., O'Driscoll, N. J., MacLeod, M., Neuhold, Y.-M., and Hungerbühler, K.: Photoreactions of mercury in surface ocean water: gross reaction kinetics and possible pathways, *Environ Sci Technol*, 44, 644-649, doi:10.1021/es9012728, 2010.

Rafaj, P., Bertok, I., Cofala, J., and Schöpp, W.: Scenarios of global mercury emissions from anthropogenic sources, *Atmos Environ*, 79, 472-479, doi:10.1016/j.atmosenv.2013.06.042, 2013.

Ridley, B. A., and Grahek, F. E.: A small, low flow, high sensitivity reaction vessel for NO chemiluminescence detectors, *J Atmos Oceanic Tech*, 7, 307-311, doi:10.1175/1520-0426(1990)007<0307:aslfhs>2.0.co;2, 1990.

Rigby, M., Manning, A. J., and Prinn, R. G.: The value of high-frequency, high-precision methane isotopologue measurements for source and sink estimation, *J Geophys Res Atmos*, 117, D12312, doi:10.1029/2011jd017384, 2012.

Rosner, B., and Grove, D.: Use of the Mann–Whitney *U*-test for clustered data, *Stat Med*, 18, 1387-1400, doi:10.1002/(SICI)1097-0258(19990615)18:11<1387::AID-SIM126>3.0.CO;2-V, 1999.

Roustan, Y., and Bocquet, M.: Inverse modelling for mercury over Europe, *Atmos Chem Phys*, 6, 3085-3098, doi:10.5194/acp-6-3085-2006, 2006.

Saikawa, E., Rigby, M., Prinn, R. G., Montzka, S. A., Miller, B. R., Kuijpers, L. J. M., Fraser, P. J. B., Vollmer, M. K., Saito, T., Yokouchi, Y., Harth, C. M., Mühle, J., Weiss, R. F., Salameh, P. K., Kim, J., Li, S., Park, S., Kim, K. R., Young, D., O'Doherty, S., Simmonds, P. G., McCulloch, A., Krummel, P. B., Steele, L. P., Lunder, C., Hermansen, O., Maione, M., Arduini, J., Yao, B., Zhou, L. X., Wang, H. J., Elkins, J. W., and Hall, B.: Global and regional emission estimates for HCFC-22, *Atmos Chem Phys*, 12, 10033-10050, doi:10.5194/acp-12-10033-2012, 2012.

Sanders, R., Henson, S. A., Koski, M., De La Rocha, C. L., Painter, S. C., Poulton, A. J., Riley, J., Salihoglu, B., Visser, A., Yool, A., Bellerby, R., and Martin, A. P.: The biological carbon pump in the North Atlantic, *Prog Oceanogr*, doi:10.1016/j.pocean.2014.05.005, 2014.

Schroeder, W. H., Keeler, G., Kock, H., Roussel, P., Schneeberger, D., and Schaedlich, F.: International field intercomparison of atmospheric mercury measurement methods, *Water Air Soil Poll*, 80, 611-620, doi:10.1007/bf01189713, 1995.

Seidel, D. J., Ao, C. O., and Li, K.: Estimating climatological planetary boundary layer heights from radiosonde observations: Comparison of methods and uncertainty analysis, *J Geophys Res Atmos*, 115, doi:10.1029/2009jd013680, 2010.

Seigneur, C., and Lohman, K.: Effect of bromine chemistry on the atmospheric mercury cycle, *J Geophys Res Atmos*, 113, D23309, doi:10.1029/2008jd010262, 2008.

Selin, N. E., Jacob, D. J., Park, R. J., Yantosca, R. M., Strode, S., Jaeglé, L., and Jaffe, D.: Chemical cycling and deposition of atmospheric mercury: Global constraints from observations, *J Geophys Res Atmos*, 112, doi:10.1029/2006jd007450, 2007.

Selin, N. E., Jacob, D. J., Yantosca, R. M., Strode, S., Jaeglé, L., and Sunderland, E. M.: Global 3-D land-ocean-atmosphere model for mercury: Present-day versus preindustrial cycles and anthropogenic enrichment factors for deposition, *Global Biogeochem Cy*, 22, GB2011, doi:10.1029/2007gb003040, 2008.

Selin, N. E.: Global biogeochemical cycling of mercury: a review, *Annu Rev Env Resour*, 34, 43-63, doi:10.1146/annurev.environ.051308.084314, 2009.

Shah, V., Jaeglé, L., Gratz, L. E., Ambrose, J. L., Jaffe, D. A., Selin, N. E., Song, S., Campos, T. L., Flocke, F. M., Reeves, M., Stechman, D., Stell, M., Festa, J., Stutz, J., Weinheimer, A. J., Knapp, D. J., Montzka, D. D., Tyndall, G. S., Apel, E. C., Hornbrook, R. S., Hills, A. J., Riemer, D. D., Blake, N. J., Cantrell, C. A., and Mauldin Iii, R. L.: Origin of oxidized mercury in the summertime free troposphere over the southeastern US, *Atmos Chem Phys*, 16, 1511-1530, doi:10.5194/acp-16-1511-2016, 2016.

Shepler, B. C., Balabanov, N. B., and Peterson, K. A.: Hg+Br→HgBr recombination and collision-induced dissociation dynamics, *J Chem Phys*, 127, 164304, doi:10.1063/1.2777142, 2007.

Sherwen, T., Schmidt, J. A., Evans, M. J., Carpenter, L. J., Großmann, K., Eastham, S. D., Jacob, D. J., Dix, B., Koenig, T. K., Sinreich, R., Ortega, I., Volkamer, R., Saiz-Lopez, A., Prados-Roman, C., Mahajan, A. S., and Ordóñez, C.: Global impacts of tropospheric halogens (Cl, Br, I) on oxidants and composition in GEOS-Chem, *Atmos Chem Phys Discuss*, 2016, 1-52, doi:10.5194/acp-2016-424, 2016.

Shetty, S. K., Lin, C.-J., Streets, D. G., and Jang, C.: Model estimate of mercury emission from natural sources in East Asia, *Atmos Environ*, 42, 8674-8685, doi:10.1016/j.atmosenv.2008.08.026, 2008.

Sheu, G.-R., Lin, N.-H., Wang, J.-L., Lee, C.-T., Ou Yang, C.-F., and Wang, S.-H.: Temporal distribution and potential sources of atmospheric mercury measured at a high-elevation background station in Taiwan, *Atmos Environ*, 44, 2393-2400, doi:10.1016/j.atmosenv.2010.04.009, 2010.

Simpson, W. R., von Glasow, R., Riedel, K., Anderson, P., Ariya, P., Bottenheim, J., Burrows, J., Carpenter, L. J., Frieß, U., Goodsite, M. E., Heard, D., Hutterli, M., Jacobi, H. W., Kaleschke, L., Neff, B., Plane, J., Platt, U., Richter, A., Roscoe, H., Sander, R., Shepson, P., Sodeau, J., Steffen, A., Wagner, T., and Wolff, E.: Halogens and their role in polar boundary-layer ozone depletion, *Atmos Chem Phys*, 7, 4375-4418, doi:10.5194/acp-7-4375-2007, 2007.

Six, D., Fily, M., Alvain, S., Henry, P., and Benoist, J.-P.: Surface characterisation of the Dome Concordia area (Antarctica) as a potential satellite calibration site, using Spot 4/Vegetation instrument, *Remote Sens Environ*, 89, 83-94, doi:10.1016/j.rse.2003.10.006, 2004.

Six, D., Fily, M., Blarel, L., and Goloub, P.: First aerosol optical thickness measurements at Dome C (East Antarctica), summer season 2003–2004, *Atmos Environ*, 39, 5041-5050, doi:10.1016/j.atmosenv.2005.05.010, 2005.

Skov, H., Brooks, S. B., Goodsite, M. E., Lindberg, S. E., Meyers, T. P., Landis, M. S., Larsen, M. R. B., Jensen, B., McConville, G., and Christensen, J.: Fluxes of reactive gaseous mercury measured with a newly developed method using relaxed eddy accumulation, *Atmos Environ*, 40, 5452-5463, doi:10.1016/j.atmosenv.2006.04.061, 2006.

Slemr, F., Brunke, E. G., Ebinghaus, R., and Kuss, J.: Worldwide trend of atmospheric mercury since 1995, *Atmos Chem Phys*, 11, 4779-4787, doi:10.5194/acp-11-4779-2011, 2011.

Slemr, F., Brunke, E. G., Whittlestone, S., Zahorowski, W., Ebinghaus, R., Kock, H. H., and Labuschagne, C.: ^{222}Rn-calibrated mercury fluxes from terrestrial surface of southern Africa, *Atmos Chem Phys*, 13, 6421-6428, doi:10.5194/acp-13-6421-2013, 2013.

Slemr, F., Weigelt, A., Ebinghaus, R., Brenninkmeijer, C., Baker, A., Schuck, T., Rauthe-Schöch, A., Riede, H., Leedham, E., Hermann, M., van Velthoven, P., Oram, D., Sullivan, D., Dyroff, C., Zahn, A., and Ziereis, H.: Mercury plumes in the global upper troposphere observed during flights with the CARIBIC observatory from May 2005 until June 2013, *Atmosphere*, 5, 342, doi:10.3390/atmos5020342, 2014.

Slemr, F., Angot, H., Dommergue, A., Magand, O., Barret, M., Weigelt, A., Ebinghaus, R., Brunke, E. G., Pfaffhuber, K. A., Edwards, G., Howard, D., Powell, J., Keywood, M., and Wang, F.: Comparison of mercury concentrations measured at several sites in the Southern Hemisphere, *Atmos Chem Phys*, 15, 3125-3133, doi:10.5194/acp-15-3125-2015, 2015.

Smith-Downey, N. V., Sunderland, E. M., and Jacob, D. J.: Anthropogenic impacts on global storage and emissions of mercury from terrestrial soils: Insights from a new global model, *J Geophys Res Biogeo*, 115, G03008, doi:10.1029/2009jg001124, 2010.

Snider, G., Raofie, F., and Ariya, P. A.: Effects of relative humidity and CO(g) on the O3-initiated oxidation reaction of Hg0(g): kinetic & product studies, *Phys Chem Chem Phys*, 10, 5616-5623, doi:10.1039/B801226A, 2008.

Soerensen, A. L., Skov, H., Jacob, D. J., Soerensen, B. T., and Johnson, M. S.: Global concentrations of gaseous elemental mercury and reactive gaseous mercury in the marine boundary layer, *Environ Sci Technol*, 44, 7425-7430, doi:10.1021/es903839n, 2010a.

Soerensen, A. L., Sunderland, E. M., Holmes, C. D., Jacob, D. J., Yantosca, R. M., Skov, H., Christensen, J. H., Strode, S. A., and Mason, R. P.: An improved global model for air-sea exchange of mercury: High concentrations over the North Atlantic, *Environ Sci Technol*, 44, 8574-8580, doi:10.1021/es102032g, 2010b.

Soerensen, A. L., Jacob, D. J., Streets, D. G., Witt, M. L. I., Ebinghaus, R., Mason, R. P., Andersson, M., and Sunderland, E. M.: Multi-decadal decline of mercury in the North Atlantic atmosphere explained by changing subsurface seawater concentrations, *Geophys Res Lett*, 39, L21810, doi:10.1029/2012gl053736, 2012.

Soerensen, A. L., Mason, R. P., Balcom, P. H., and Sunderland, E. M.: Drivers of surface ocean mercury concentrations and air–sea exchange in the West Atlantic Ocean, *Environ Sci Technol*, 47, 7757-7765, doi:10.1021/es401354q, 2013.

Sommar, J., Gårdfeldt, K., Strömberg, D., and Feng, X.: A kinetic study of the gas-phase reaction between the hydroxyl radical and atomic mercury, *Atmos Environ*, 35, 3049-3054, doi:10.1016/S1352-2310(01)00108-X, 2001.

Sommar, J., Andersson, M. E., and Jacobi, H. W.: Circumpolar measurements of speciated mercury, ozone and carbon monoxide in the boundary layer of the Arctic Ocean, *Atmos Chem Phys*, 10, 5031-5045, doi:10.5194/acp-10-5031-2010, 2010.

Song, S., Selin, N. E., Soerensen, A. L., Angot, H., Artz, R., Brooks, S., Brunke, E. G., Conley, G., Dommergue, A., Ebinghaus, R., Holsen, T. M., Jaffe, D. A., Kang, S., Kelley, P., Luke, W. T., Magand, O., Marumoto, K., Pfaffhuber, K. A., Ren, X., Sheu, G. R., Slemr, F., Warneke, T., Weigelt, A., Weiss-Penzias, P., Wip, D. C., and Zhang, Q.: Top-down constraints on atmospheric mercury emissions and implications for global biogeochemical cycling, *Atmos Chem Phys*, 15, 7103-7125, doi:10.5194/acp-15-7103-2015, 2015.

Song, S., Selin, N. E., Gratz, L. E., Ambrose, J. L., Jaffe, D. A., Shah, V., Jaeglé, L., Giang, A., Yuan, B., and Kaser, L.: Constraints from observations and modeling on atmosphere–surface exchange of mercury in eastern North America, *Elementa: Science of the Anthropocene*, 4, 000100, doi:10.12952/journal.elementa.000100, 2016.

Stamenkovic, J., and Gustin, M. S.: Nonstomatal versus stomatal uptake of atmospheric mercury, *Environ Sci Technol*, 43, 1367-1372, doi:10.1021/es801583a, 2009.

Steffen, A., Douglas, T., Amyot, M., Ariya, P., Aspmo, K., Berg, T., Bottenheim, J., Brooks, S., Cobbett, F., Dastoor, A., Dommergue, A., Ebinghaus, R., Ferrari, C., Gardfeldt, K., Goodsite, M. E., Lean, D., Poulain, A. J., Scherz, C., Skov, H., Sommar, J., and Temme, C.: A synthesis of atmospheric mercury depletion event chemistry in the atmosphere and snow, *Atmos Chem Phys*, 8, 1445-1482, doi:10.5194/acp-8-1445-2008, 2008.

Steffen, A., Scherz, T., Olson, M., Gay, D., and Blanchard, P.: A comparison of data quality control protocols for atmospheric mercury speciation measurements, *J Environ Monit*, 14, 752-765, doi:10.1039/c2em10735j, 2012.

Steffen, A., Bottenheim, J., Cole, A., Ebinghaus, R., Lawson, G., and Leaitch, W. R.: Atmospheric mercury speciation and mercury in snow over time at Alert, Canada, *Atmos Chem Phys*, 14, 2219-2231, doi:10.5194/acp-14-2219-2014, 2014.

Stein, A. F., Draxler, R. R., Rolph, G. D., Stunder, B. J. B., Cohen, M. D., and Ngan, F.: NOAA's HYSPLIT atmospheric transport and dispersion modeling system, *Bull Amer Meteor Soc*, 96, 2059-2077, doi:10.1175/BAMS-D-14-00110.1, 2015.

Stein, E. D., Cohen, Y., and Winer, A. M.: Environmental distribution and transformation of mercury compounds, *Crit Rev Env Sci Tec*, 26, 1-43, doi:10.1080/10643389609388485, 1996.

Streets, D. G., Zhang, Q., and Wu, Y.: Projections of global mercury emissions in 2050, *Environ Sci Technol*, 43, 2983-2988, doi:10.1021/es802474j, 2009.

Streets, D. G., Devane, M. K., Lu, Z., Bond, T. C., Sunderland, E. M., and Jacob, D. J.: All-time releases of mercury to the atmosphere from human activities, *Environ Sci Technol*, 45, 10485-10491, doi:10.1021/es202765m, 2011.

Strode, S. A., Jaeglé, L., Selin, N. E., Jacob, D. J., Park, R. J., Yantosca, R. M., Mason, R. P., and Slemr, F.: Air-sea exchange in the global mercury cycle, *Global Biogeochem Cy*, 21, GB1017, doi:10.1029/2006gb002766, 2007.

Strode, S. A., Jaeglé, L., Jaffe, D. A., Swartzendruber, P. C., Selin, N. E., Holmes, C., and Yantosca, R. M.: Trans-Pacific transport of mercury, *J Geophys Res Atmos*, 113, D15305, doi:10.1029/2007jd009428, 2008.

Stutz, J., Thomas, J. L., Hurlock, S. C., Schneider, M., von Glasow, R., Piot, M., Gorham, K., Burkhart, J. F., Ziemba, L., Dibb, J. E., and Lefer, B. L.: Longpath DOAS observations of surface BrO at Summit, Greenland, *Atmos Chem Phys*, 11, 9899-9910, doi:10.5194/acp-11-9899-2011, 2011.

Subir, M., Ariya, P. A., and Dastoor, A. P.: A review of uncertainties in atmospheric modeling of mercury chemistry I. Uncertainties in existing kinetic parameters – Fundamental limitations and the importance of heterogeneous chemistry, *Atmos Environ*, 45, 5664-5676, doi:10.1016/j.atmosenv.2011.04.046, 2011.

Subir, M., Ariya, P. A., and Dastoor, A. P.: A review of the sources of uncertainties in atmospheric mercury modeling II. Mercury surface and heterogeneous chemistry – A missing link, *Atmos Environ*, 46, 1-10, doi:10.1016/j.atmosenv.2011.07.047, 2012.

Sumner, A. L., Spicer, C. W., Satola, J., Mangaraj, R., Cowen, K. A., Landis, M. S., Stevens, R. K., and Atkeson, T. D.: Environmental Chamber Studies of Mercury Reactions in the Atmosphere, in: Dynamics of Mercury Pollution on Regional and Global Scales:: Atmospheric Processes and Human Exposures Around the World, edited by: Pirrone, N., and Mahaffey, K. R., Springer US, Boston, MA, 193-212, 2005.

Sunderland, E. M., and Mason, R. P.: Human impacts on open ocean mercury concentrations, *Global Biogeochem Cy*, 21, GB4022, doi:10.1029/2006gb002876, 2007.

Sunderland, E. M., Krabbenhoft, D. P., Moreau, J. W., Strode, S. A., and Landing, W. M.: Mercury sources, distribution, and bioavailability in the North Pacific Ocean: Insights from data and models, *Global Biogeochem Cy*, 23, GB2010, doi:10.1029/2008gb003425, 2009.

Sunderland, E. M., Dalziel, J., Heyes, A., Branfireun, B. A., Krabbenhoft, D. P., and Gobas, F. A. P. C.: Response of a macrotidal estuary to changes in anthropogenic mercury loading between 1850 and 2000, *Environ Sci Technol*, 44, 1698-1704, doi:10.1021/es9032524, 2010.

Swartzendruber, P. C., Jaffe, D. A., Prestbo, E. M., Weiss-Penzias, P., Selin, N. E., Park, R., Jacob, D. J., Strode, S., and Jaeglé, L.: Observations of reactive gaseous mercury in the free troposphere at the Mount Bachelor Observatory, *J Geophys Res Atmos*, 111, doi:10.1029/2006JD007415, 2006.

Temme, C., Einax, J. W., Ebinghaus, R., and Schroeder, W. H.: Measurements of Atmospheric Mercury Species at a Coastal Site in the Antarctic and over the South Atlantic Ocean during Polar Summer, *Environ Sci Technol*, 37, 22-31, doi:10.1021/es025884w, 2003a.

Temme, C., Slemr, F., Ebinghaus, R., and Einax, J. W.: Distribution of mercury over the Atlantic Ocean in 1996 and 1999–2001, *Atmos Environ*, 37, 1889-1897, doi:10.1016/S1352-2310(03)00069-4, 2003b.

Temme, C., Ebinghaus, R., Kock, H. H., Schwerin, A., and Bieber, E.: Field intercomparison of mercury measurements within EMEP (executive summary), 2006.

Thomas, J. L., Stutz, J., Lefer, B., Huey, L. G., Toyota, K., Dibb, J. E., and von Glasow, R.: Modeling chemistry in and above snow at Summit, Greenland – Part 1: Model description and results, *Atmos Chem Phys*, 11, 4899-4914, doi:10.5194/acp-11-4899-2011, 2011.

Timonen, H., Ambrose, J. L., and Jaffe, D. A.: Oxidation of elemental Hg in anthropogenic and marine airmasses, *Atmos Chem Phys*, 13, 2827-2836, doi:10.5194/acp-13-2827-2013, 2013.

Toyota, K., Dastoor, A. P., and Ryzhkov, A.: Air–snowpack exchange of bromine, ozone and mercury in the springtime Arctic simulated by the 1-D model PHANTAS – Part 2: Mercury and its speciation, *Atmos Chem Phys*, 14, 4135-4167, doi:10.5194/acp-14-4135-2014, 2014.

Tørseth, K., Aas, W., Breivik, K., Fjæraa, A. M., Fiebig, M., Hjellbrekke, A. G., Lund Myhre, C., Solberg, S., and Yttri, K. E.: Introduction to the European Monitoring and Evaluation Programme (EMEP) and observed atmospheric composition change during 1972-2009, *Atmos Chem Phys*, 12, 5447-5481, doi:10.5194/acp-12-5447-2012, 2012.

Travnikov, O., and Ilyin, I.: The EMEP/MSC-E mercury modeling system, in: Mercury Fate and Transport in the Global Atmosphere, edited by: Mason, R., and Pirrone, N., Springer US, 571-587, 2009.

Ulrych, T., Sacchi, M., and Woodbury, A.: A Bayes tour of inversion: A tutorial, *Geophysics*, 66, 55-69, doi:10.1190/1.1444923, 2001.

Van Dam, B., Helmig, D., Neff, W., and Kramer, L.: Evaluation of boundary layer depth estimates at Summit Station, Greenland, *J Appl Meteor Climatol*, 52, 2356-2362, doi:10.1175/JAMC-D-13-055.1, 2013.

van der Werf, G. R., Randerson, J. T., Giglio, L., Collatz, G. J., Mu, M., Kasibhatla, P. S., Morton, D. C., DeFries, R. S., Jin, Y., and van Leeuwen, T. T.: Global fire emissions and the contribution of deforestation, savanna, forest, agricultural, and peat fires (1997–2009), *Atmos Chem Phys*, 10, 11707-11735, doi:10.5194/acp-10-11707-2010, 2010.

Wan, Q., Feng, X. B., Lu, J. L., Zheng, W., Song, X. J., Han, S. J., and Xu, H.: Atmospheric mercury in Changbai Mountain area, northeastern China I. The seasonal distribution pattern of total gaseous mercury and its potential sources, *Environ Res*, 109, 201-206, doi:10.1016/j.envres.2008.12.001, 2009.

Wang, D., He, L., Shi, X., Wei, S., and Feng, X.: Release flux of mercury from different environmental surfaces in Chongqing, China, *Chemosphere*, 64, 1845-1854, doi:10.1016/j.chemosphere.2006.01.054, 2006.

Wang, F., Saiz-Lopez, A., Mahajan, A. S., Gómez Martín, J. C., Armstrong, D., Lemes, M., Hay, T., and Prados-Roman, C.: Enhanced production of oxidised mercury over the tropical Pacific Ocean: a key missing oxidation pathway, *Atmos Chem Phys*, 14, 1323-1335, doi:10.5194/acp-14-1323-2014, 2014a.

Wang, S., Zhang, Q., Martin, R. V., Philip, S., Liu, F., Li, M., Jiang, X., and He, K.: Satellite measurements oversee China's sulfur dioxide emission reductions from coal-fired power plants, *Environ Res Lett*, 10, 114015, doi:10.1088/1748-9326/10/11/114015, 2015.

Wang, X., Lin, C. J., and Feng, X.: Sensitivity analysis of an updated bidirectional air–surface exchange model for elemental mercury vapor, *Atmos Chem Phys*, 14, 6273-6287, doi:10.5194/acp-14-6273-2014, 2014b.

Wang, X., Bao, Z., Lin, C.-J., Yuan, W., and Feng, X.: Assessment of global mercury deposition through litterfall, *Environ Sci Technol*, doi:10.1021/acs.est.5b06351, 2016.

Weigelt, A., Temme, C., Bieber, E., Schwerin, A., Schuetze, M., Ebinghaus, R., and Kock, H. H.: Measurements of atmospheric mercury species at a German rural background site from 2009 to 2011 – methods and results, *Environ Chem*, 10, 102-110, doi:10.1071/EN12107, 2013.

Weigelt, A., Ebinghaus, R., Manning, A. J., Derwent, R. G., Simmonds, P. G., Spain, T. G., Jennings, S. G., and Slemr, F.: Analysis and interpretation of 18 years of mercury observations since 1996 at Mace Head, Ireland, *Atmos Environ*, 100, 85-93, doi:10.1016/j.atmosenv.2014.10.050, 2015.

Wesely, M. L.: Parameterization of surface resistances to gaseous dry deposition in regional-scale numerical models, *Atmos Environ*, 23, 1293-1304, doi:10.1016/0004-6981(89)90153-4, 1989.

Wilke, C. R., and Chang, P.: Correlation of diffusion coefficients in dilute solutions, *AIChE Journal*, 1, 264-270, doi:10.1002/aic.690010222, 1955.

Wu, Q., Wang, S., Zhang, L., Hui, M., Wang, F., and Hao, J.: Flow analysis of the mercury associated with nonferrous ore concentrates: Implications on mercury emissions and recovery in China, *Environ Sci Technol*, doi:10.1021/acs.est.5b04934, 2016.

Wunsch, C.: Discrete inverse and state estimation problems: with geophysical fluid applications, Cambridge University Press, New York, USA, 43-69 pp., 2006.

Xiao, X., Prinn, R. G., Fraser, P. J., Weiss, R. F., Simmonds, P. G., O'Doherty, S., Miller, B. R., Salameh, P. K., Harth, C. M., Krummel, P. B., Golombek, A., Porter, L. W., Butler, J. H., Elkins, J. W., Dutton, G. S., Hall, B. D., Steele, L. P., Wang, R. H. J., and Cunnold, D. M.: Atmospheric three-dimensional inverse modeling of regional industrial emissions and global oceanic uptake of carbon tetrachloride, *Atmos Chem Phys*, 10, 10421-10434, doi:10.5194/acp-10-10421-2010, 2010.

Xu, X., Yang, X., R. Miller, D., Helble, J. J., and Carley, R. J.: Formulation of bi-directional atmosphere-surface exchanges of elemental mercury, *Atmos Environ*, 33, 4345-4355, doi:10.1016/S1352-2310(99)00245-9, 1999.

Ye, Z., Mao, H., Lin, C. J., and Kim, S. Y.: Investigation of processes controlling summertime gaseous elemental mercury oxidation at midlatitudinal marine, coastal, and inland sites, *Atmos Chem Phys*, 16, 8461-8478, doi:10.5194/acp-16-8461-2016, 2016.

Yuan, B., Kaser, L., Karl, T., Graus, M., Peischl, J., Campos, T. L., Shertz, S., Apel, E. C., Hornbrook, R. S., Hills, A., Gilman, J. B., Lerner, B. M., Warneke, C., Flocke, F. M., Ryerson, T. B., Guenther, A. B., and de Gouw, J. A.: Airborne flux measurements of methane and volatile organic compounds over the Haynesville and Marcellus shale gas production regions, *J Geophys Res Atmos*, 120, 6271-6289, doi:10.1002/2015jd023242, 2015.

Zepp, R. G., Faust, B. C., and Hoigne, J.: Hydroxyl radical formation in aqueous reactions (pH 3-8) of iron(II) with hydrogen peroxide: the photo-Fenton reaction, *Environ Sci Technol*, 26, 313-319, doi:10.1021/es00026a011, 1992.

Zhang, H., and Lindberg, S. E.: Sunlight and Iron(III)-induced photochemical production of dissolved gaseous mercury in freshwater, *Environ Sci Technol*, 35, 928-935, doi:10.1021/es001521p, 2001.

Zhang, H., Fu, X. W., Lin, C. J., Wang, X., and Feng, X. B.: Observation and analysis of speciated atmospheric mercury in Shangri-La, Tibetan Plateau, China, *Atmos Chem Phys*, 15, 653-665, doi:10.5194/acp-15-653-2015, 2015.

Zhang, L., Blanchard, P., Gay, D. A., Prestbo, E. M., Risch, M. R., Johnson, D., Narayan, J., Zsolway, R., Holsen, T. M., Miller, E. K., Castro, M. S., Graydon, J. A., Louis, V. L. S., and Dalziel, J.: Estimation of speciated and total mercury dry deposition at monitoring locations in eastern and central North America, *Atmos Chem Phys*, 12, 4327-4340, doi:10.5194/acp-12-4327-2012, 2012a.

Zhang, Y., Jaeglé, L., van Donkelaar, A., Martin, R. V., Holmes, C. D., Amos, H. M., Wang, Q., Talbot, R., Artz, R., Brooks, S., Luke, W., Holsen, T. M., Felton, D., Miller, E. K., Perry, K. D., Schmeltz, D., Steffen, A., Tordon, R., Weiss-Penzias, P., and Zsolway, R.: Nested-grid simulation of mercury over North America, *Atmos Chem Phys*, 12, 6095-6111, doi:10.5194/acp-12-6095-2012, 2012b.

Zhang, Y., Jaeglé, L., Thompson, L., and Streets, D. G.: Six centuries of changing oceanic mercury, *Global Biogeochem Cy*, 28, 1251-1261, doi:10.1002/2014gb004939, 2014.

Zhu, J., Wang, D., Liu, X., and Zhang, Y.: Mercury fluxes from air/surface interfaces in paddy field and dry land, *Appl Geochem*, 26, 249-255, doi:10.1016/j.apgeochem.2010.11.025, 2011.

Zhu, W., Lin, C. J., Wang, X., Sommar, J., Fu, X., and Feng, X.: Global observations and modeling of atmosphere–surface exchange of elemental mercury: a critical review, *Atmos Chem Phys*, 16, 4451-4480, doi:10.5194/acp-16-4451-2016, 2016.